Nano-Hexapod - Test Bench

Dehaeze Thomas

March 25, 2024

Contents

This document is dedicated to the experimental study of the nano-hexapod shown in Figure 1.

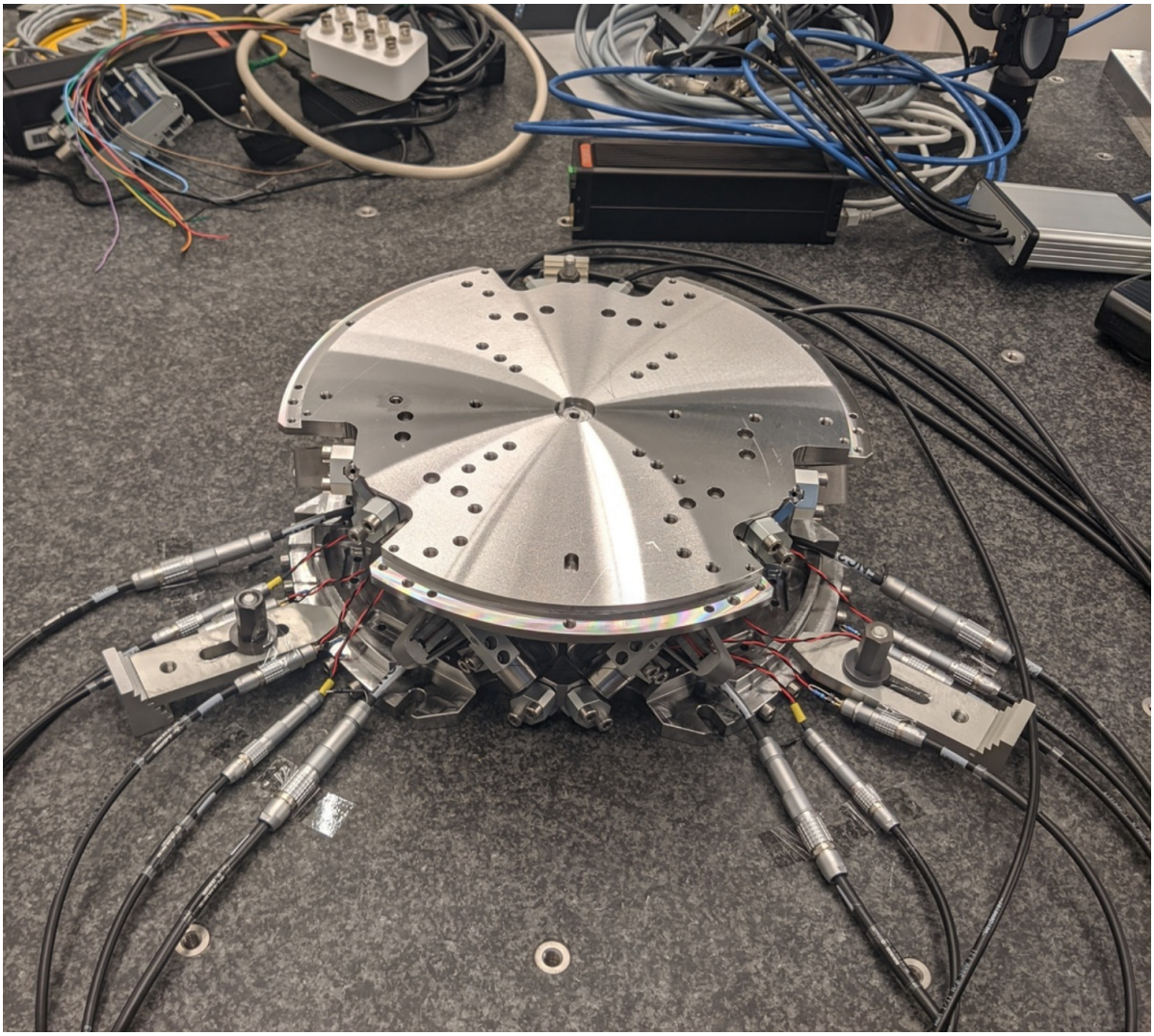

Figure 1: Nano-Hexapod

In Figure 3 is shown a block diagram of the experimental setup. When possible, the notations are consistent with this diagram and summarized in Table 1.

This document is divided in the following sections:

- Section 1: mounting of the nano-hexapod
- Section 2: the dynamics of the nano-hexapod when the encoders are fixed to the struts is studied.
- Section 3: the same is done when the encoders are fixed to the plates.
- Section 4: a decentralized HAC-LAC strategy is studied and implemented.

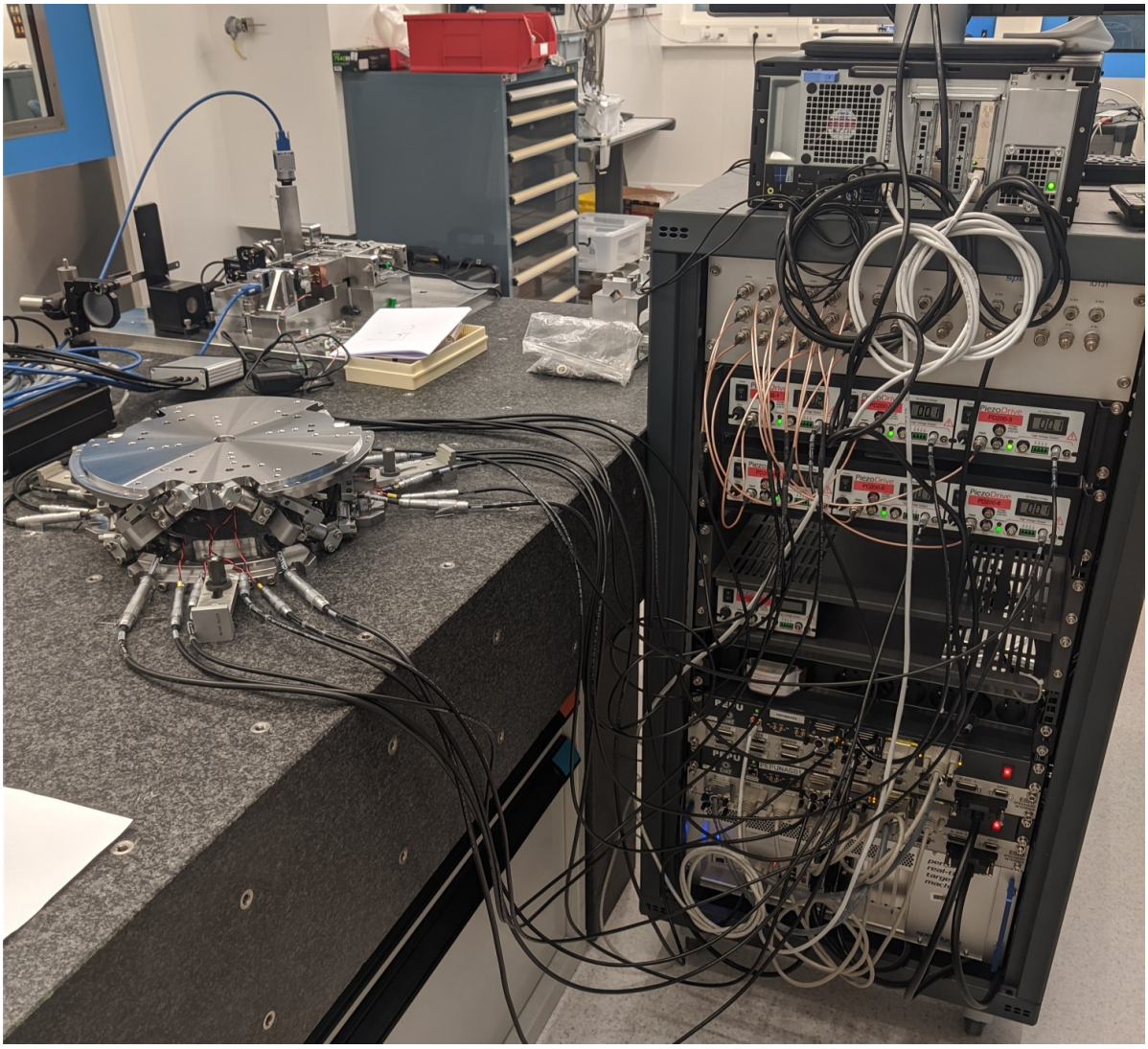

Figure 2: Nano-Hexapod and the control electronics

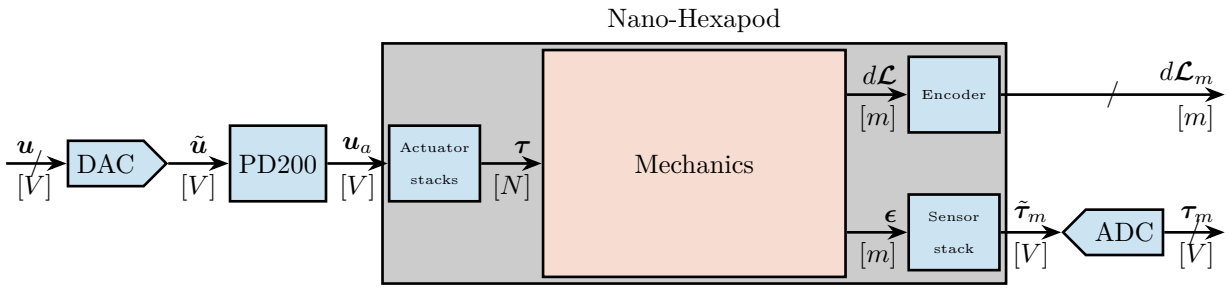

Figure 3: Block diagram of the system with named signals

Table 1: List of signals

	Unit	**Matlab**	**Vector**	**Elements**
Control Input (wanted DAC voltage)	`[V]`	`u`	$\boldsymbol{u}$	u_i
DAC Output Voltage	`[V]`	`u`	$\tilde{\boldsymbol{u}}$	$\tilde{u}_i$
PD200 Output Voltage	`[V]`	`ua`	$\boldsymbol{u}_a$	$u_{a,i}$
Actuator applied force	`[N]`	`tau`	$\boldsymbol{\tau}$	τ_i
Strut motion	`[m]`	`dL`	$d\boldsymbol{\mathcal{L}}$	$d\mathcal{L}_i$
Encoder measured displacement	`[m]`	`dLm`	$d\boldsymbol{\mathcal{L}}_m$	$d\mathcal{L}_{m,i}$
Force Sensor strain	`[m]`	`epsilon`	$\boldsymbol{\epsilon}$	ϵ_i
Force Sensor Generated Voltage	`[V]`	`taum`	$\tilde{\boldsymbol{\tau}}_m$	$\tilde{\tau}_{m,i}$
Measured Generated Voltage	`[V]`	`taum`	$\boldsymbol{\tau}_m$	$\tau_{m,i}$
Motion of the top platform	`[m,rad]`	`dX`	$d\boldsymbol{\mathcal{X}}$	$d\mathcal{X}_i$
Metrology measured displacement	`[m,rad]`	`dXm`	$d\boldsymbol{\mathcal{X}}_m$	$d\mathcal{X}_{m,i}$

1 Mounting Procedure

1.1 Mounting Goals

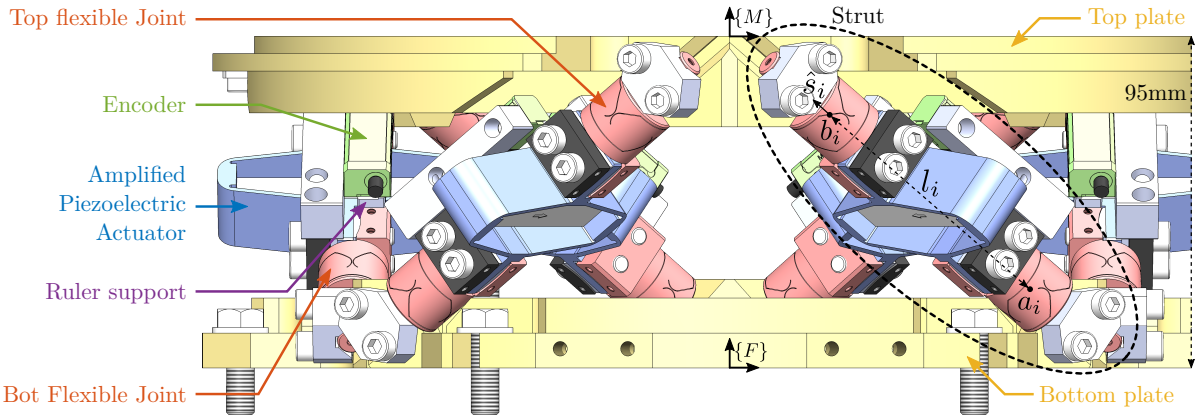

Figure 1.1: Received top and bottom nano-hexapod's plates

1.2 Mounting Bench

1.3 Mounting Procedure

1. Fix the bottom plate with the cylindrical tool

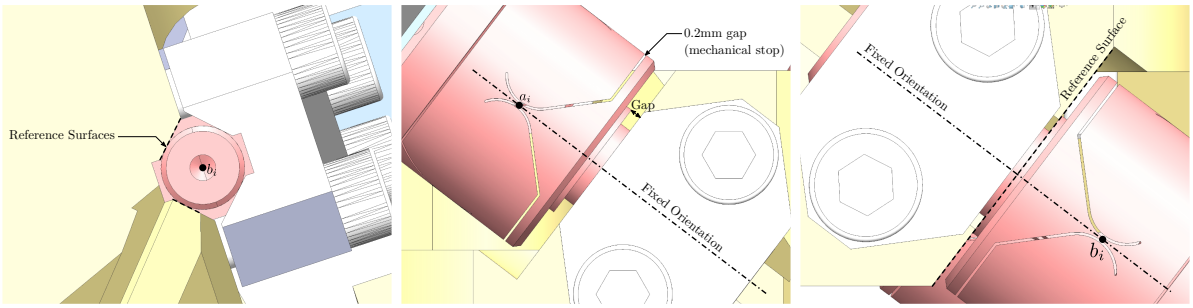

(a) Flexible Joint Clamping **(b)** Bottom Positioning **(c)** Top positioning

Figure 1.2: Fixation of the flexible points to the nano-hexapod plates

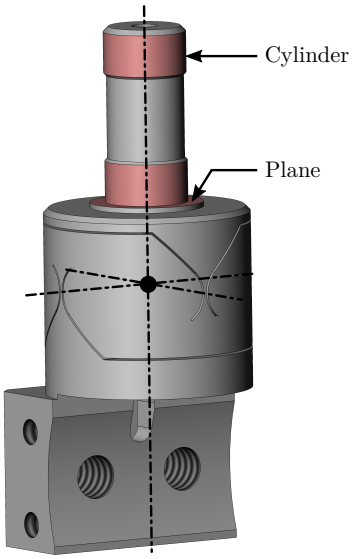

Figure 1.3: Reference surfaces of the flexible joint interface with the plates

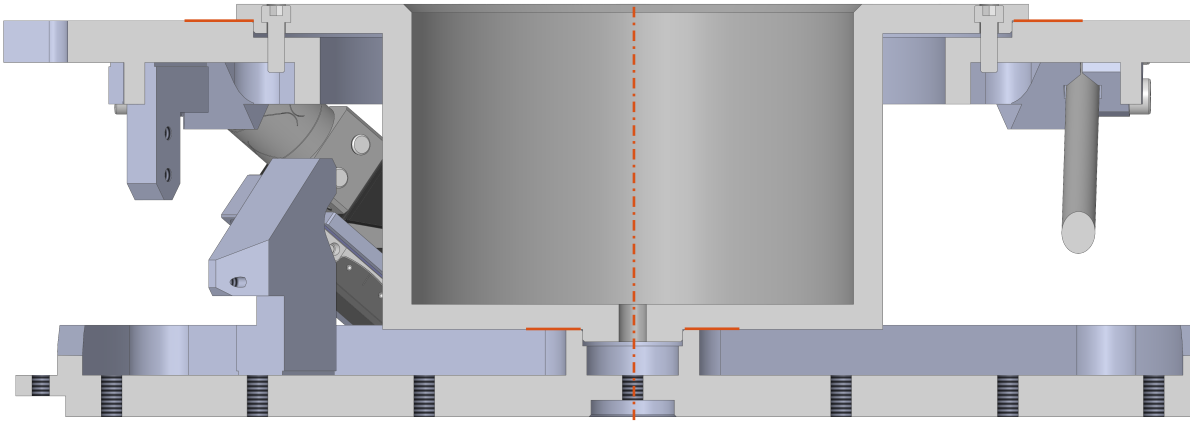

Figure 1.4: Received top and bottom nano-hexapod's plates

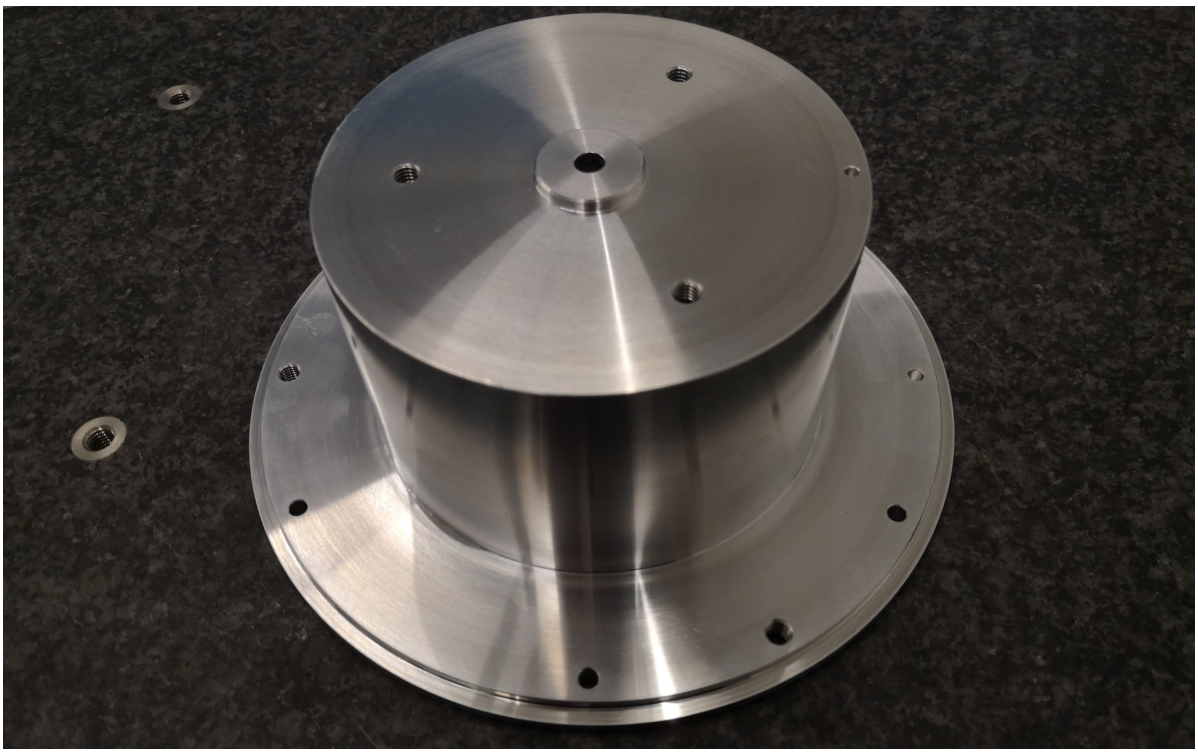

Figure 1.5: Received top and bottom nano-hexapod's plates

2. Put the top plate on the granite
3. Put the cylindrical tool and bottom plate on top of the top plate (Figure 1.8). This position the bottom plate with respect to the top plate in X, Y, Z, Rx, Ry
4. Put the pin to position/fix the Rz. Now the two plates should be position and clamped together
5. Fix the 6 struts
6. Remove the pin and the tool
7. Put the nano-hexapod in place

1.4 Nano-Hexapod Mounting

1.4.1 Plates

1.4.2 Mounting Tool

A mounting tool is used to position the top and bottom platforms. Then the struts can be mounted one by one. When all the struts are mounted, the "mounting tool" is disassembled and the nano-hexapod is considered to be mounted.

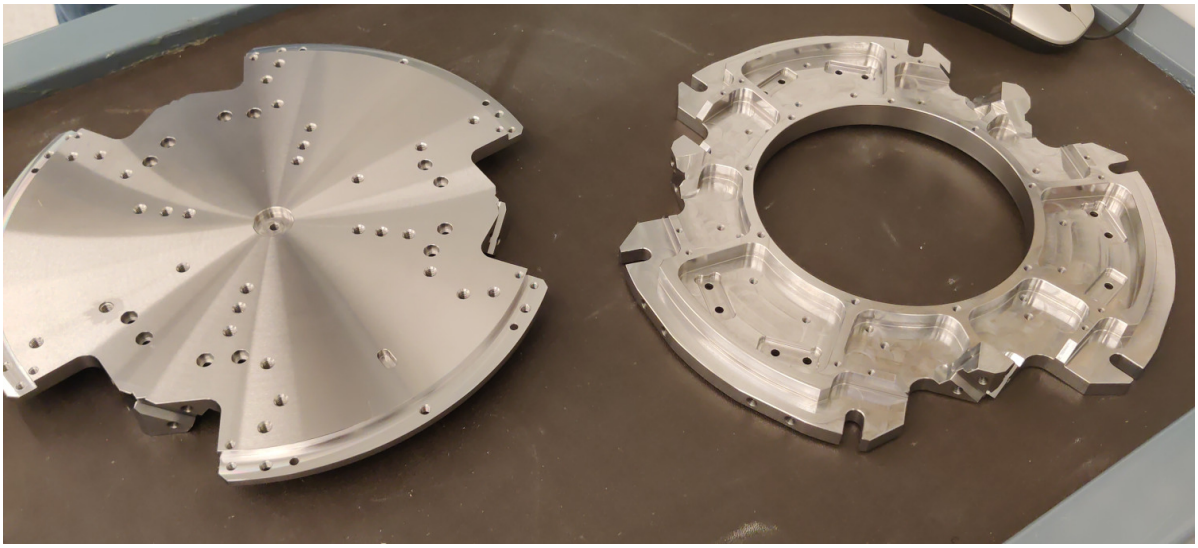

Figure 1.6: Received top and bottom nano-hexapod's plates

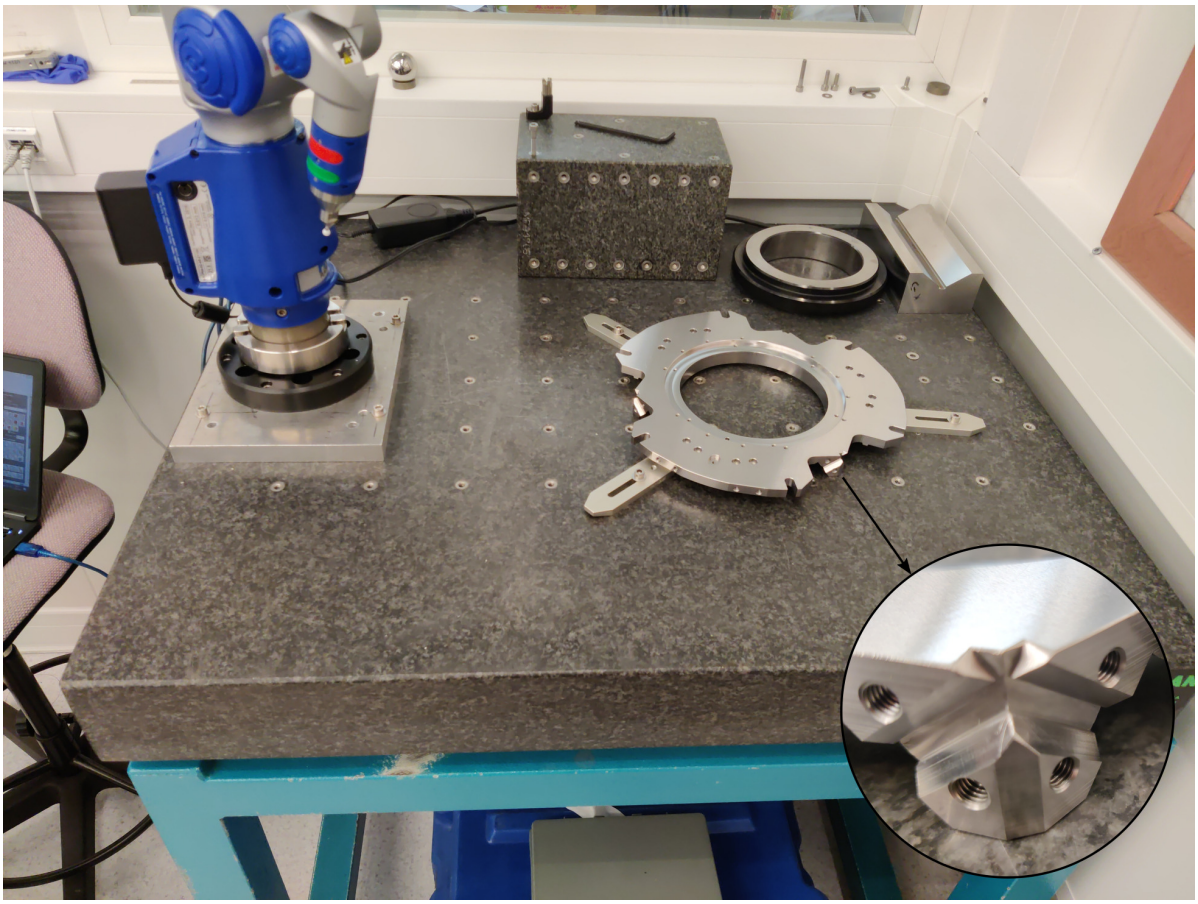

Figure 1.7: Bottom plate on the measurement granite (FARO arm). Zoom on the main feature of the plate

The main goal of this "mounting tool" is to position the "V" shapes of both plates such that they are coaxial.

The straightness is the diameter of the smallest cylinder containing all points of the axis.

Table 1.1: Measured straightness between the two "V" for the six struts. These measurements are performed two times for each strut.

Strut nb	**Meas 1**	**Meas 2**
1	7um	3um
2	11um	11um
3	15um	14um
4	6um	6um
5	7um	5um
6	6um	7um

Using the FARO arm, the coaxiality of the "V" shapes have been measured to better than 15 μm! This means that the two cylinders corresponding to the flexible joints are both within a perfect cylinder with a diameter of 15 μm. This is probably better than that, but we reached the limit of the FARO arm's precision.

1.4.3 Mounted Hexapod

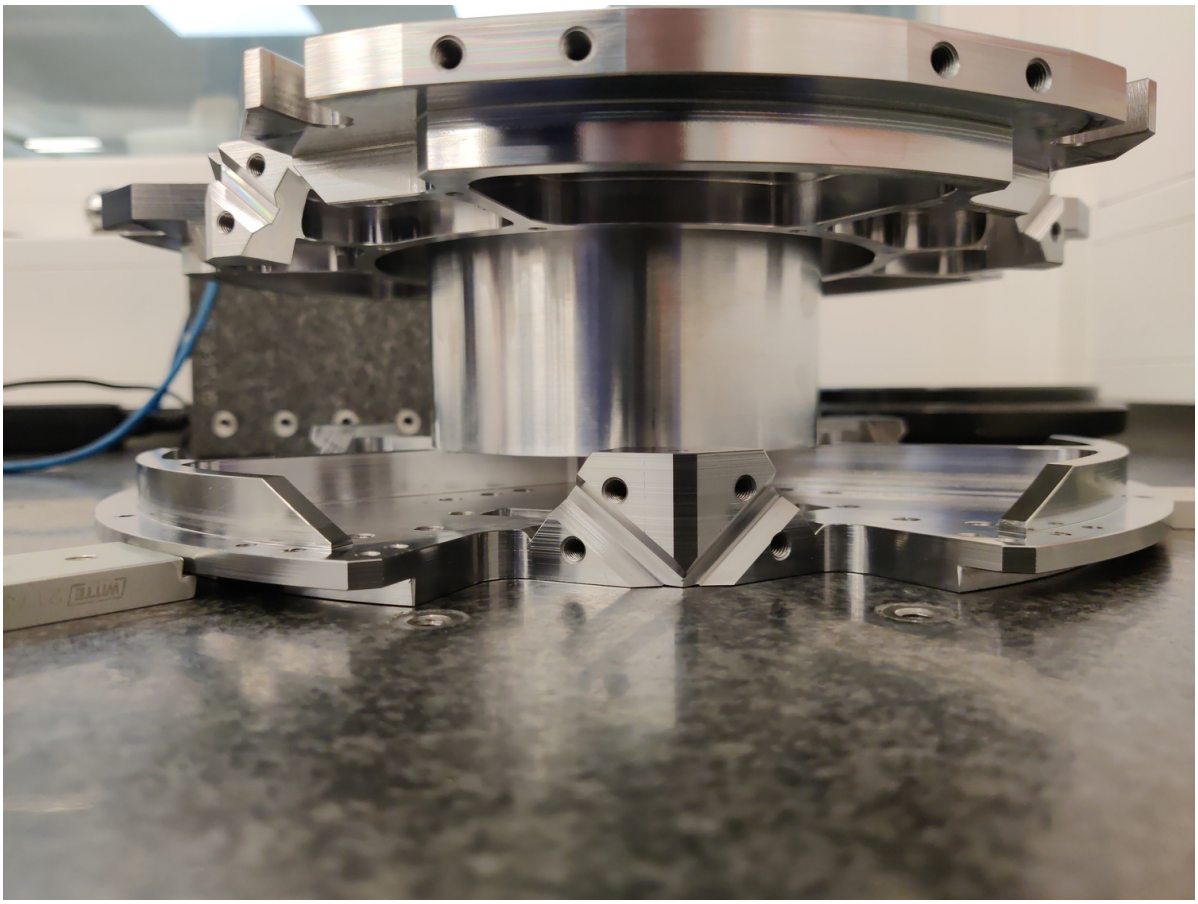

Figure 1.8: Bottom and top plates mounted together with the special tool

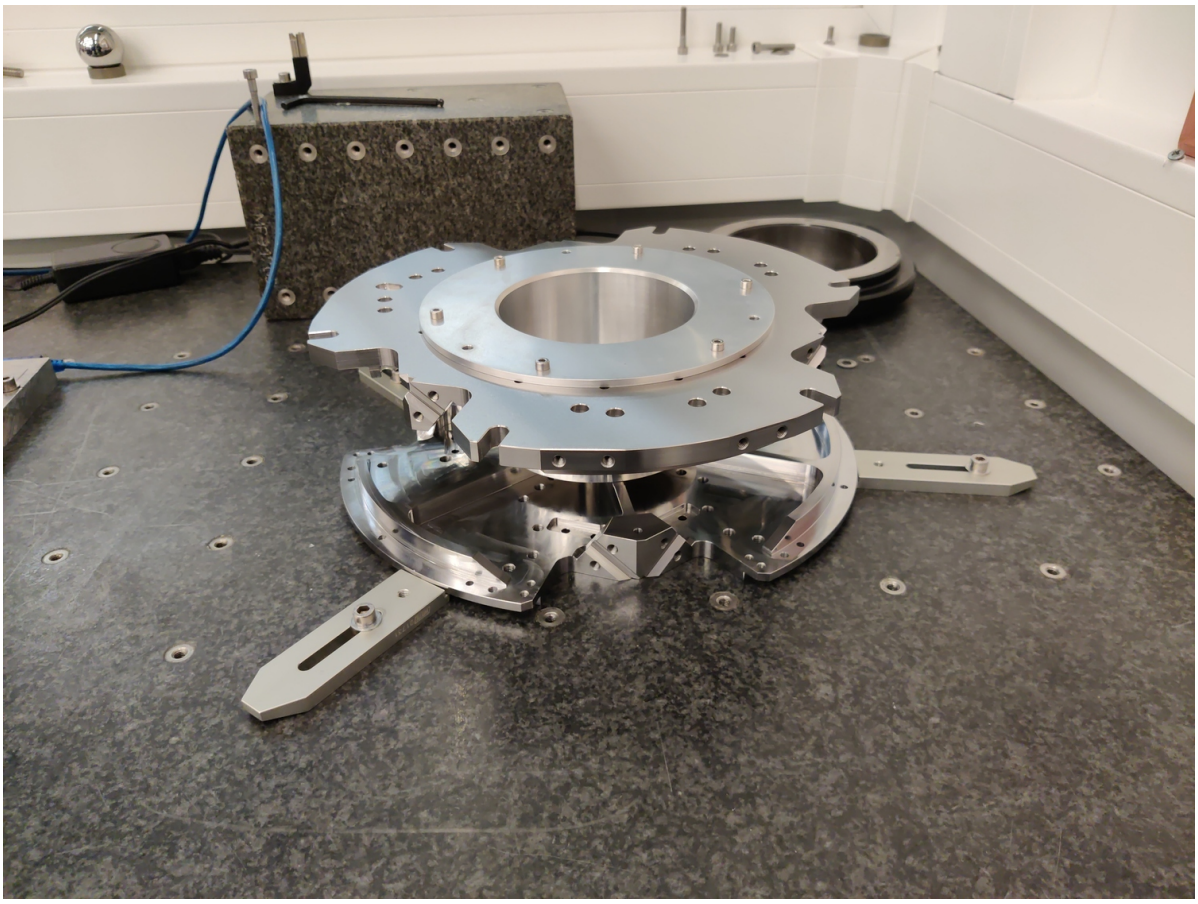

Figure 1.9: Bottom and top plates mounted together with the special tool (top view)

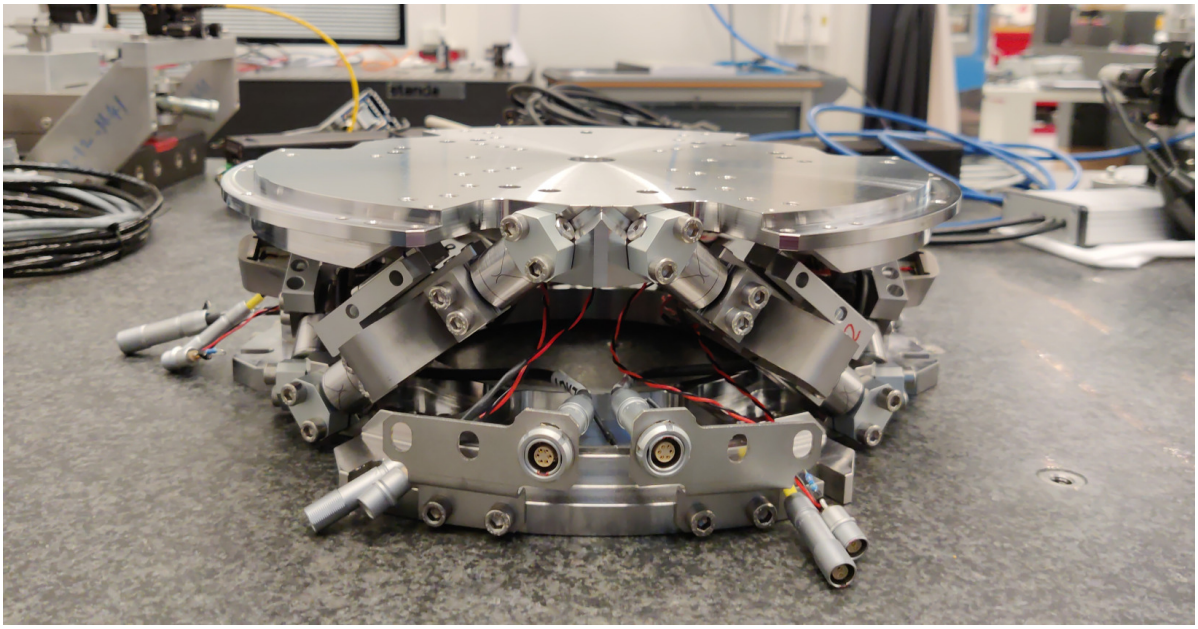

Figure 1.10: Mounted Nano-Hexapod

2 Encoders fixed to the struts

In this section, the encoders are fixed to the struts.

It is divided in the following sections:

- Section 2.1: the transfer function matrix from the actuators to the force sensors and to the encoders is experimentally identified.
- Section 2.3: the obtained FRF matrix is compared with the dynamics of the simscape model
- Section 2.4: decentralized Integral Force Feedback (IFF) is applied and its performances are evaluated.
- Section 2.5: a modal analysis of the nano-hexapod is performed

2.1 Identification of the dynamics

2.1.1 Load Measurement Data

Two identifications are performed, one for low frequencies and one for higher frequencies.

2.1.2 Spectral Analysis - Setup

The window used for the spectral analysis is defined as well as the frequency vector `f`.

2.1.3 Transfer function from Actuator to Encoder

The 6x6 transfer function matrix from $\boldsymbol{u}$ to $d\boldsymbol{\mathcal{L}}_m$ is estimated and shown in Figure 2.1.

Important

The low frequency gain of the transfer function from $\boldsymbol{u}$ to $d\boldsymbol{\mathcal{L}}_m$ is close to diagonal. Then the coupling is quite large starting from the frequency of the first suspension mode (110Hz to 180Hz). Additional modes at 220Hz, 300Hz and 380Hz which are the modes of the struts are adding a lot of complexity in the plant and phase drops. Then there is a mode at 700Hz which correspond to a flexible mode of the top plate.

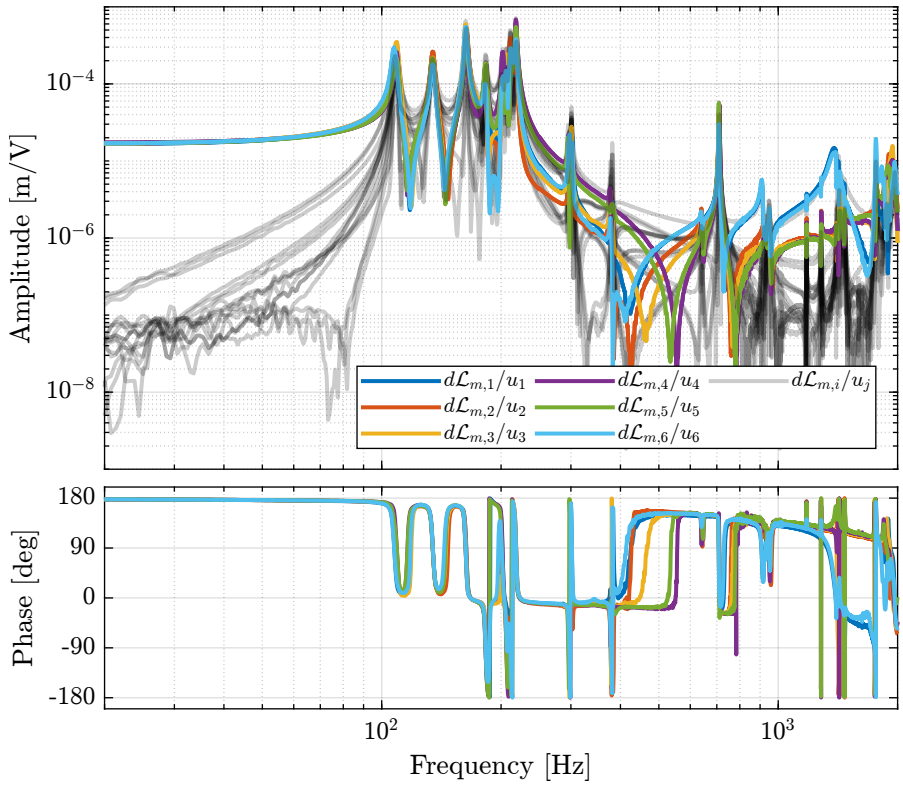

Figure 2.1: Measured FRF for the transfer function from $\boldsymbol{u}$ to $d\boldsymbol{\mathcal{L}_m}$

2.1.4 Transfer function from Actuator to Force Sensor

The 6x6 transfer function matrix from $\boldsymbol{u}$ to $\boldsymbol{\tau}_m$ is estimated and shown in Figure 2.2.

Important

The transfer function matrix from $\boldsymbol{u}$ to $\boldsymbol{\tau}_m$ in Figure 2.2 has alternating poles and zeros as expected. The 4 suspensions modes have quite separated poles and zeros which indicates that is should be possible to add a good amount of damping to these modes using Integral Force Feedback.

2.1.5 Save Identified Plants

The identified plants are now saved for further analysis.

2.2 Jacobian matrices and centralized plants

The Jacobian is used to transform the excitation force in the cartesian frame as well as the displacements.

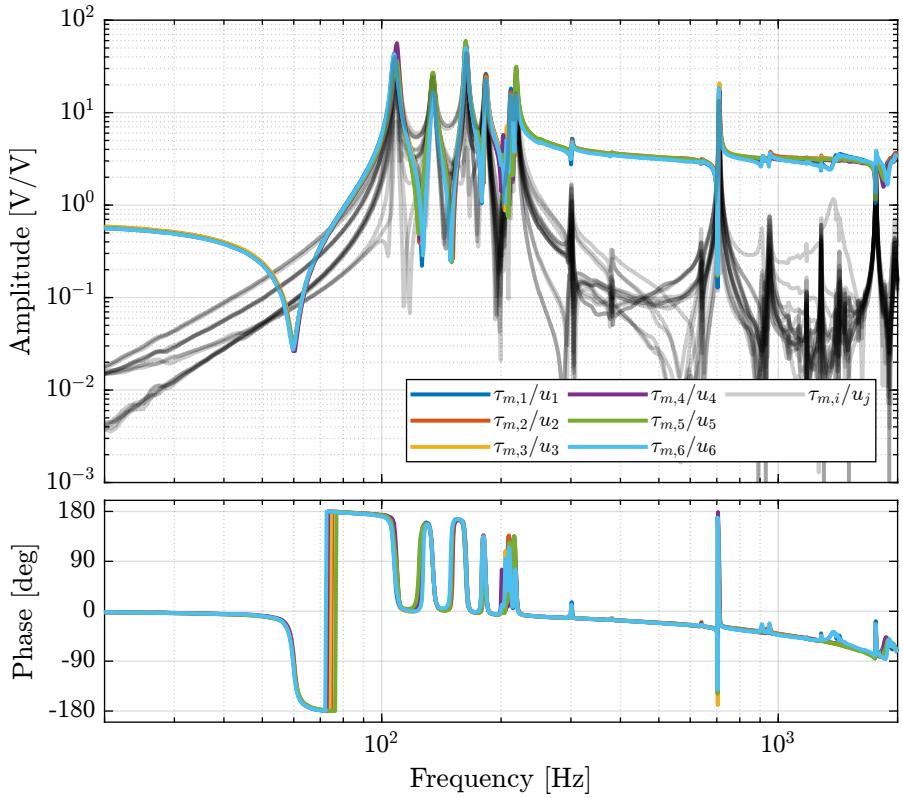

Figure 2.2: Measured FRF for the transfer function from $\boldsymbol{u}$ to $\boldsymbol{\tau}_m$

Consider the plant shown in Figure 2.3 with:

- $\boldsymbol{u}$ the 6 input voltages (going to the PD200 amplifier and then to the APA)
- $d\boldsymbol{\mathcal{L}}$ the relative motion sensor outputs (encoders)
- $\boldsymbol{\tau}_m$ the generated voltage of the force sensor stacks
- J_a and J_s the Jacobians for the actuators and sensors

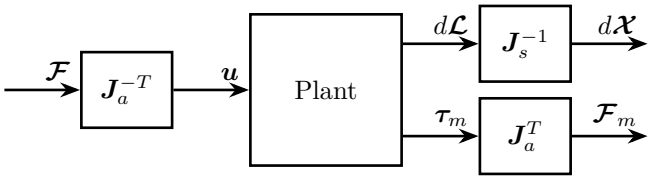

Figure 2.3: Plant in the cartesian Frame

2.2.1 Jacobian Matrices

The Jacobian matrices (for the sensors and for the actuators) are estimated in two cases:

- when the point of interest is at 150mm above the top platform
- when the point of interest is at the "center of stiffness" (42mm below the top platform)

2.2.2 Obtained Centralized plants

The transfer function matrices from $\boldsymbol{\mathcal{F}}$ to $d\boldsymbol{\mathcal{X}}$ are computed for both Jacobians and shown in Figures 2.4 (Center of Stiffness) and 2.5 (Point of Interest).

Important

The centralized plant evaluated at the Center of Stiffness (Figure 2.4) is presenting a good decoupling at low frequency which is not the case for the Centralized plant at the point of interest in Figure 2.5.

2.2.3 Centralized plant using the Force sensors

The transfer function from $\boldsymbol{\mathcal{F}}$ to $\boldsymbol{\mathcal{F}}_m$ is computed using the Jacobian evaluated at the Center of Stiffness and shown in Figure 2.6.

From Figure 2.6, we can well estimate the directions of the suspension modes:

- modes at 110Hz and 160Hz are horizontal translation/rotation modes
- mode at 135Hz is a pure vertical mode

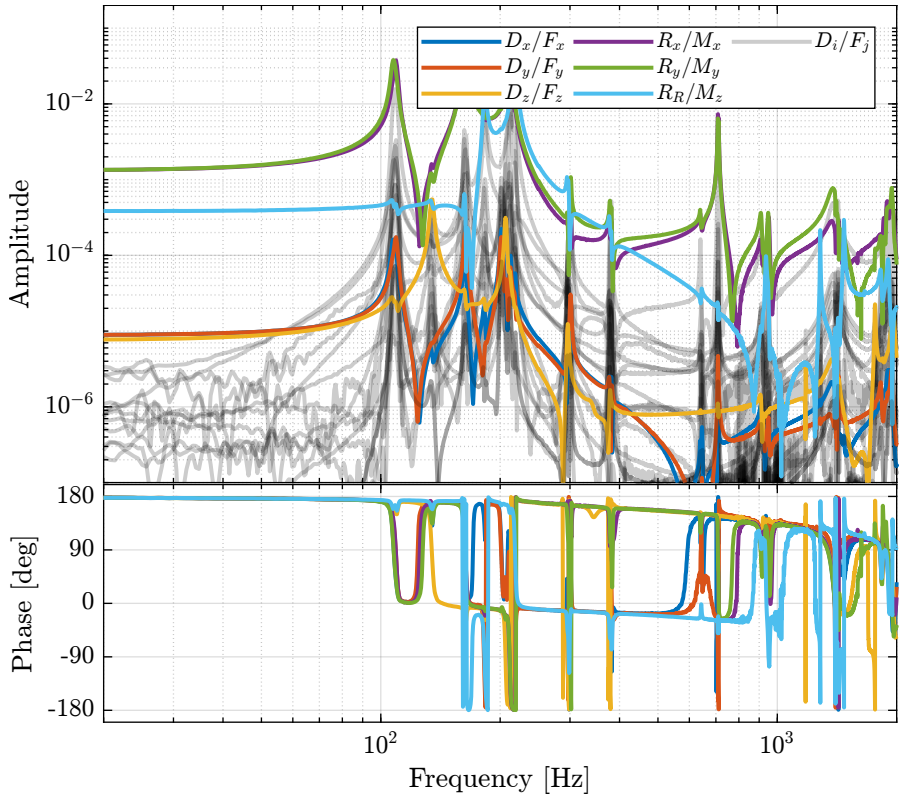

Figure 2.4: Bode plot of the transfer function from $\boldsymbol{\mathcal{F}}$ to $d\boldsymbol{\mathcal{X}}$ which is computed using the Jacobian matrices evaluted at the Center of Stiffness

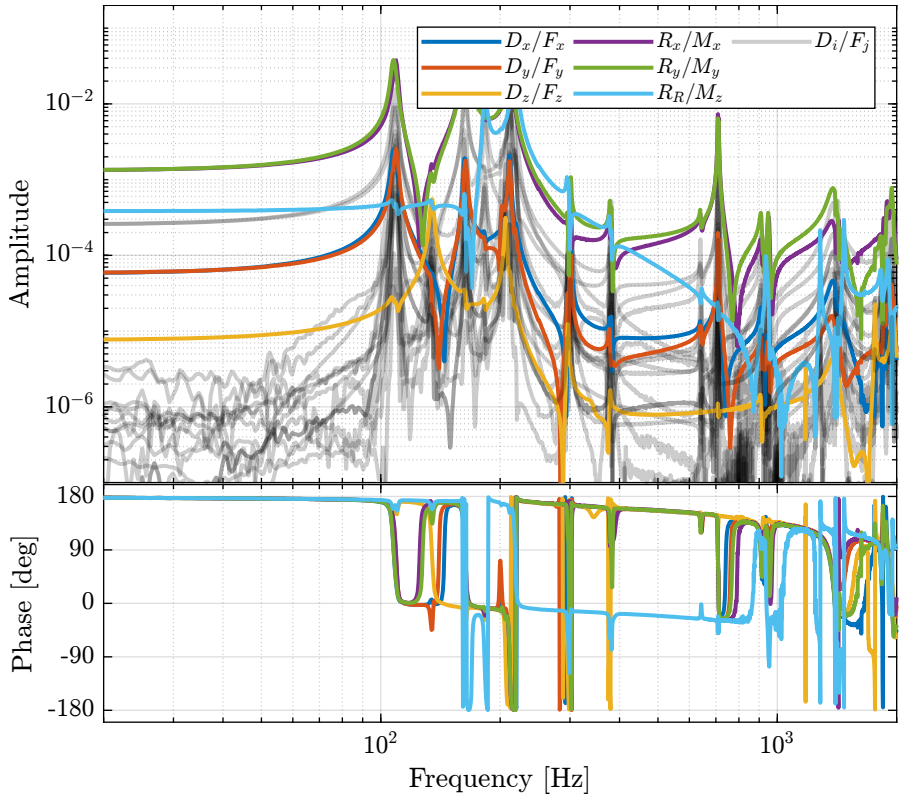

Figure 2.5: Bode plot of the transfer function from $\boldsymbol{\mathcal{F}}$ to $d\boldsymbol{\mathcal{X}}$ which is computed using the Jacobian matrices evaluated at the Point of Interest

- mode at 185Hz is a pure rotation mode around the vertical axis

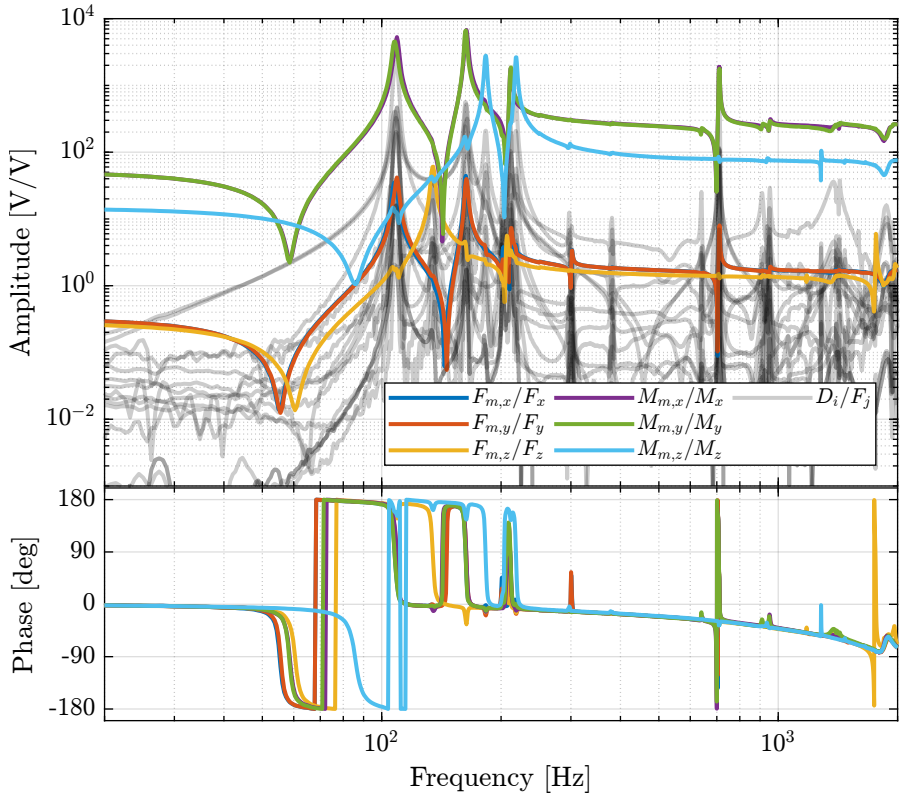

Figure 2.6: Measured FRF for the IFF plant in the cartesian frame

2.3 Comparison with the Simscape Model

In this section, the measured dynamics is compared with the dynamics estimated from the Simscape model.

2.3.1 Simscape Model - Identification

Let's initialize the nano-hexapod using 2 DoF models for the APA.

The Nano-hexapod is fixed on a rigid granite and no payload is fixed on top of the hexapod. The transfer function matrix from $\boldsymbol{u}$ to $\boldsymbol{\tau}_m$ using the Simscape model is now extracted.

And the plant from $\boldsymbol{u}$ to $d\boldsymbol{\mathcal{L}}_m$.

Both transfer functions are saved for further use.

2.3.2 Dynamics from Actuator to Force Sensors

The comparison between the extracted model and the measurement is done in Figures 2.7 (diagonal elements) and 2.8 (off-diagonal elements).

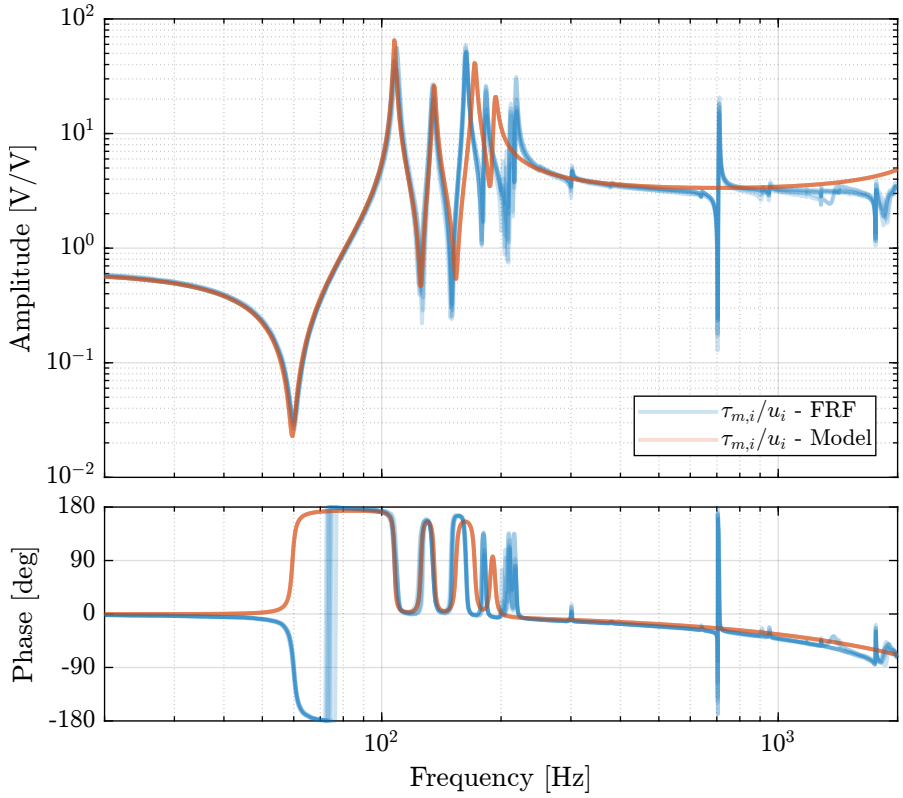

Figure 2.7: Comparison of the diagonal elements of the transfer function matrix from $\boldsymbol{u}$ to $\boldsymbol{\tau}_m$ - Simscape Model and measured FRF

2.3.3 Dynamics from Actuator to Encoder

The comparison between the model is done in Figures 2.9 and 2.10.

Important

The Simscape model is quite accurately representing the system dynamics. Using 2dof models for the APA, we don't model the flexible modes of the APA. Similarly, the flexible modes of the top plate are not modelled. But up to 200Hz, the model is accurate.

2.3.4 Using Flexible model

In order to model flexible modes of the APA, flexible elements are used and some misalignment between the APA and the flexible joints is introduced.

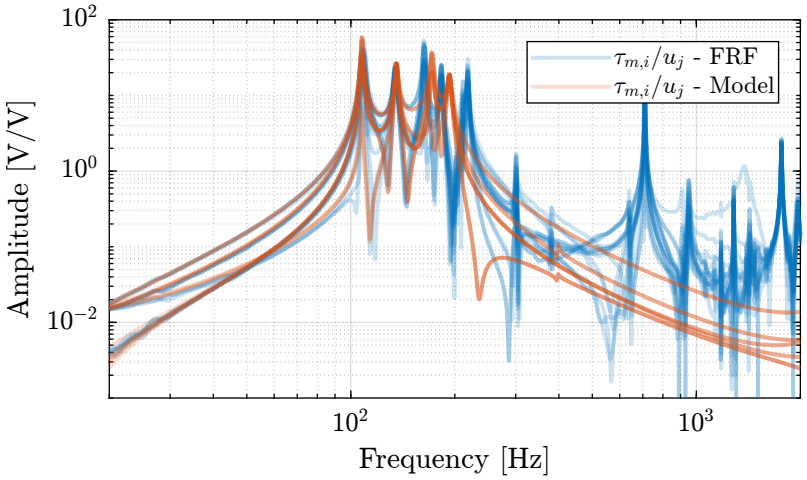

Figure 2.8: Comparison of the off-diagonal elements of the transfer function matrix from $\boldsymbol{u}$ to $\boldsymbol{\tau}_m$ - Simscape Model and measured FRF

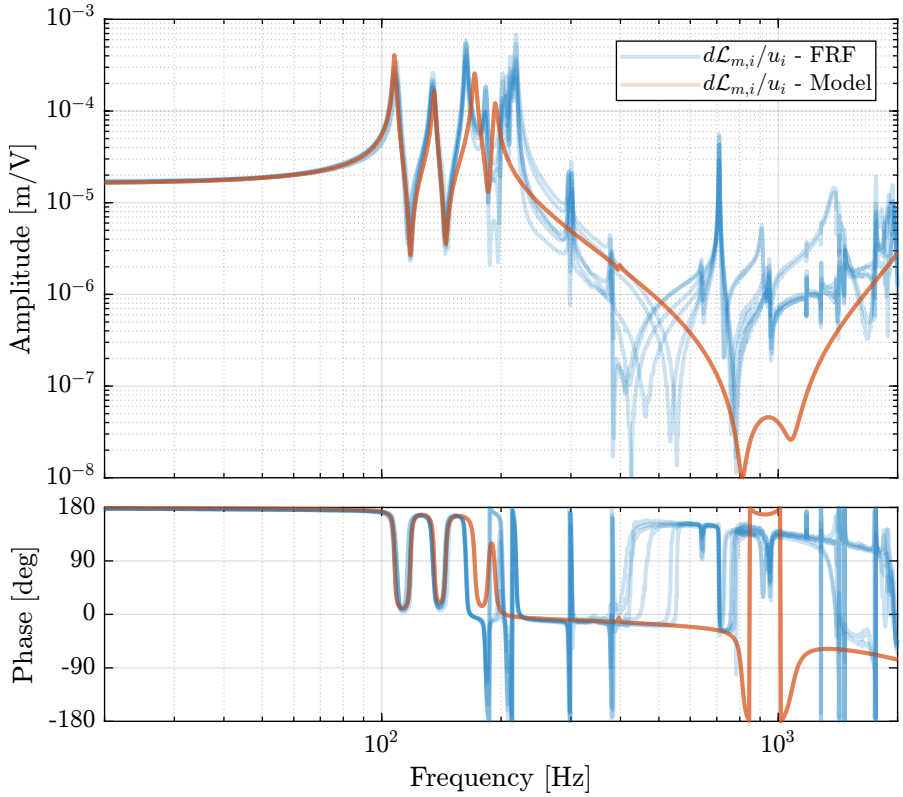

Figure 2.9: Diagonal elements of the DVF Plant

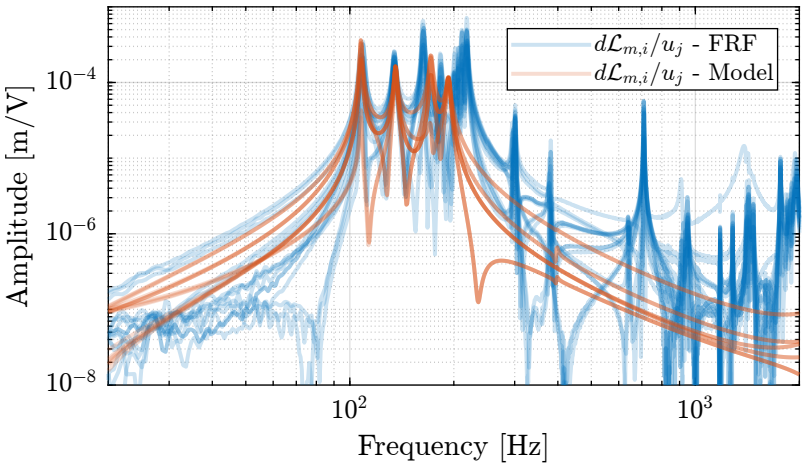

Figure 2.10: Off diagonal elements of the DVF Plant

These misalignments are estimated from measurements performed on each of the struts. The dynamics from $\boldsymbol{u}$ to $d\boldsymbol{\mathcal{L}}_m$ is estimated. The obtained diagonal elements are compared with the measurements in Figure 2.11. Modeling the APA as flexible elements can indeed yields to more accurate models. However this also adds a lot of states to the system, and time domain simulations can become realy long to perform.

2.4 Integral Force Feedback

In this section, the Integral Force Feedback (IFF) control strategy is applied to the nano-hexapod. The main goal of this to add damping to the nano-hexapod's modes.

The control architecture is shown in Figure 2.12 where $\boldsymbol{K}_{\text{IFF}}$ is a diagonal 6×6 controller.

The system as then a new input $\boldsymbol{u}'$, and the transfer function from $\boldsymbol{u}'$ to $d\boldsymbol{\mathcal{L}}_m$ should be easier to control than the initial transfer function from $\boldsymbol{u}$ to $d\boldsymbol{\mathcal{L}}_m$.

This section is structured as follow:

- Section 2.4.1: Using the Simscape model (APA taken as 2DoF model), the transfer function from $\boldsymbol{u}$ to $\boldsymbol{\tau}_m$ is identified. Based on the obtained dynamics, the control law is developed and the optimal gain is estimated using the Root Locus.
- Section 2.4.2: Still using the Simscape model, the effect of the IFF gain on the the transfer function from $\boldsymbol{u}'$ to $d\boldsymbol{\mathcal{L}}_m$ is studied.
- Section 2.4.3: The same is performed experimentally: several IFF gains are used and the damped plant is identified each time.
- Section 2.4.4: The damped model and the identified damped system are compared for the optimal IFF gain. It is found that IFF indeed adds a lot of damping into the system. However it is not efficient in damping the spurious struts modes.

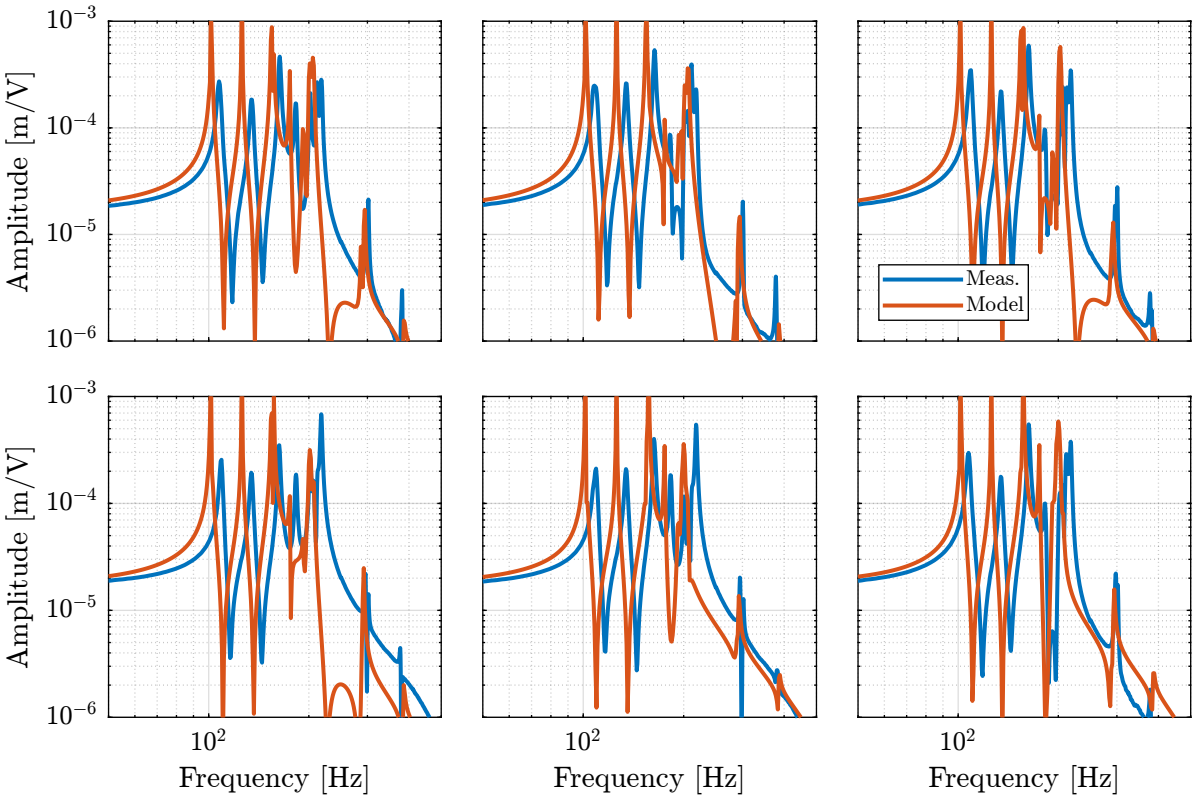

Figure 2.11: Comparison of the measured transfer functions from u_i to $d\mathcal{L}_{m,i}$ - Simscape model and measured FRF

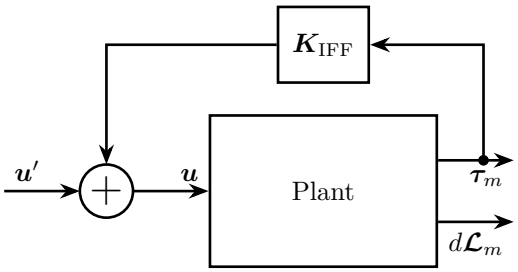

Figure 2.12: Integral Force Feedback Strategy

- Section 2.4.5: Finally, a "flexible" model of the APA is used in the Simscape model and the optimally damped model is compared with the measurements.

2.4.1 IFF Control Law and Optimal Gain

The IFF controller is defined as shown below: Then, the poles of the system are shown in the complex plane as a function of the controller gain (i.e. Root Locus plot) in Figure 2.13. A gain of 400 is chosen as the "optimal" gain as it visually seems to be the gain that adds the maximum damping to all the suspension modes simultaneously.

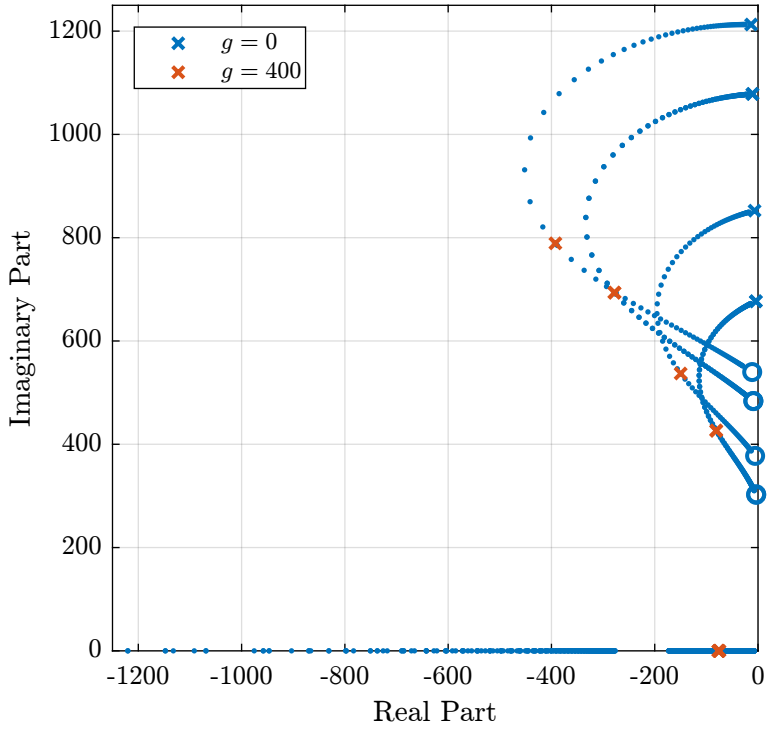

Figure 2.13: Root Locus for the IFF control strategy

Then the "optimal" IFF controller is defined: And it is saved for further use. The bode plots of the "diagonal" elements of the loop gain are shown in Figure 2.14. It is shown that the phase and gain margins are quite high and the loop gain is large around the resonances.

2.4.2 Effect of IFF on the transfer function from actuator to encoder - Simulations

Still using the Simscape model with encoders fixed to the struts and 2DoF APA, the IFF strategy is tested. The Nano-hexapod is fixed on a rigid granite and no payload is fixed on top of the hexapod. The following IFF gains are tested: And the transfer functions from $\boldsymbol{u}'$ to $d\boldsymbol{\mathcal{L}}_m$ are identified for all the IFF gains. The obtained dynamics are shown in Figure 2.15.

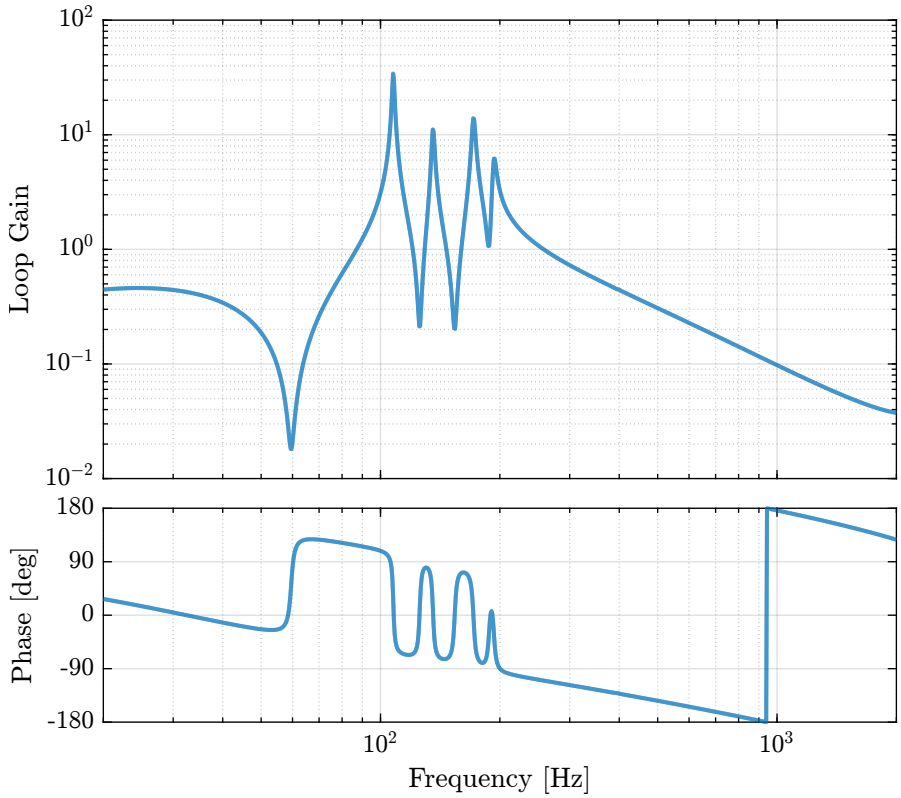

Figure 2.14: Bode plot of the "decentralized loop gain" $G_{\text{iff}}(i,i) \times K_{\text{iff}}(i,i)$

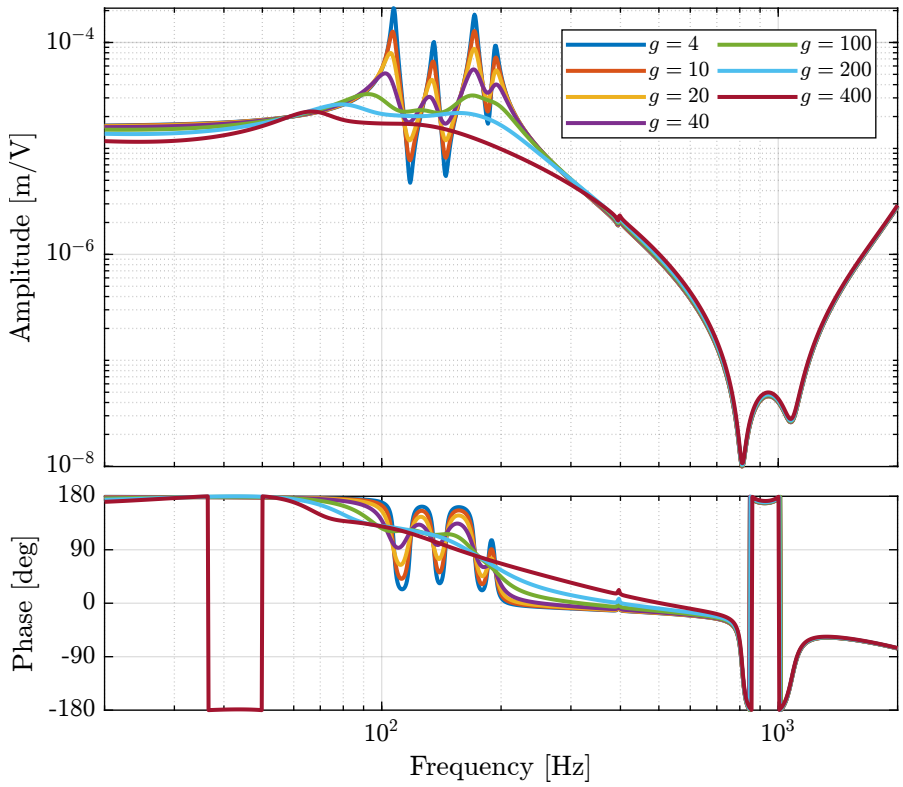

Figure 2.15: Effect of the IFF gain g on the transfer function from $\boldsymbol{\tau}$ to $d\boldsymbol{\mathcal{L}}_m$

2.4.3 Effect of IFF on the plant - Experimental Results

The IFF strategy is applied experimentally and the transfer function from $\boldsymbol{u}'$ to $d\boldsymbol{\mathcal{L}}_m$ is identified for all the defined values of the gain.

Load Data First load the identification data.

Spectral Analysis - Setup And define the useful variables that will be used for the identification using the `tfestimate` function.

DVF Plant The transfer functions are estimated for all the values of the gain. The obtained dynamics as shown in the bode plot in Figure 2.16. The dashed curves are the results obtained using the model, and the solid curves the results from the experimental identification.

The bode plot is then zoomed on the suspension modes of the nano-hexapod in Figure 2.17.

Important

The IFF control strategy is very effective for the damping of the suspension modes. It however does not damp the modes at 200Hz, 300Hz and 400Hz (flexible modes of the APA).

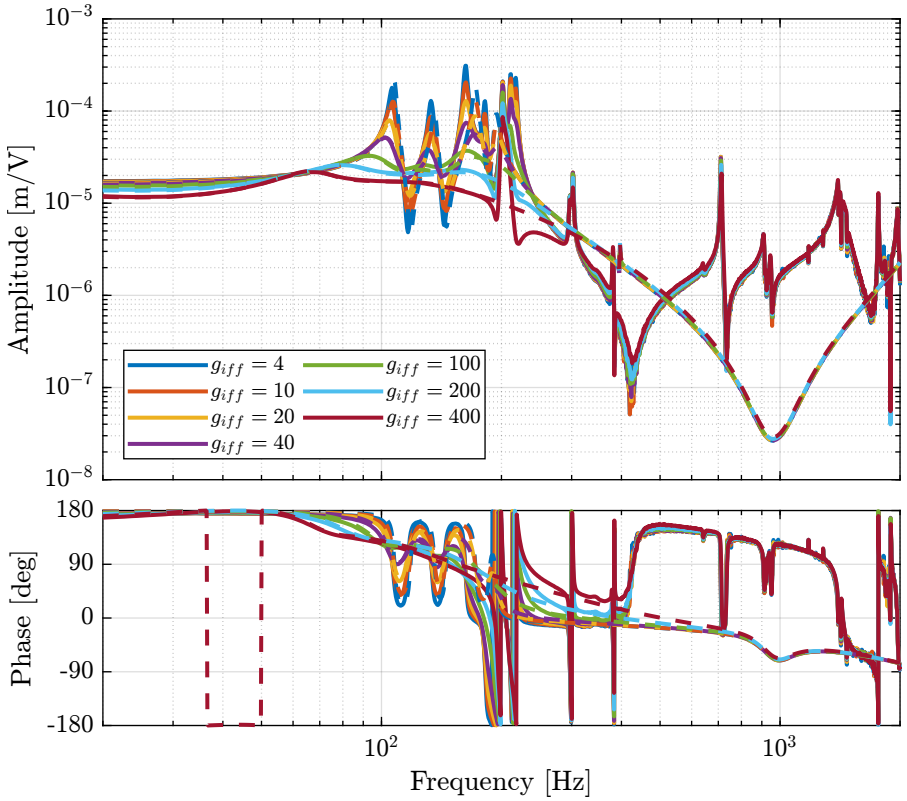

Figure 2.16: Transfer function from u to $d\mathcal{L}_m$ for multiple values of the IFF gain

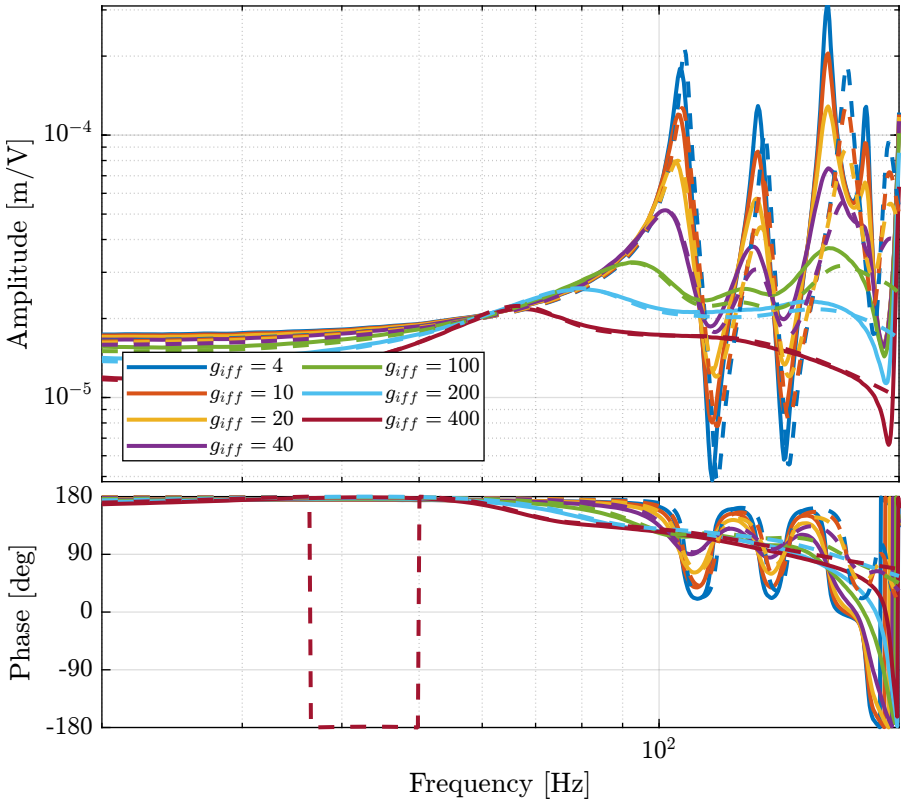

Figure 2.17: Transfer function from u to $d\mathcal{L}_m$ for multiple values of the IFF gain (Zoom)

Also, the experimental results and the models obtained from the Simscape model are in agreement concerning the damped system (up to the flexible modes).

Experimental Results - Comparison of the un-damped and fully damped system The un-damped and damped experimental plants are compared in Figure 2.18 (diagonal terms).

It is very clear that all the suspension modes are very well damped thanks to IFF. However, there is little to no effect on the flexible modes of the struts and of the plate.

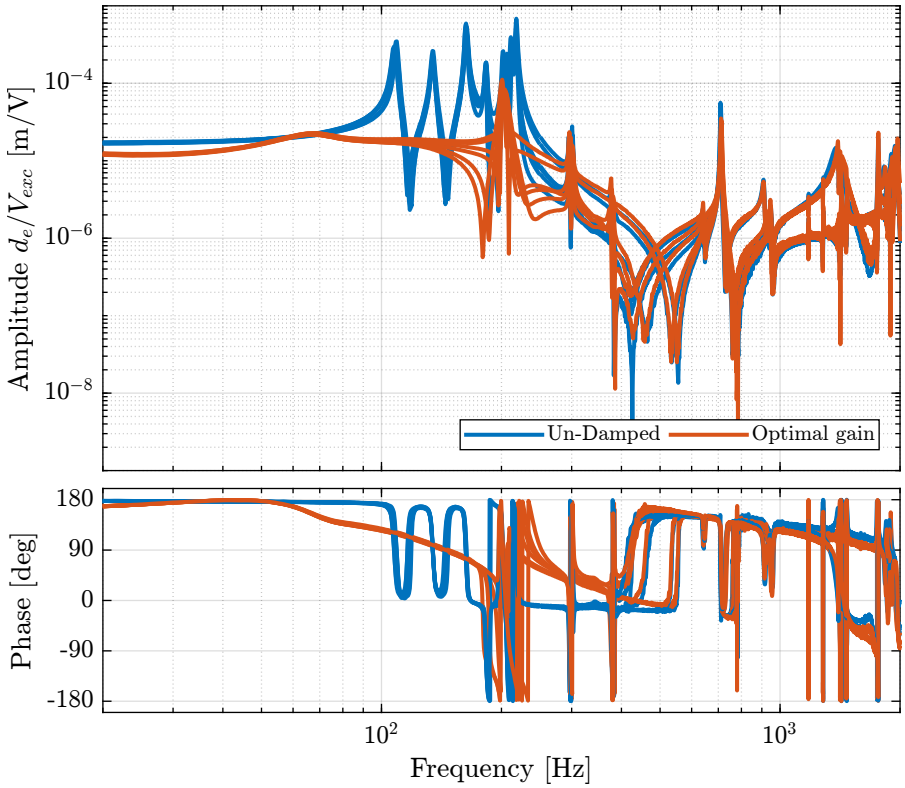

Figure 2.18: Comparison of the diagonal elements of the tranfer function from $\boldsymbol{u}$ to $d\boldsymbol{\mathcal{L}}_m$ without active damping and with optimal IFF gain

2.4.4 Experimental Results - Damped Plant with Optimal gain

Let's now look at the 6×6 damped plant with the optimal gain $g = 400$.

Load Data The experimental data are loaded.

Spectral Analysis - Setup And the parameters useful for the spectral analysis are defined.

DVF Plant Finally, the 6×6 plant is identified using the `tfestimate` function. The obtained diagonal elements are compared with the model in Figure 2.19.

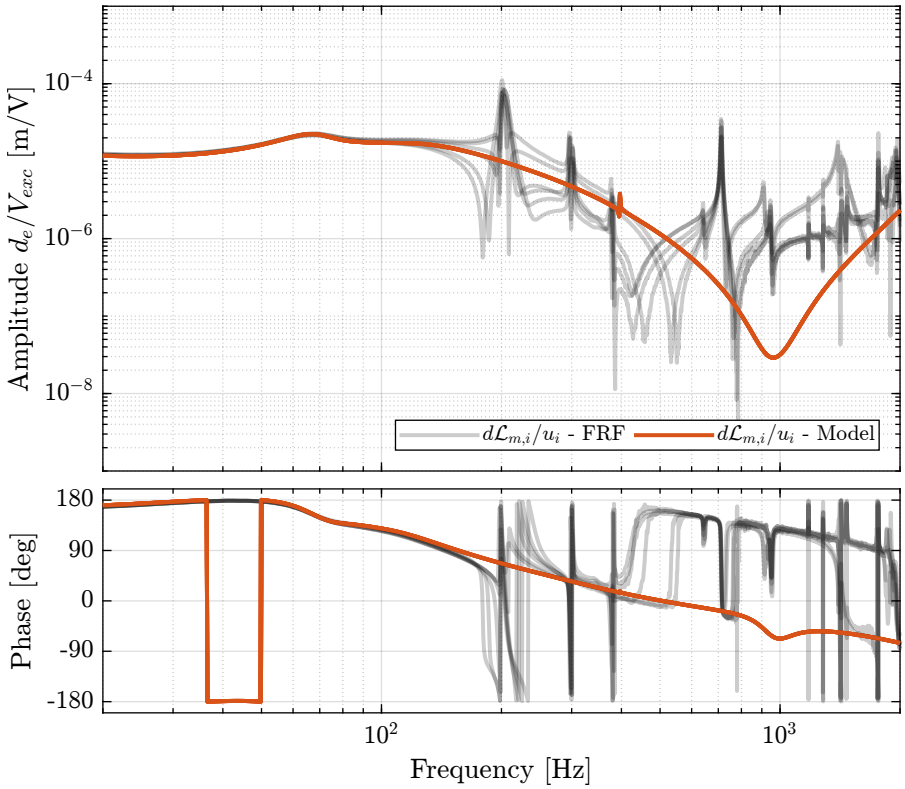

Figure 2.19: Comparison of the diagonal elements of the transfer functions from $\boldsymbol{u}$ to $d\boldsymbol{\mathcal{L}}_m$ with active damping (IFF) applied with an optimal gain $g = 400$

And all the off-diagonal elements are compared with the model in Figure 2.20.

Important

With the IFF control strategy applied and the optimal gain used, the suspension modes are very well damped. Remains the un-damped flexible modes of the APA (200Hz, 300Hz, 400Hz), and the modes of the plates (700Hz).
The Simscape model and the experimental results are in very good agreement.

2.4.5 Comparison with the Flexible model

When using the 2-DoF model for the APA, the flexible modes of the struts were not modelled, and it was the main limitation of the model. Now, let's use a flexible model for the APA, and see if the obtained damped plant using the model is similar to the measured dynamics.

First, the nano-hexapod is initialized. And the "optimal" controller is loaded. The transfer function from $\boldsymbol{u}'$ to $d\boldsymbol{\mathcal{L}}_m$ is identified using the Simscape model. The obtained diagonal elements are shown in Figure 2.21 while the off-diagonal elements are shown in Figure 2.22.

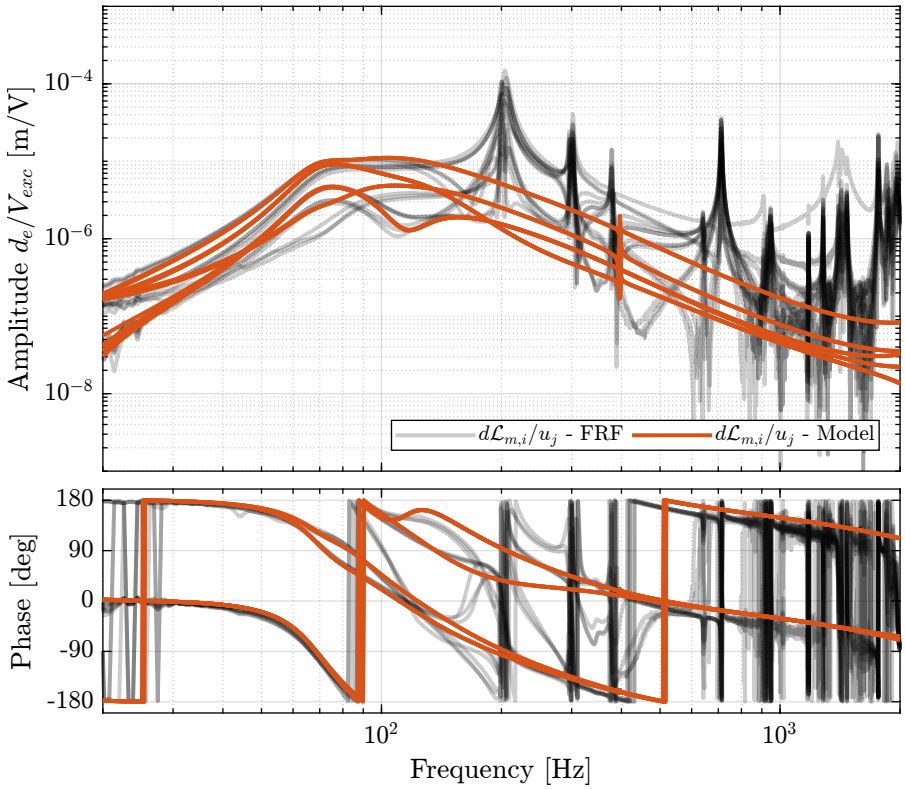

Figure 2.20: Comparison of the off-diagonal elements of the transfer functions from $\boldsymbol{u}$ to $d\boldsymbol{\mathcal{L}}_m$ with active damping (IFF) applied with an optimal gain $g = 400$

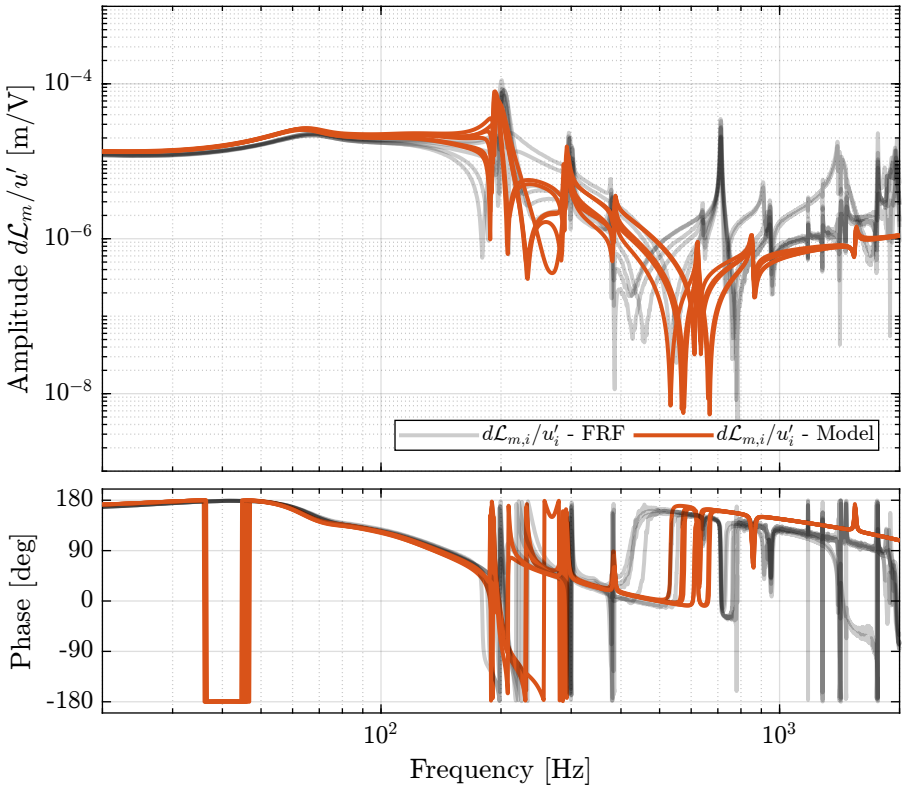

Figure 2.21: Diagonal elements of the transfer function from $\boldsymbol{u}'$ to $d\boldsymbol{\mathcal{L}}_m$ - comparison of the measured FRF and the identified dynamics using the flexible model

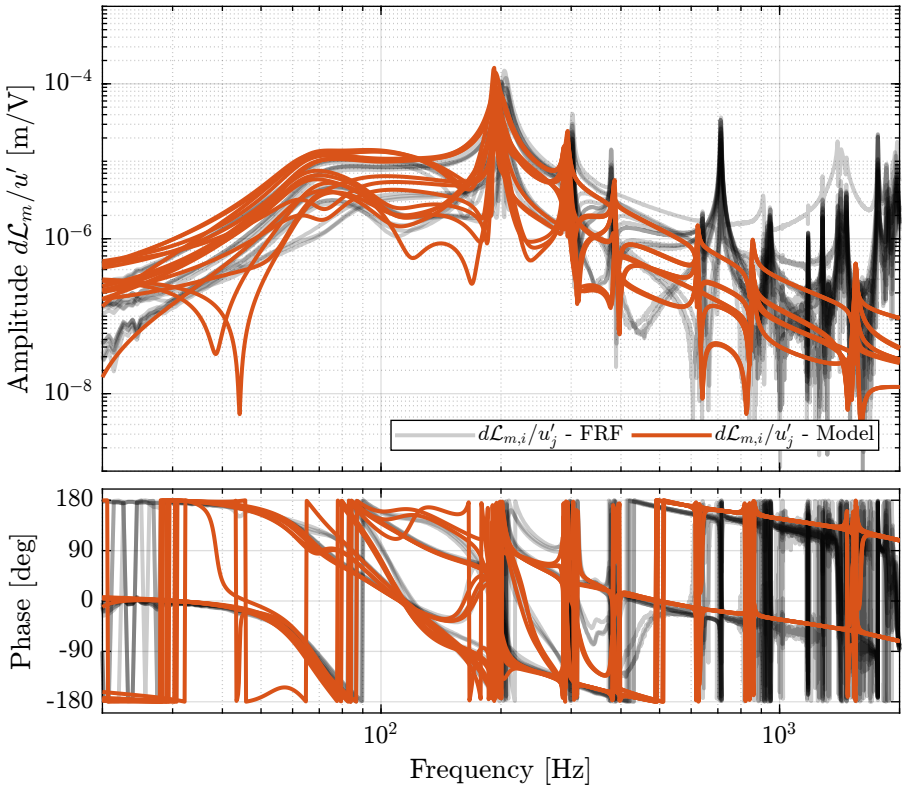

Figure 2.22: Off-diagonal elements of the transfer function from $\boldsymbol{u}'$ to $d\boldsymbol{\mathcal{L}}_m$ - comparison of the measured FRF and the identified dynamics using the flexible model

Important

Using flexible models for the APA, the agreement between the Simscape model of the nano-hexapod and the measured FRF is very good.
Only the flexible mode of the top-plate is not appearing in the model which is very logical as the top plate is taken as a solid body.

2.4.6 Conclusion

Important

The decentralized Integral Force Feedback strategy applied on the nano-hexapod is very effective in damping all the suspension modes.
The Simscape model (especially when using a flexible model for the APA) is shown to be very accurate, even when IFF is applied.

2.5 Modal Analysis

Several 3-axis accelerometers are fixed on the top platform of the nano-hexapod as shown in Figure 2.27.

The top platform is then excited using an instrumented hammer as shown in Figure 2.24.

From this experiment, the resonance frequencies and the associated mode shapes can be computed (Section 2.5.1). Then, in Section 2.5.2, the vertical compliance of the nano-hexapod is experimentally estimated. Finally, in Section 2.5.3, the measured compliance is compare with the estimated one from the Simscape model.

2.5.1 Obtained Mode Shapes

We can observe the mode shapes of the first 6 modes that are the suspension modes (the plate is behaving as a solid body) in Figure 2.25.

Then, there is a mode at 692Hz which corresponds to a flexible mode of the top plate (Figure 2.26).

The obtained modes are summarized in Table 2.1.

2.5.2 Nano-Hexapod Compliance - Effect of IFF

In this section, we wish to estimate the effectiveness of the IFF strategy regarding the compliance.

The top plate is excited vertically using the instrumented hammer two times:

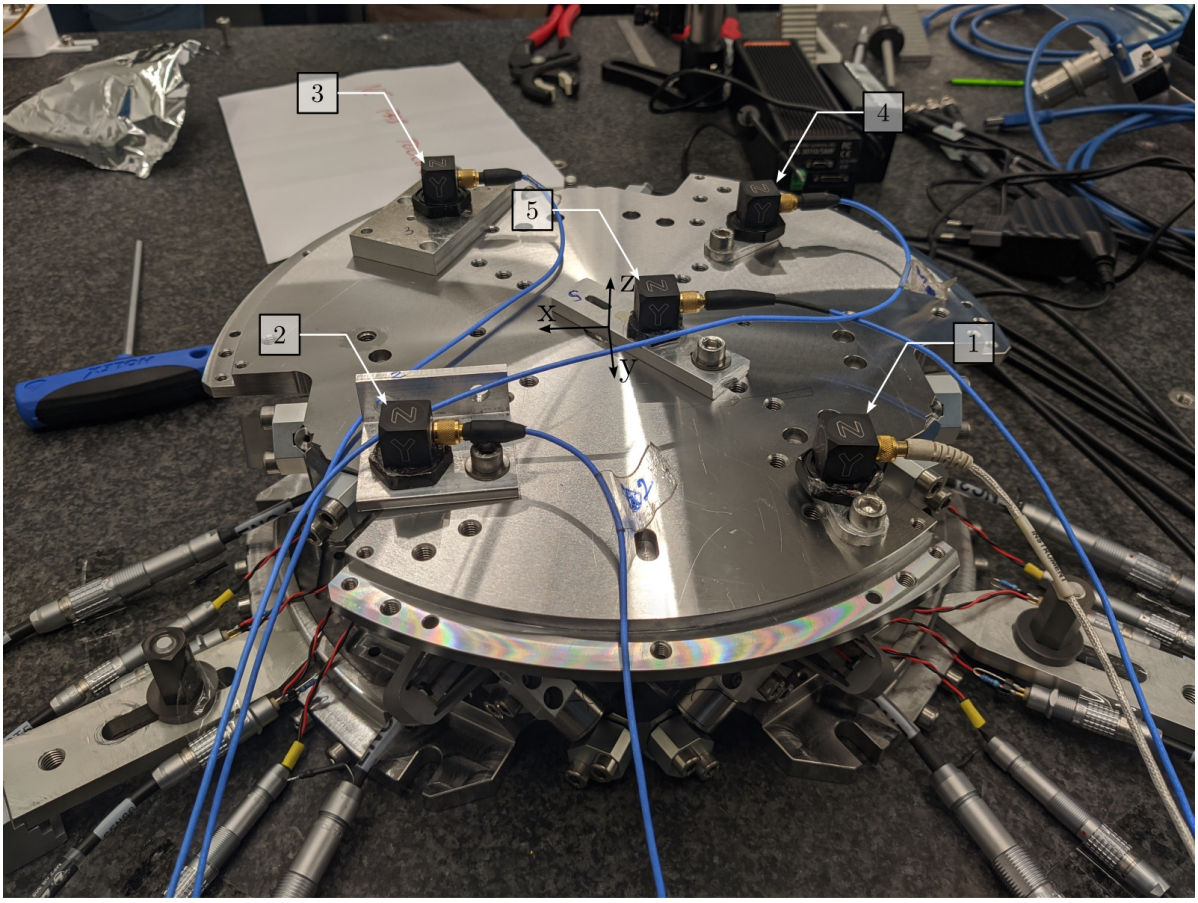

Figure 2.23: Location of the accelerometers on top of the nano-hexapod

Table 2.1: Description of the identified modes

Mode	Freq. [Hz]	Description
1	105	Suspension Mode: Y-translation
2	107	Suspension Mode: X-translation
3	131	Suspension Mode: Z-translation
4	161	Suspension Mode: Y-tilt
5	162	Suspension Mode: X-tilt
6	180	Suspension Mode: Z-rotation
7	692	(flexible) Membrane mode of the top platform

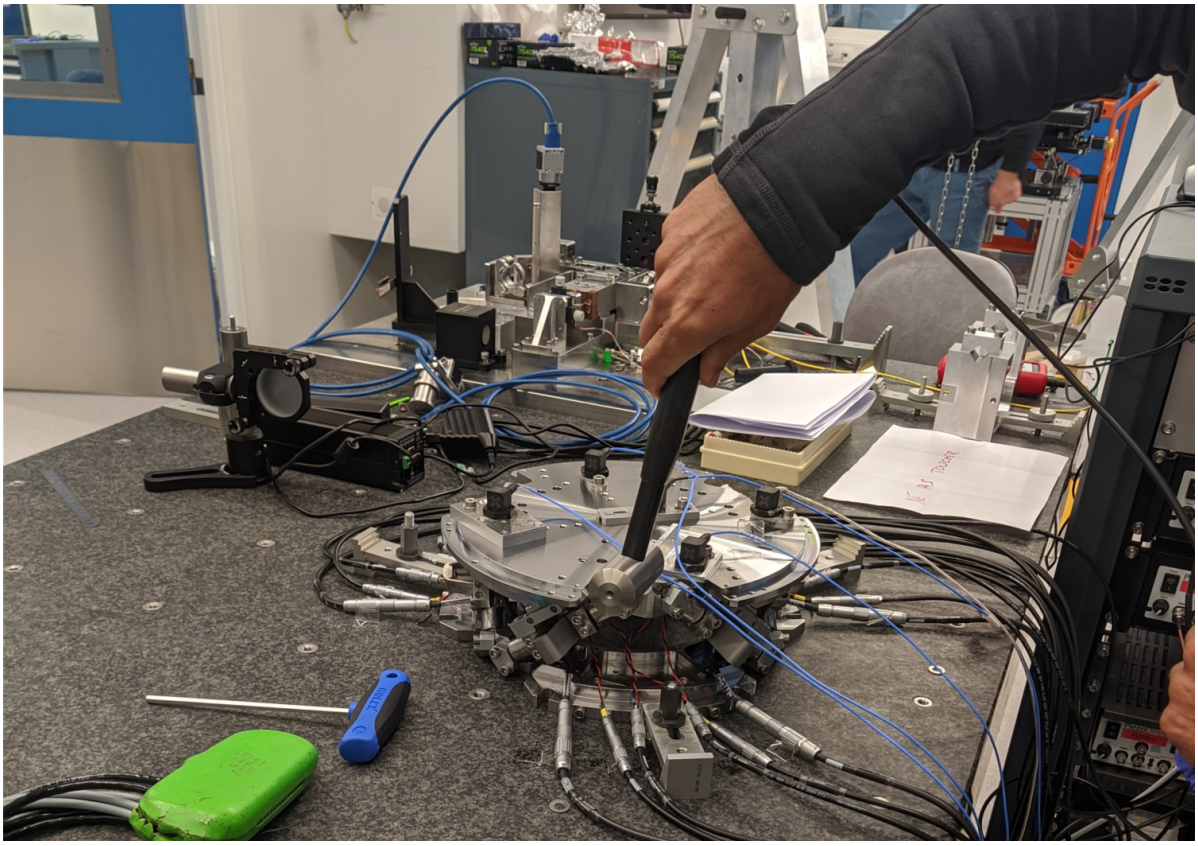

Figure 2.24: Example of an excitation using an instrumented hammer

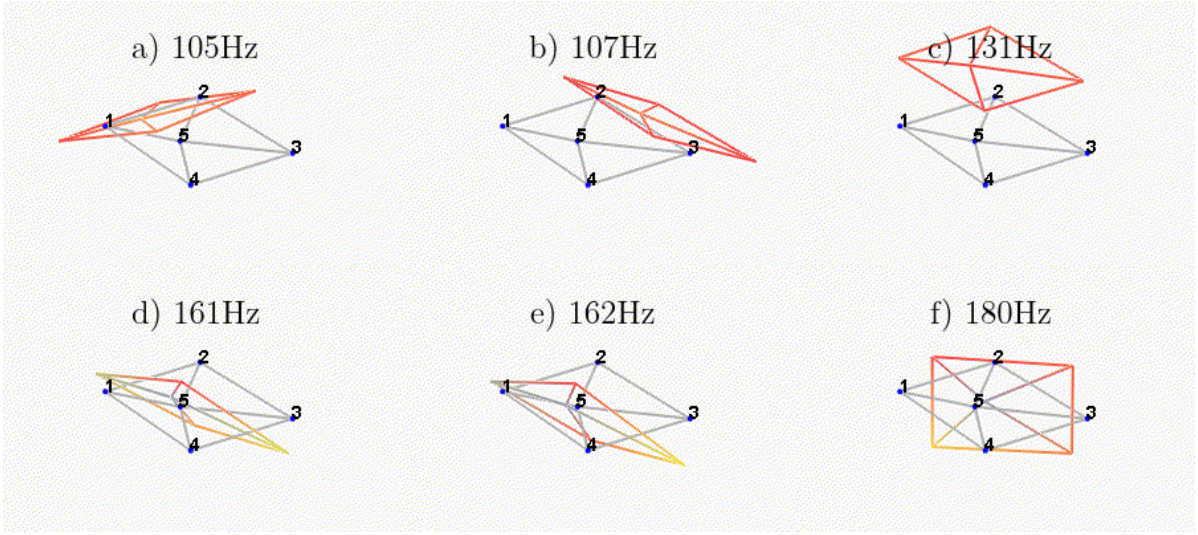

Figure 2.25: Measured mode shapes for the first six modes

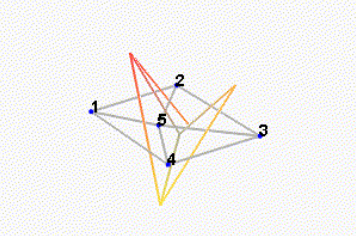

Figure 2.26: First flexible mode at 692Hz

1. no control loop is used

2. decentralized IFF is used

The data are loaded. The mean vertical motion of the top platform is computed by averaging all 5 vertical accelerometers. The vertical compliance (magnitude of the transfer function from a vertical force applied on the top plate to the vertical motion of the top plate) is shown in Figure 2.27.

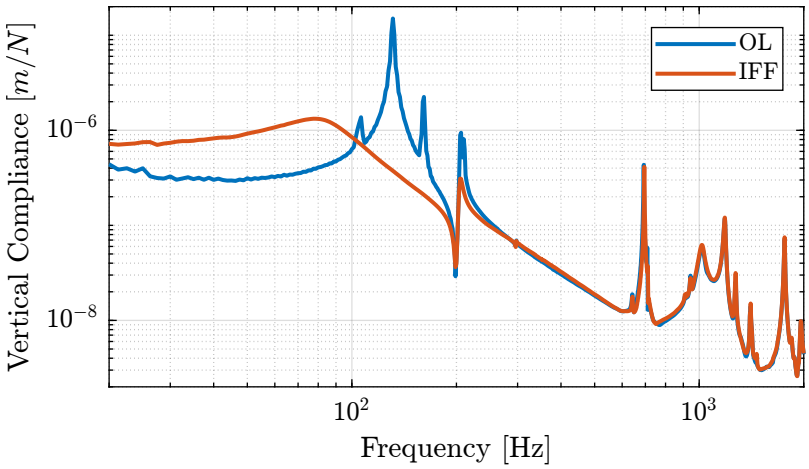

Figure 2.27: Measured vertical compliance with and without IFF

Important

From Figure 2.27, it is clear that the IFF control strategy is very effective in damping the suspensions modes of the nano-hexapod. It also has the effect of (slightly) degrading the vertical compliance at low frequency.
It also seems some damping can be added to the modes at around 205Hz which are flexible modes of the struts.

2.5.3 Comparison with the Simscape Model

Let's initialize the Simscape model such that it corresponds to the experiment. And let's compare the measured vertical compliance with the vertical compliance as estimated from the Simscape model.

The transfer function from a vertical external force to the absolute motion of the top platform is

identified (with and without IFF) using the Simscape model. The comparison is done in Figure 2.28. Again, the model is quite accurate in predicting the (closed-loop) behavior of the system.

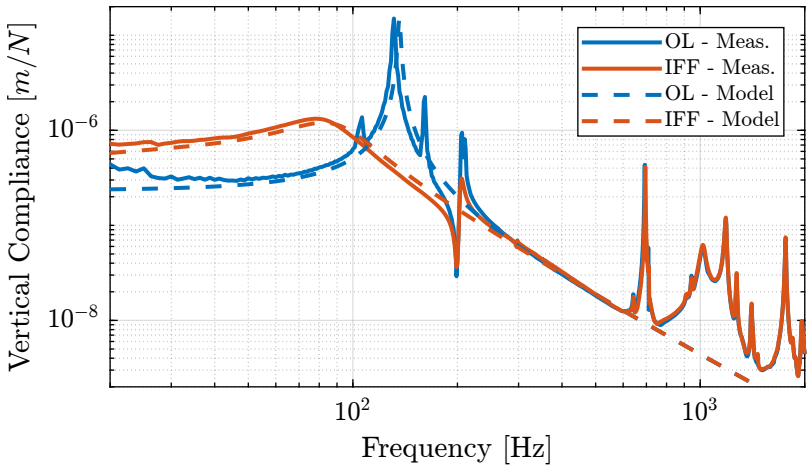

Figure 2.28: Measured vertical compliance with and without IFF

2.6 Conclusion

Important

From the previous analysis, several conclusions can be drawn:

- Decentralized IFF is very effective in damping the "suspension" modes of the nano-hexapod (Figure 2.18)
- Decentralized IFF does not damp the "spurious" modes of the struts nor the flexible modes of the top plate (Figure 2.18)
- Even though the Simscape model and the experimentally measured FRF are in good agreement (Figures 2.21 and 2.22), the obtain dynamics from the control inputs $\boldsymbol{u}$ and the encoders $d\boldsymbol{\mathcal{L}}_m$ is very difficult to control

Therefore, in the following sections, the encoders will be fixed to the plates. The goal is to be less sensitive to the flexible modes of the struts.

3 Encoders fixed to the plates

In this section, the encoders are fixed to the plates rather than to the struts as shown in Figure 3.1.

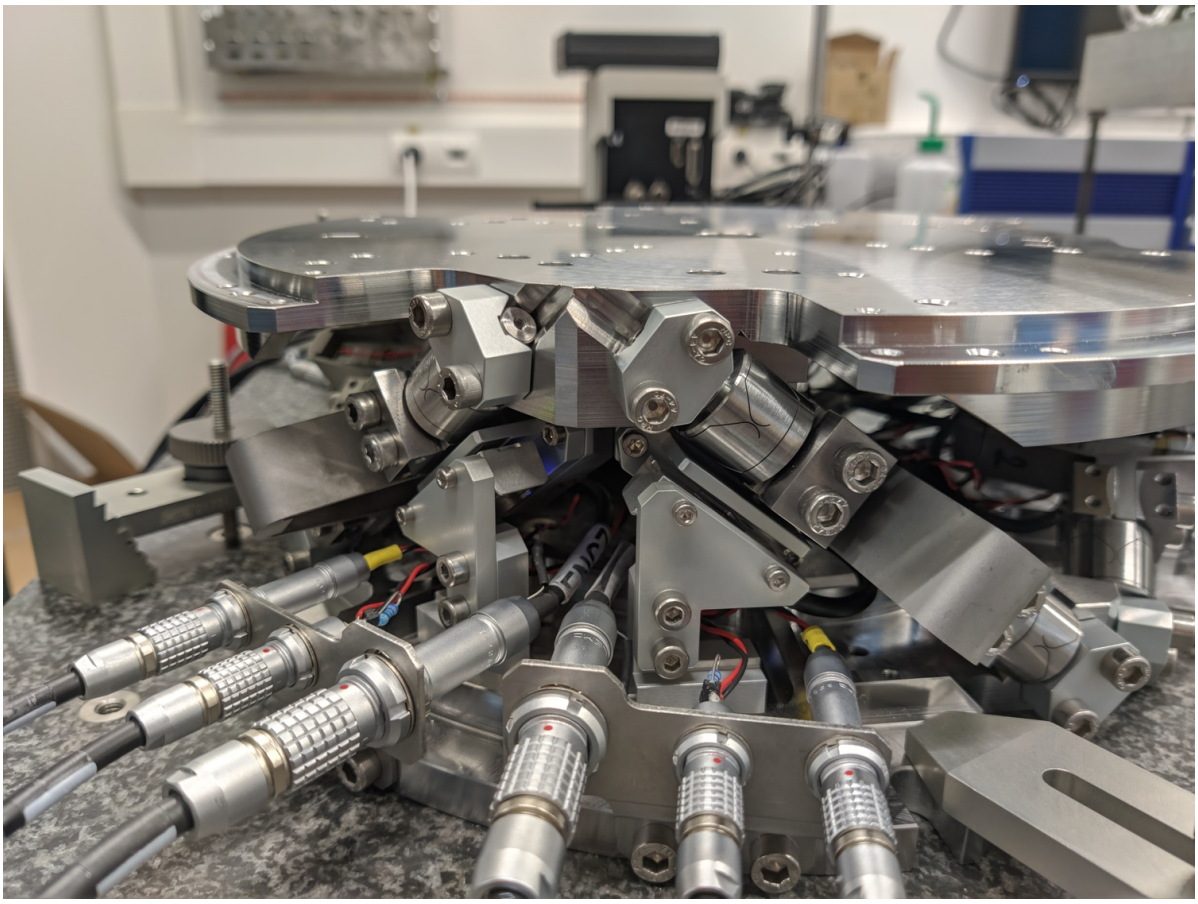

Figure 3.1: Nano-Hexapod with encoders fixed to the struts

It is structured as follow:

- Section 3.1: The dynamics of the nano-hexapod is identified.
- Section 3.2: The identified dynamics is compared with the Simscape model.
- Section 3.3: The Integral Force Feedback (IFF) control strategy is applied and the dynamics of the damped nano-hexapod is identified and compare with the Simscape model.

3.1 Identification of the dynamics

In this section, the dynamics of the nano-hexapod with the encoders fixed to the plates is identified.

First, the measurement data are loaded in Section 3.1.1, then the transfer function matrix from the actuators to the encoders are estimated in Section 3.1.2. Finally, the transfer function matrix from the actuators to the force sensors is estimated in Section 3.1.3.

3.1.1 Data Loading and Spectral Analysis Setup

The actuators are excited one by one using a low pass filtered white noise. For each excitation, the 6 force sensors and 6 encoders are measured and saved.

3.1.2 Transfer function from Actuator to Encoder

The 6x6 transfer function matrix from the excitation voltage $\boldsymbol{u}$ and the displacement $d\boldsymbol{\mathcal{L}}_m$ as measured by the encoders is estimated.

The diagonal and off-diagonal terms of this transfer function matrix are shown in Figure 3.2.

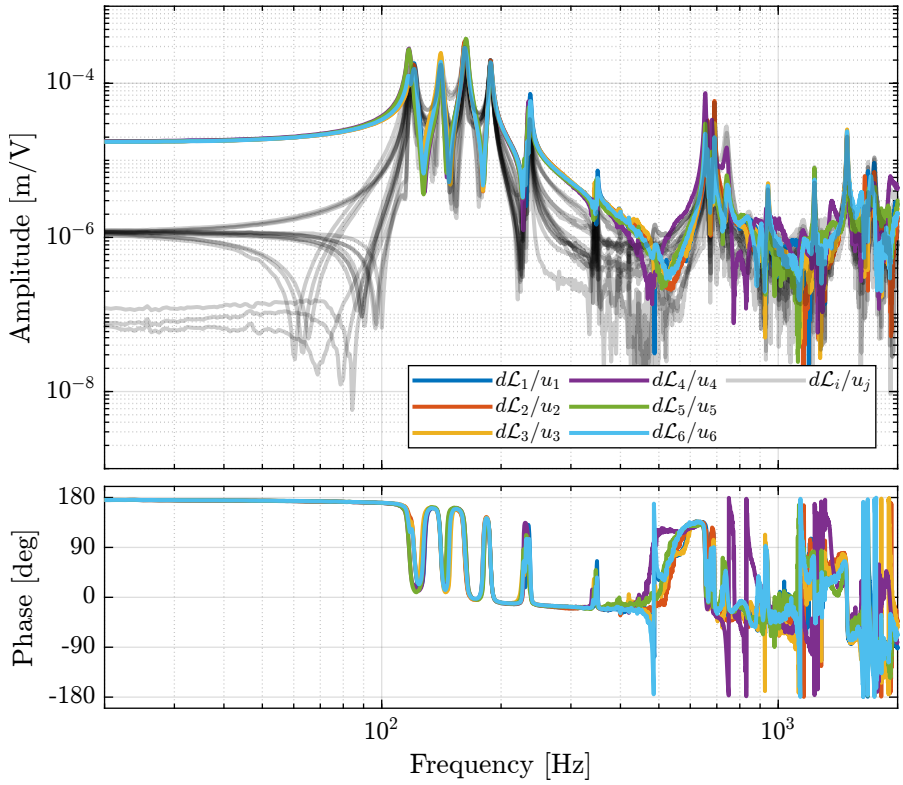

Figure 3.2: Measured FRF for the transfer function from $\boldsymbol{u}$ to $d\boldsymbol{\mathcal{L}}_m$

Important

From Figure 3.2, we can draw few conclusions on the transfer functions from $\boldsymbol{u}$ to $d\boldsymbol{\mathcal{L}}_m$ when the encoders are fixed to the plates:

- the decoupling is rather good at low frequency (below the first suspension mode). The low frequency gain is constant for the off diagonal terms, whereas when the encoders where fixed to the struts, the low frequency gain of the off-diagonal terms were going to zero (Figure 2.1).
- the flexible modes of the struts at 226Hz and 337Hz are indeed shown in the transfer functions, but their amplitudes are rather low.
- the diagonal terms have alternating poles and zeros up to at least 600Hz: the flexible modes of the struts are not affecting the alternating pole/zero pattern. This what not the case when the encoders were fixed to the struts (Figure 2.1).

3.1.3 Transfer function from Actuator to Force Sensor

Then the 6x6 transfer function matrix from the excitation voltage $\boldsymbol{u}$ and the voltage $\boldsymbol{\tau}_m$ generated by the Force senors is estimated. The bode plot of the diagonal and off-diagonal terms are shown in Figure 3.3.

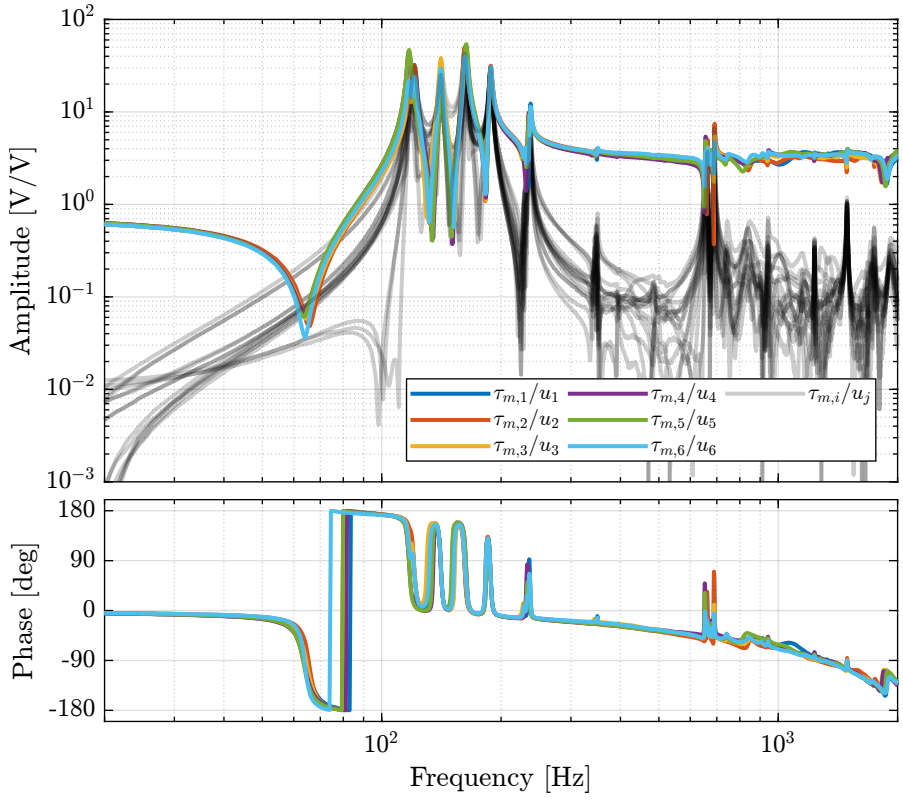

Figure 3.3: Measured FRF for the IFF plant

Important

It is shown in Figure 3.4 that:

- The IFF plant has alternating poles and zeros
- The first flexible mode of the struts as 235Hz is appearing, and therefore is should be possible to add some damping to this mode using IFF
- The decoupling is quite good at low frequency (below the first model) as well as high frequency (above the last suspension mode, except near the flexible modes of the top plate)

3.1.4 Save Identified Plants

The identified dynamics is saved for further use.

3.2 Comparison with the Simscape Model

In this section, the measured dynamics done in Section 3.1 is compared with the dynamics estimated from the Simscape model.

3.2.1 Identification with the Simscape Model

The nano-hexapod is initialized with the APA taken as 2dof models. Then the transfer function from $\boldsymbol{u}$ to $\boldsymbol{\tau}_m$ is identified using the Simscape model. Now, the dynamics from the DAC voltage $\boldsymbol{u}$ to the encoders $d\boldsymbol{\mathcal{L}}_m$ is estimated using the Simscape model. The identified dynamics is saved for further use.

3.2.2 Dynamics from Actuator to Force Sensors

The identified dynamics is compared with the measured FRF:

- Figure 3.4: the individual transfer function from u_1 (the DAC voltage for the first actuator) to the force sensors of all 6 struts are compared
- Figure 3.5: all the diagonal elements are compared
- Figure 3.6: all the off-diagonal elements are compared

3.2.3 Dynamics from Actuator to Encoder

The identified dynamics is compared with the measured FRF:

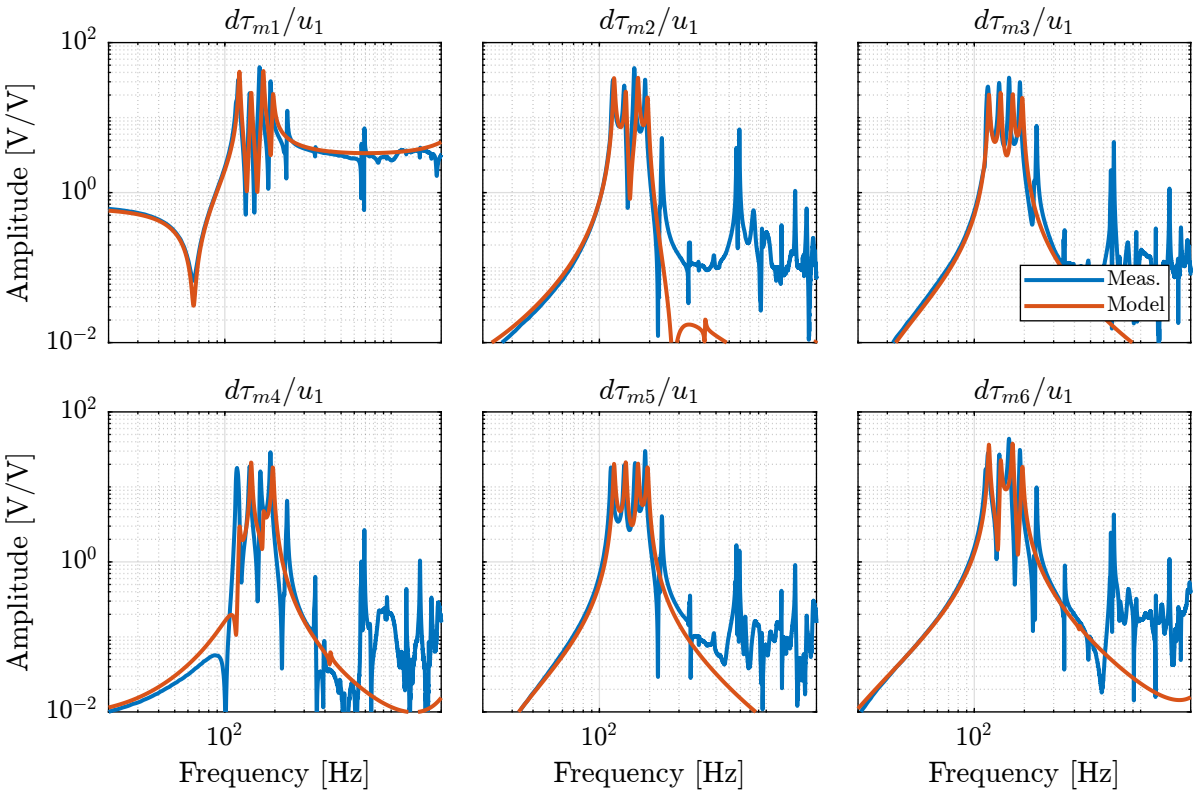

Figure 3.4: IFF Plant for the first actuator input and all the force senosrs

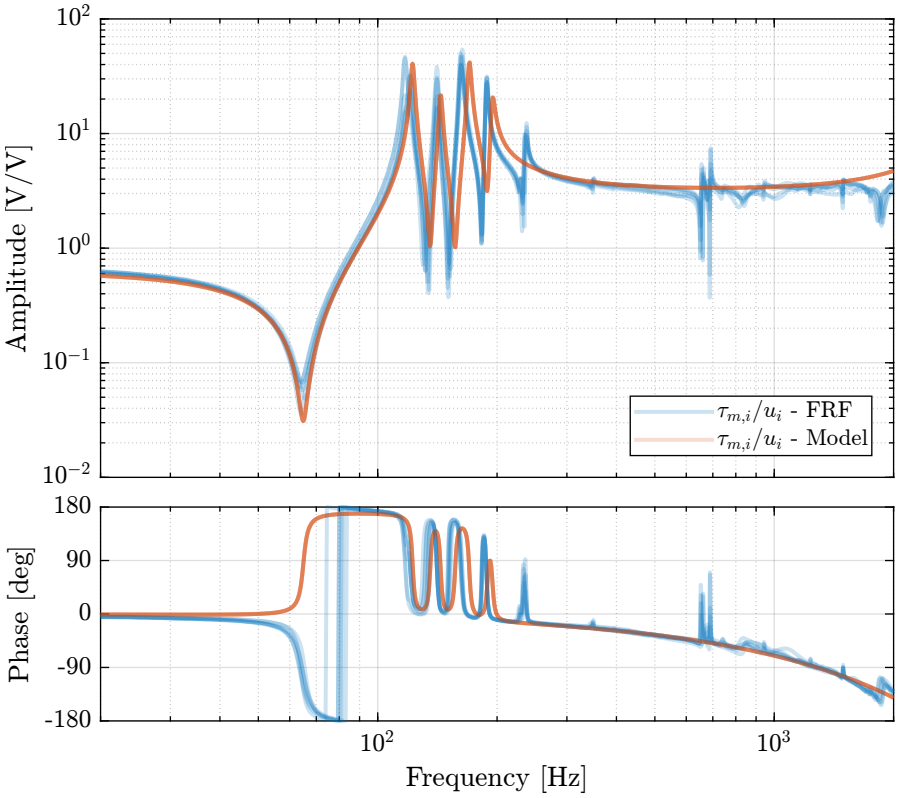

Figure 3.5: Diagonal elements of the IFF Plant

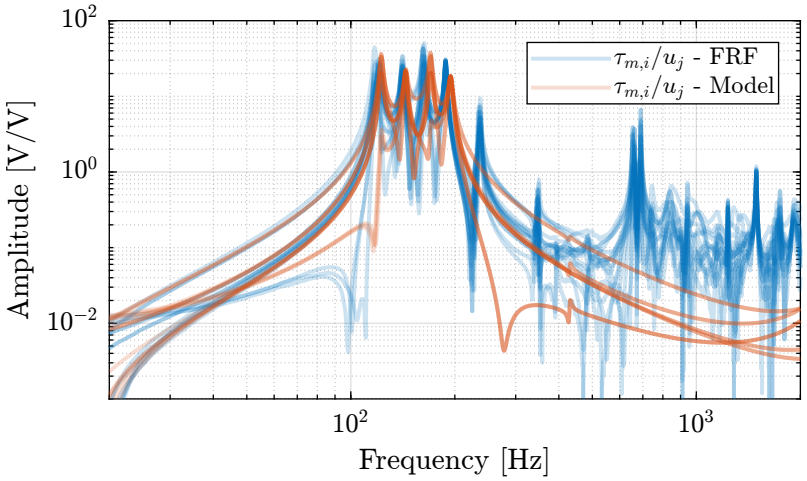

Figure 3.6: Off diagonal elements of the IFF Plant

- Figure 3.7: the individual transfer function from u_3 (the DAC voltage for the actuator number 3) to the six encoders
- Figure 3.8: all the diagonal elements are compared
- Figure 3.9: all the off-diagonal elements are compared

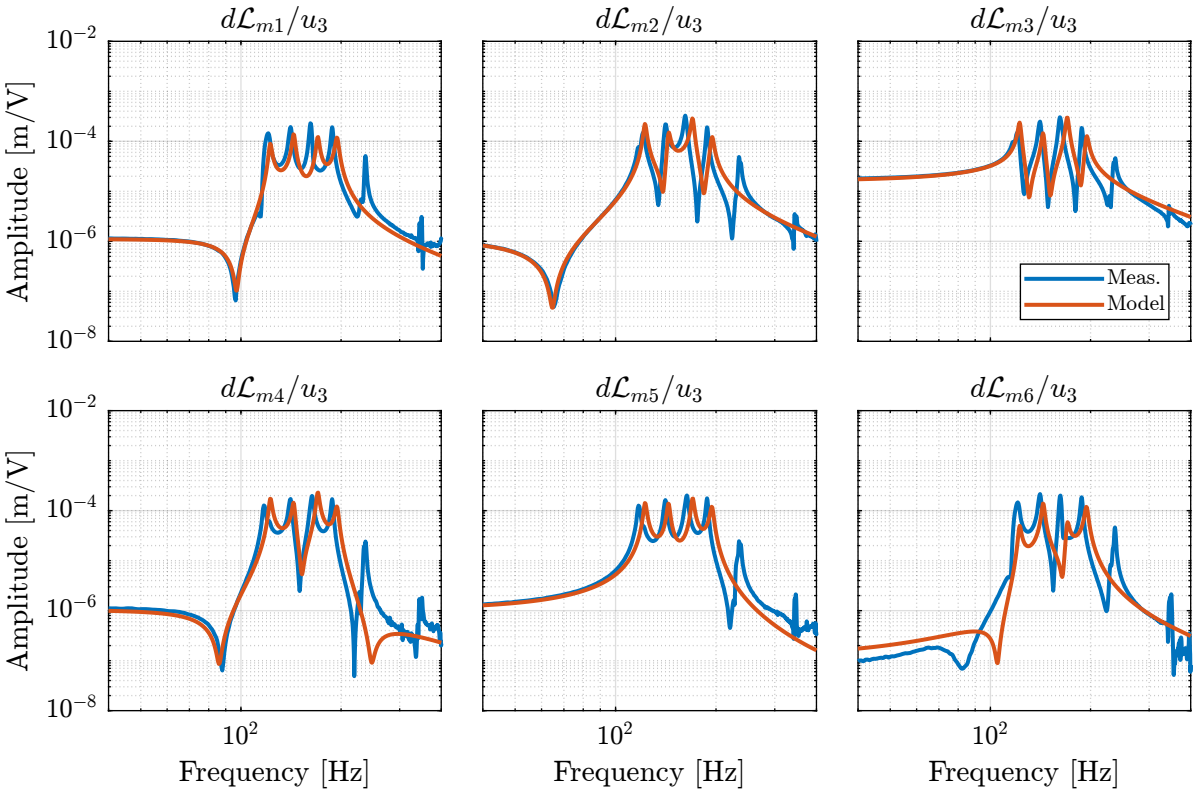

Figure 3.7: DVF Plant for the first actuator input and all the encoders

3.2.4 Conclusion

Important

The Simscape model is quite accurate for the transfer function matrices from $\boldsymbol{u}$ to $\boldsymbol{\tau}_m$ and from $\boldsymbol{u}$ to $d\boldsymbol{\mathcal{L}}_m$ except at frequencies of the flexible modes of the top-plate. The Simscape model can therefore be used to develop the control strategies.

3.3 Integral Force Feedback

In this section, the Integral Force Feedback (IFF) control strategy is applied to the nano-hexapod in order to add damping to the suspension modes.

The control architecture is shown in Figure 3.10:

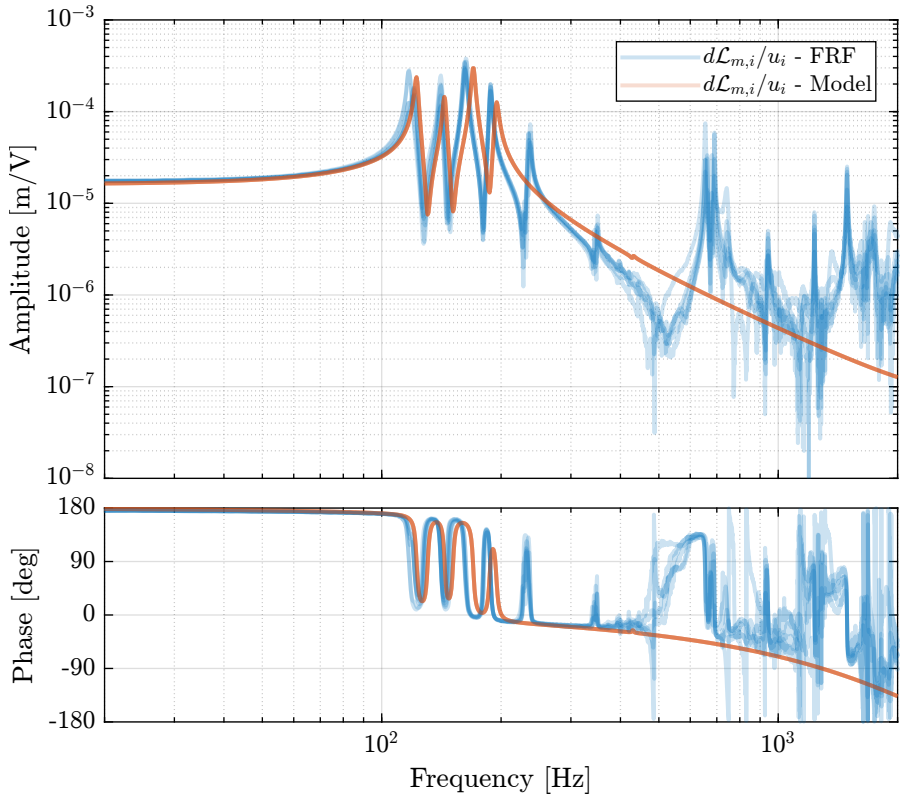

Figure 3.8: Diagonal elements of the DVF Plant

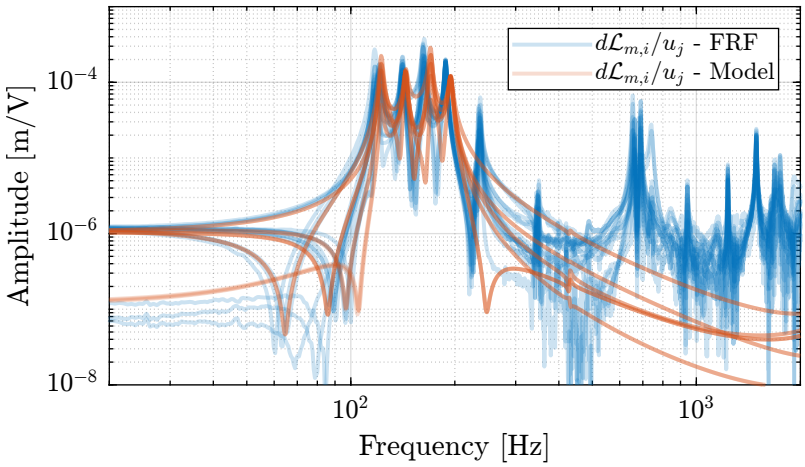

Figure 3.9: Off diagonal elements of the DVF Plant

- $\boldsymbol{\tau}_m$ is the measured voltage of the 6 force sensors
- $\boldsymbol{K}_{\text{IFF}}$ is the 6×6 diagonal controller
- $\boldsymbol{u}$ is the plant input (voltage generated by the 6 DACs)
- $\boldsymbol{u}'$ is the new plant inputs with added damping

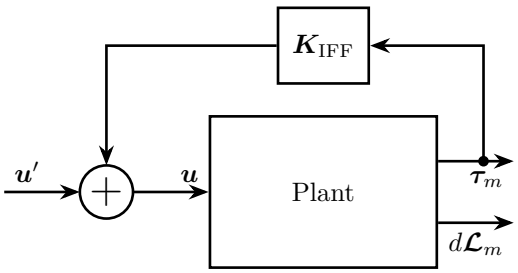

Figure 3.10: Integral Force Feedback Strategy

- Section 3.3.1

3.3.1 Effect of IFF on the plant - Simscape Model

The nano-hexapod is initialized with 2DoF APA and the encoders fixed to the struts. The same controller as the one developed when the encoder were fixed to the struts is used. The transfer function from $\boldsymbol{u}'$ to $d\boldsymbol{\mathcal{L}}_m$ is identified. It is first verified that the system is stable:

Matlab
```
isstable(G_dL)
```

Results
```
1
```

The identified dynamics is saved for further use. The diagonal and off-diagonal terms of the 6×6 transfer function matrices identified are compared in Figure 3.11. It is shown, as was the case when the encoders were fixed to the struts, that the IFF control strategy is very effective in damping the suspension modes of the nano-hexapod.

3.3.2 Effect of IFF on the plant - FRF

The IFF control strategy is experimentally implemented. The (damped) transfer function from $\boldsymbol{u}'$ to $d\boldsymbol{\mathcal{L}}_m$ is experimentally identified.

The identification data are loaded: And the parameters used for the transfer function estimation are defined below. The estimation is performed using the `tfestimate` command. The experimentally identified plant is saved for further use.

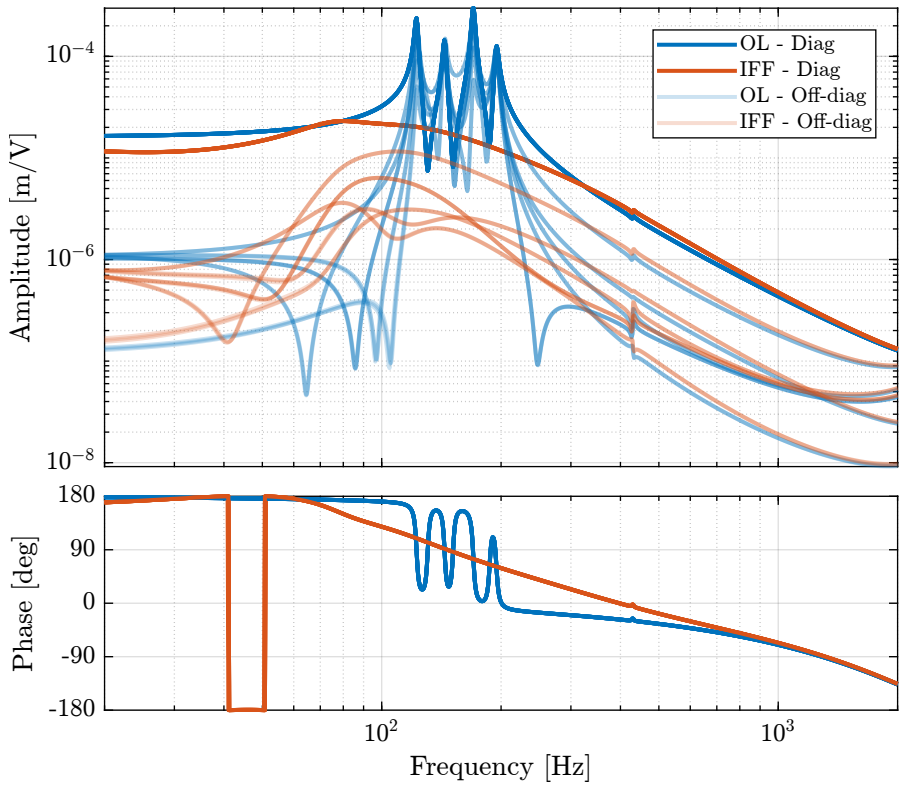

Figure 3.11: Effect of the IFF control strategy on the transfer function from $\boldsymbol{\tau}$ to $d\boldsymbol{\mathcal{L}}_m$

```Matlab
save('matlab/data_frf/damped_plant_enc_plates.mat', 'f', 'Ts', 'G_dL')
```

The obtained diagonal and off-diagonal elements of the transfer function from $\boldsymbol{u}'$ to $d\boldsymbol{\mathcal{L}}_m$ are shown in Figure 3.12 both without and with IFF.

Important

As was predicted with the Simscape model, the IFF control strategy is very effective in damping the suspension modes of the nano-hexapod. Little damping is also applied on the first flexible mode of the strut at 235Hz. However, no damping is applied on other modes, such as the flexible modes of the top plate.

3.3.3 Comparison of the measured FRF and the Simscape model

Let's now compare the obtained damped plants obtained experimentally with the one extracted from Simscape:

- Figure 3.13: the individual transfer function from u_1' to the six encoders are comapred
- Figure 3.14: all the diagonal elements are compared

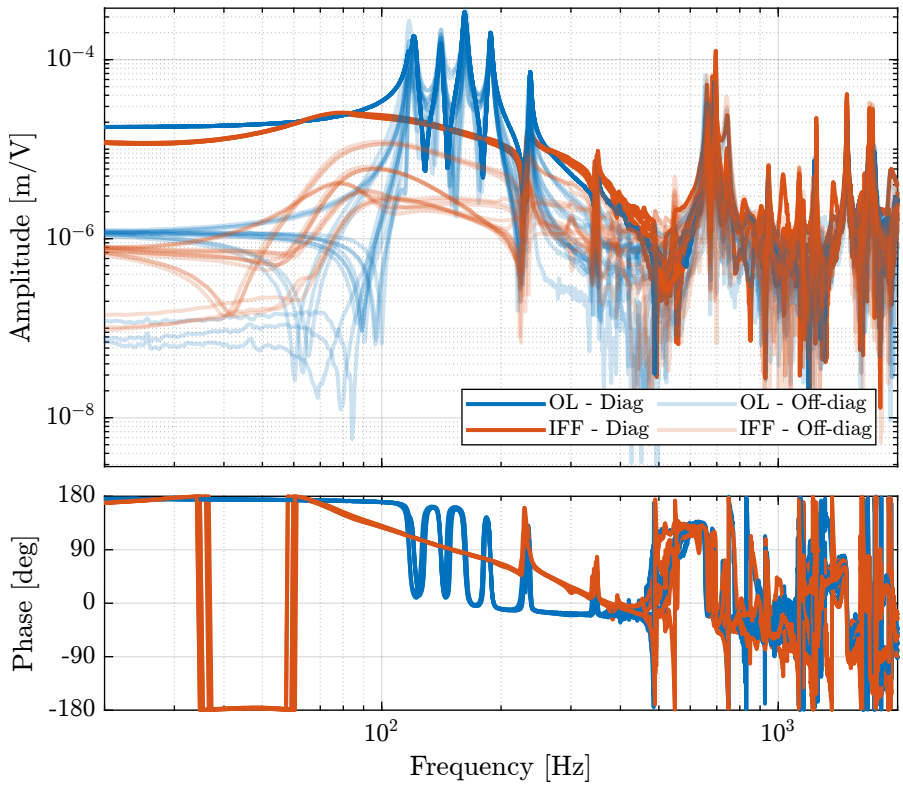

Figure 3.12: Effect of the IFF control strategy on the transfer function from $\boldsymbol{\tau}$ to $d\boldsymbol{\mathcal{L}}_m$

- Figure 3.15: all the off-diagonal elements are compared

Important

From Figures 3.14 and 3.15, it is clear that the Simscape model very well represents the dynamics of the nano-hexapod. This is true to around 400Hz, then the dynamics depends on the flexible modes of the top plate which are not modelled.

3.4 Effect of Payload mass on the Dynamics

In this section, the encoders are fixed to the plates, and we identify the dynamics for several payloads. The added payload are half cylinders, and three layers can be added for a total of around 40kg (Figure 3.16).

First the dynamics from $\boldsymbol{u}$ to $d\mathcal{L}_m$ and $\boldsymbol{\tau}_m$ is identified. Then, the Integral Force Feedback controller is developed and applied as shown in Figure 3.17. Finally, the dynamics from $\boldsymbol{u}'$ to $d\mathcal{L}_m$ is identified and the added damping can be estimated.

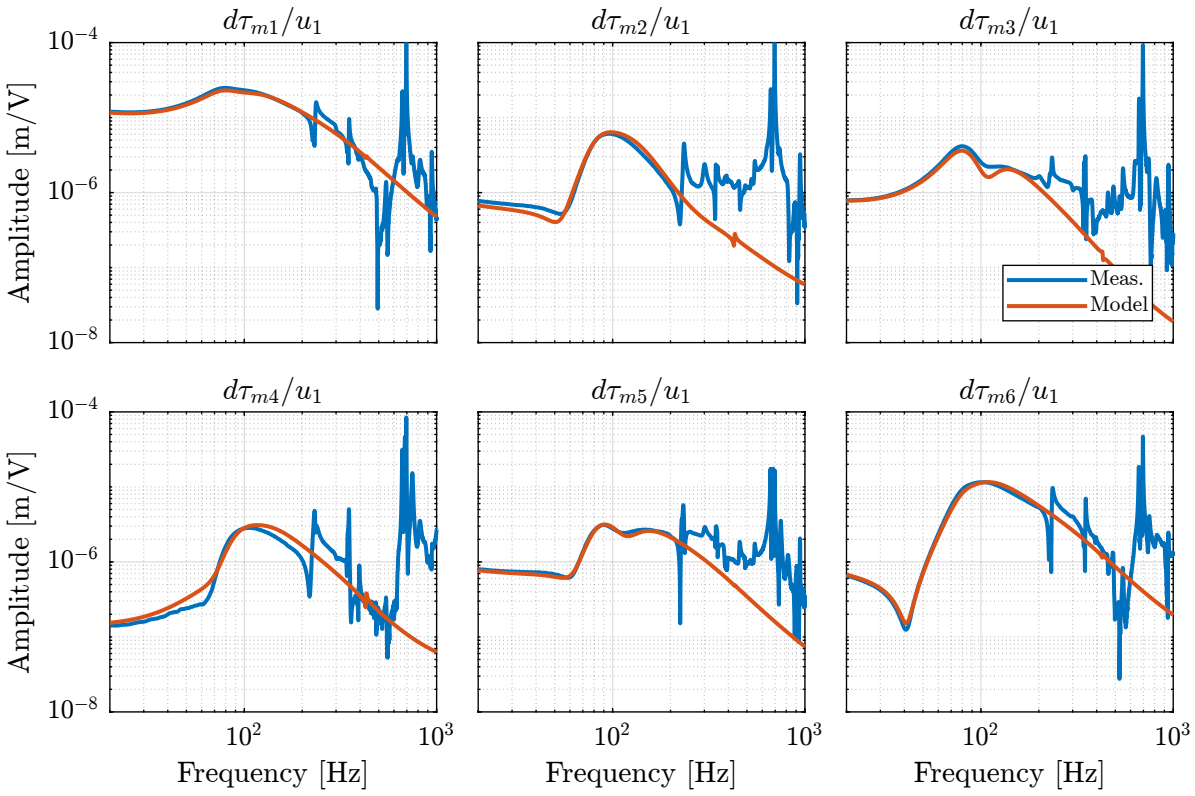

Figure 3.13: FRF from one actuator to all the encoders when the plant is damped using IFF

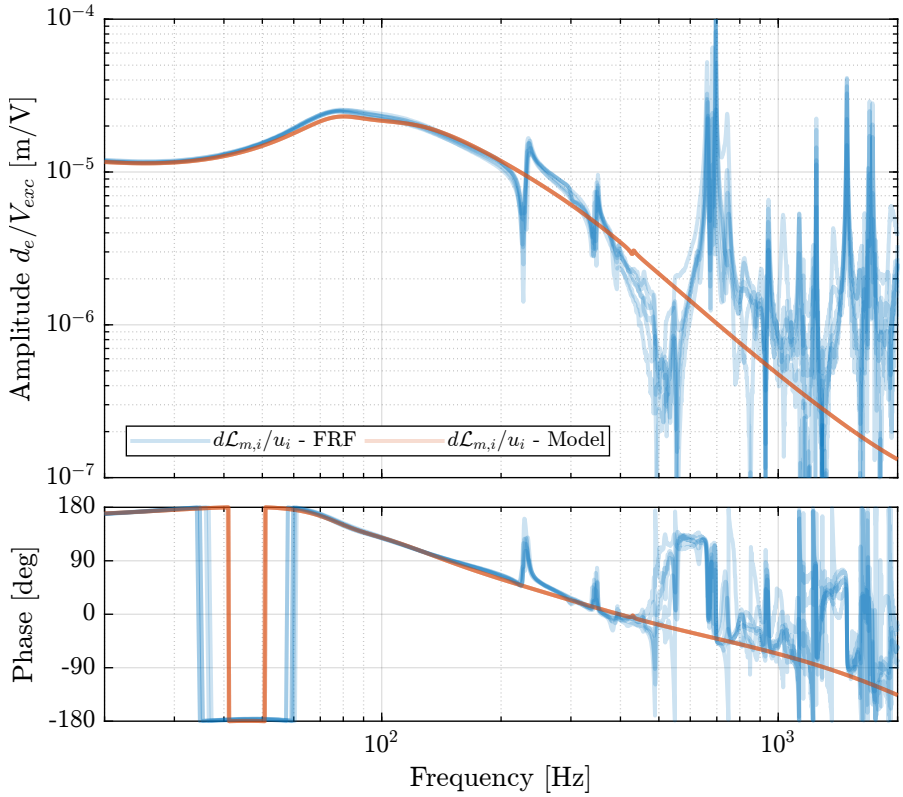

Figure 3.14: Comparison of the diagonal elements of the transfer functions from $\boldsymbol{u}$ to $d\boldsymbol{\mathcal{L}}_m$ with active damping (IFF) applied with an optimal gain $g = 400$

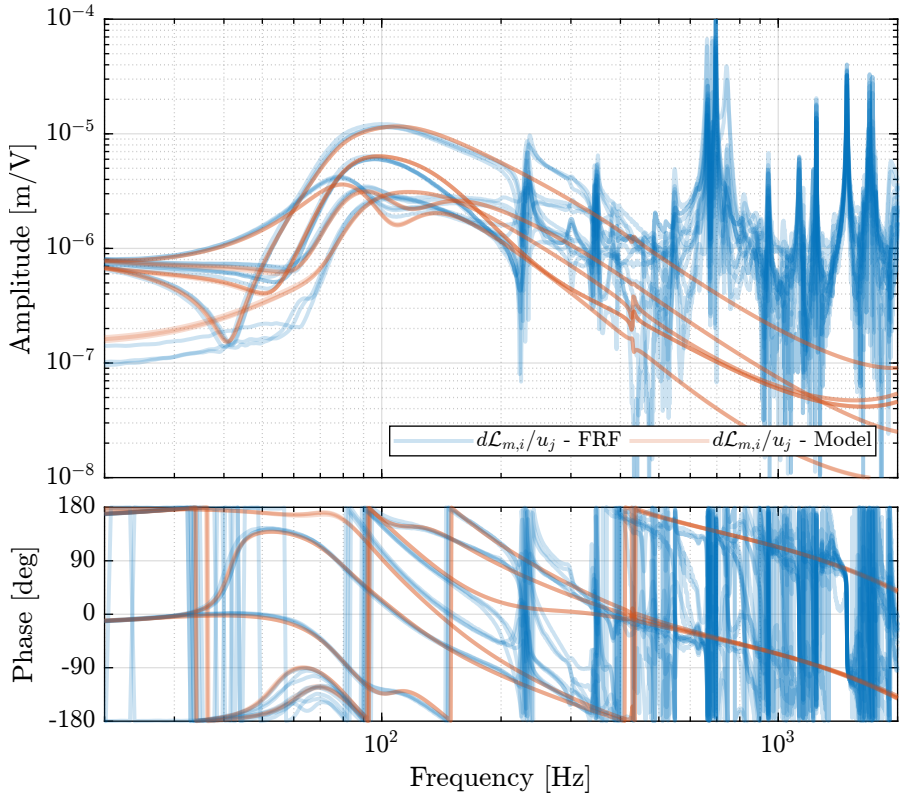

Figure 3.15: Comparison of the off-diagonal elements of the transfer functions from $\boldsymbol{u}$ to $d\boldsymbol{\mathcal{L}}_m$ with active damping (IFF) applied with an optimal gain $g = 400$

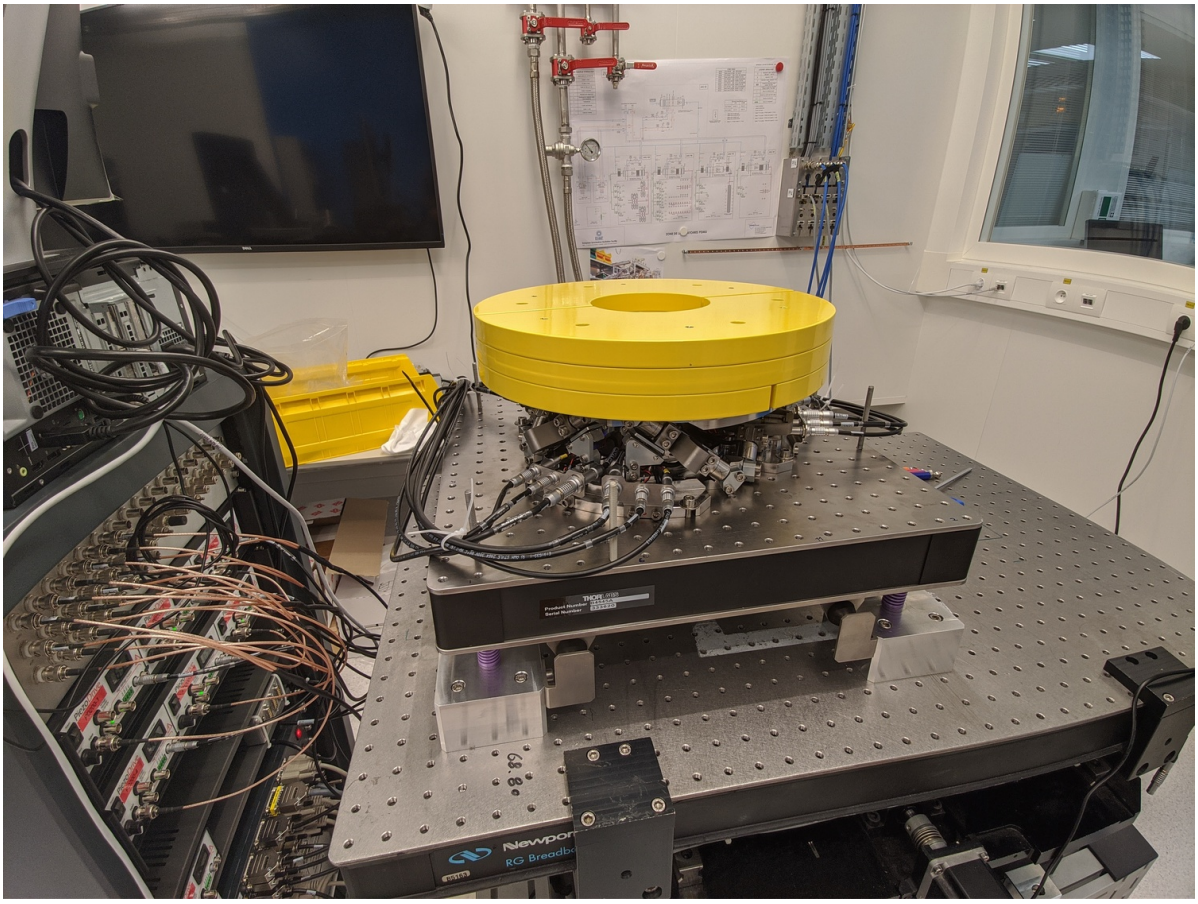

Figure 3.16: Picture of the nano-hexapod with added mass

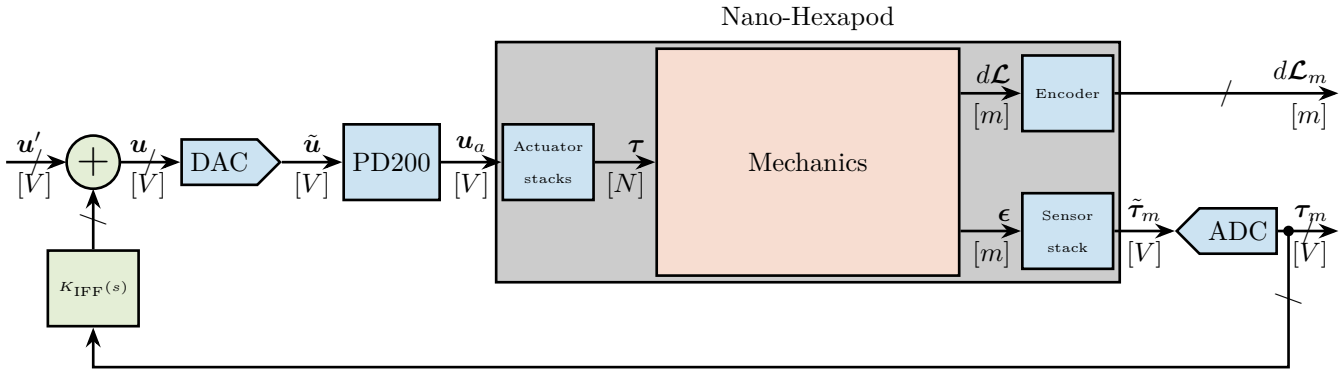

Figure 3.17: Block Diagram of the experimental setup and model

3.4.1 Measured Frequency Response Functions

The following data are loaded:

- `Va`: the excitation voltage (corresponding to u_i)
- `Vs`: the generated voltage by the 6 force sensors (corresponding to $\boldsymbol{\tau}_m$)
- `de`: the measured motion by the 6 encoders (corresponding to $d\boldsymbol{\mathcal{L}}_m$)

The window `win` and the frequency vector `f` are defined. Finally the 6×6 transfer function matrices from $\boldsymbol{u}$ to $d\boldsymbol{\mathcal{L}}_m$ and from $\boldsymbol{u}$ to $\boldsymbol{\tau}_m$ are identified: The identified dynamics are then saved for further use.

3.4.2 Rigidification of the added payloads

figure

The window `win` and the frequency vector `f` are defined. Finally the 6×6 transfer function matrices from $\boldsymbol{u}$ to $d\boldsymbol{\mathcal{L}}_m$ and from $\boldsymbol{u}$ to $\boldsymbol{\tau}_m$ are identified:

3.4.3 Transfer function from Actuators to Encoders

The transfer functions from $\boldsymbol{u}$ to $d\boldsymbol{\mathcal{L}}_m$ are shown in Figure 3.18.

Important

From Figure 3.18, we can observe few things:

- The obtained dynamics is changing a lot between the case without mass and when there is at least one added mass.
- Between 1, 2 and 3 added masses, the dynamics is not much different, and it would be easier to design a controller only for these cases.
- The flexible modes of the top plate is first decreased a lot when the first mass is added (from 700Hz to 400Hz). This is due to the fact that the added mass is composed of two half cylinders which are not fixed together. Therefore is adds a lot of mass to the top plate without adding a lot of rigidity in one direction. When more than 1 mass layer is added, the half cylinders are added with some angles such that rigidity are added in all directions (see Figure 3.16). In that case, the frequency of these flexible modes are increased. In practice, the payload should be one solid body, and we should not see a massive decrease of the frequency of this flexible mode.
- Flexible modes of the top plate are becoming less problematic as masses are added.
- First flexible mode of the strut at 230Hz is not much decreased when mass is added. However, its apparent amplitude is much decreased.

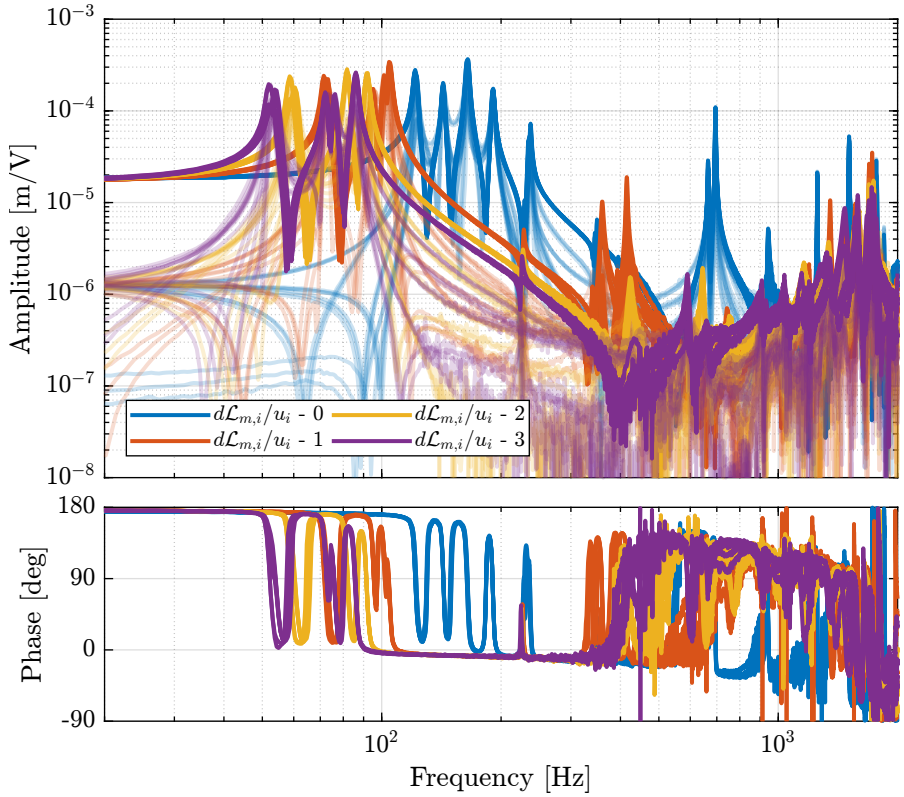

Figure 3.18: Measured Frequency Response Functions from u_i to $d\mathcal{L}_{m,i}$ for all 4 payload conditions. Diagonal terms are solid lines, and shaded lines are off-diagonal terms.

3.4.4 Transfer function from Actuators to Force Sensors

The transfer functions from $\boldsymbol{u}$ to $\boldsymbol{\tau}_m$ are shown in Figure 3.19.

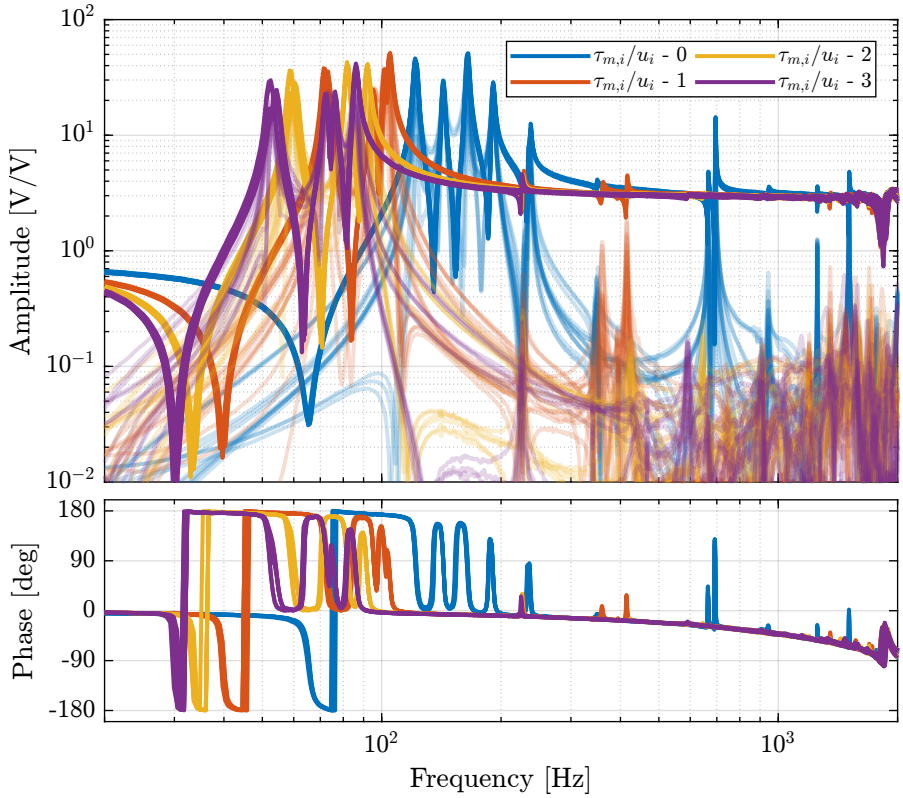

Figure 3.19: Measured Frequency Response Functions from u_i to $\tau_{m,i}$ for all 4 payload conditions. Diagonal terms are solid lines, and shaded lines are off-diagonal terms.

Important

From Figure 3.19, we can see that for all added payloads, the transfer function from $\boldsymbol{u}$ to $\boldsymbol{\tau}_m$ always has alternating poles and zeros.

3.4.5 Coupling of the transfer function from Actuator to Encoders

The RGA-number, which is a measure of the interaction in the system, is computed for the transfer function matrix from $\boldsymbol{u}$ to $d\boldsymbol{\mathcal{L}}_m$ for all the payloads. The obtained numbers are compared in Figure 3.20.

Important

From Figure 3.20, it is clear that the coupling is quite large starting from the first suspension mode of the nano-hexapod. Therefore, is the payload's mass is increase, the coupling in the system start to become unacceptably large at lower frequencies.

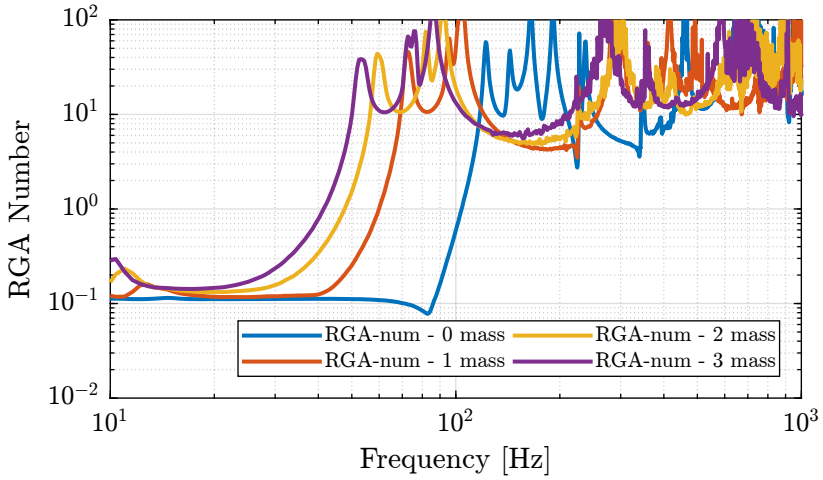

Figure 3.20: RGA-number for the open-loop transfer function from $\boldsymbol{u}$ to $d\boldsymbol{\mathcal{L}}_m$

3.5 Comparison with the Simscape model

Let's now compare the identified dynamics with the Simscape model. We wish to verify if the Simscape model is still accurate for all the tested payloads.

3.5.1 System Identification

Let's initialize the simscape model with the nano-hexapod fixed on top of the vibration table. First perform the identification for the transfer functions from $\boldsymbol{u}$ to $d\boldsymbol{\mathcal{L}}_m$: The identified dynamics are then saved for further use.

3.5.2 Transfer function from Actuators to Encoders

The measured FRF and the identified dynamics from u_i to $d\mathcal{L}_{m,i}$ are compared in Figure 3.21. A zoom near the "suspension" modes is shown in Figure 3.22.

Important

The Simscape model is very accurately representing the measured dynamics up. Only the flexible modes of the struts and of the top plate are not represented here as these elements are modelled as rigid bodies.

3.5.3 Transfer function from Actuators to Force Sensors

The measured FRF and the identified dynamics from u_i to $\tau_{m,i}$ are compared in Figure 3.23. A zoom near the "suspension" modes is shown in Figure 3.24.

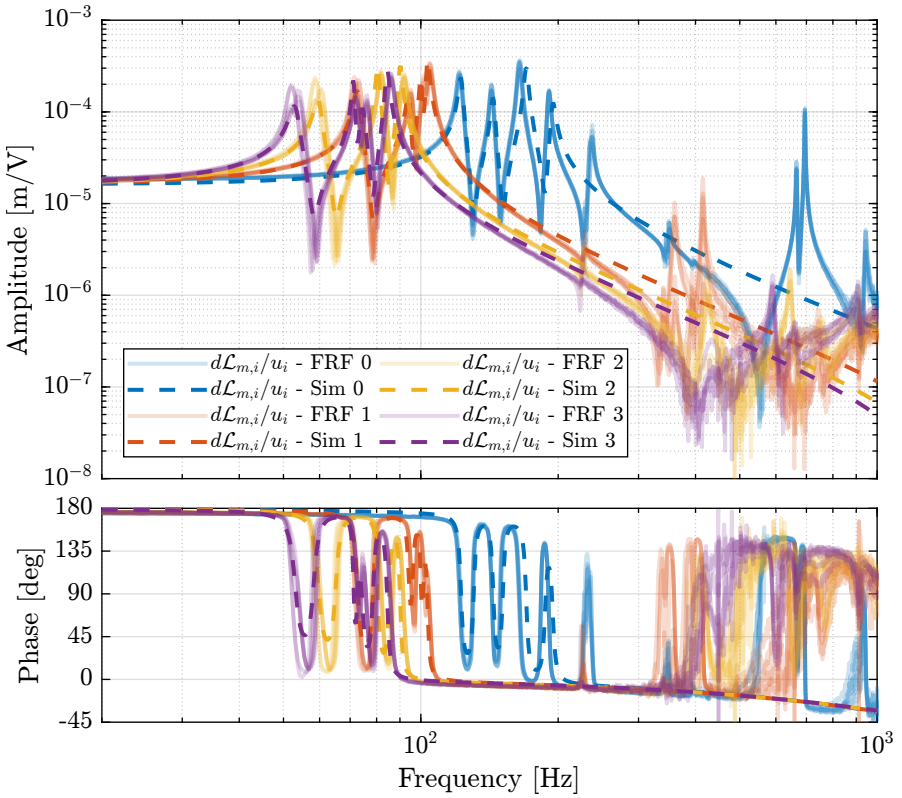

Figure 3.21: Comparison of the transfer functions from u_i to $d\mathcal{L}_{m,i}$ - measured FRF and identification from the Simscape model

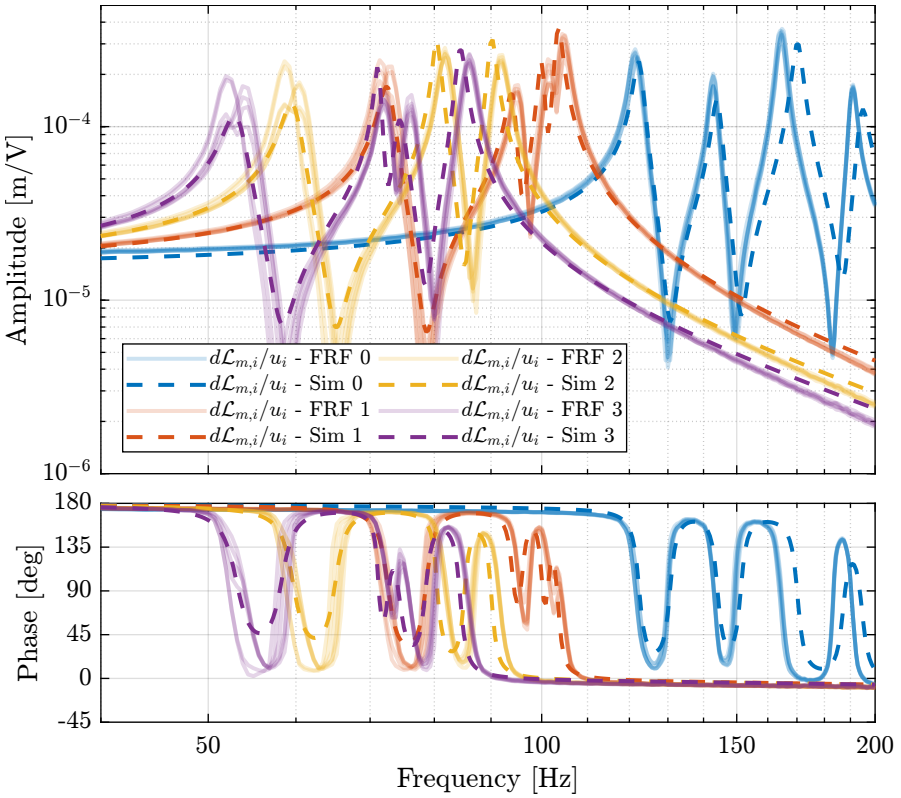

Figure 3.22: Comparison of the transfer functions from u_i to $d\mathcal{L}_{m,i}$ - measured FRF and identification from the Simscape model (Zoom)

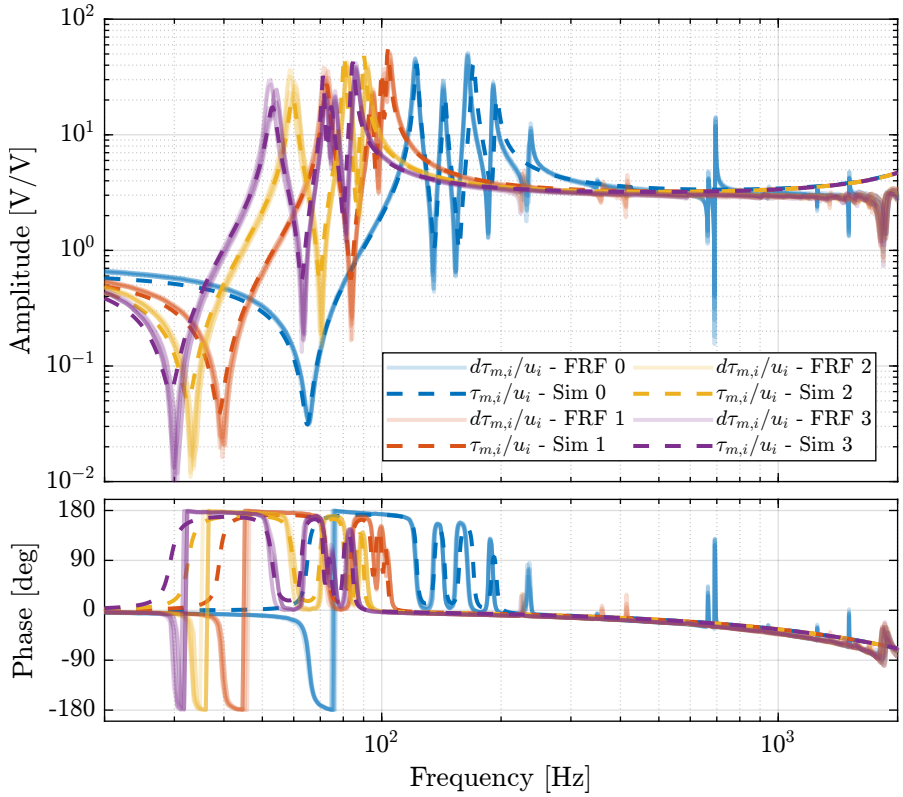

Figure 3.23: Comparison of the transfer functions from u_i to $\tau_{m,i}$ - measured FRF and identification from the Simscape model

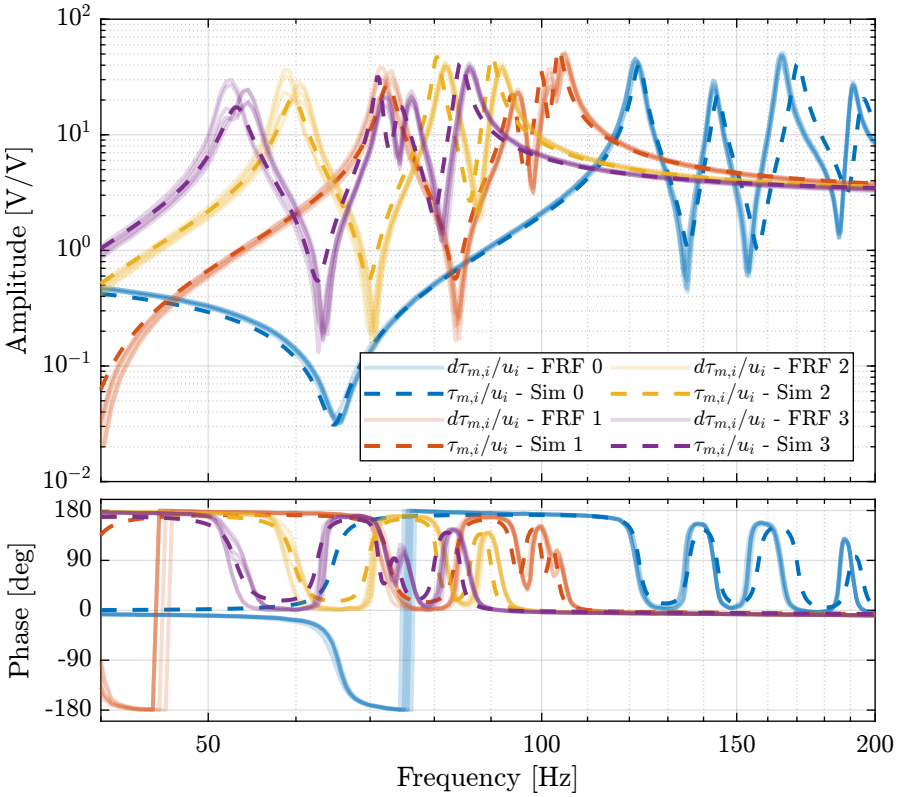

Figure 3.24: Comparison of the transfer functions from u_i to $\tau_{m,i}$ - measured FRF and identification from the Simscape model (Zoom)

3.6 Integral Force Feedback Controller

In this section, we wish to develop the Integral Force Feedback controller that is robust with respect to the added payload.

3.6.1 Robust IFF Controller

Based on the measured FRF from $\boldsymbol{u}$ to $\boldsymbol{\tau}_m$, the following IFF controller is developed: Then, the Root Locus plot of Figure 3.25 is used to estimate the optimal gain. This Root Locus plot is computed from the Simscape model.

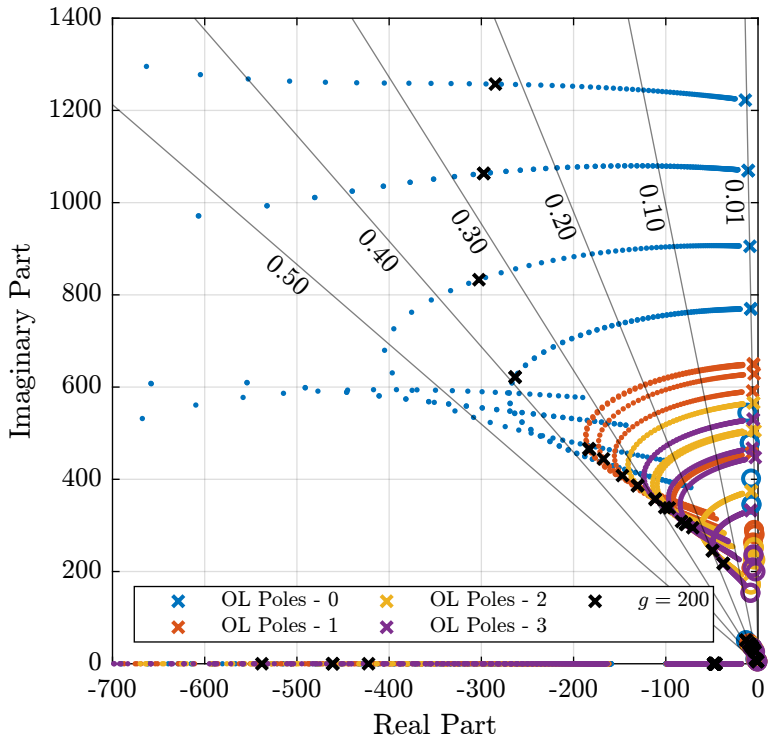

Figure 3.25: Root Locus for the IFF control strategy (for all payload conditions).

The found optimal IFF controller is: It is saved for further use. The corresponding experimental loop gains are shown in Figure 3.26.

Important

Based on the above analysis:

- The same IFF controller can be used to damp the suspension modes for all payload conditions
- The IFF controller should be robust

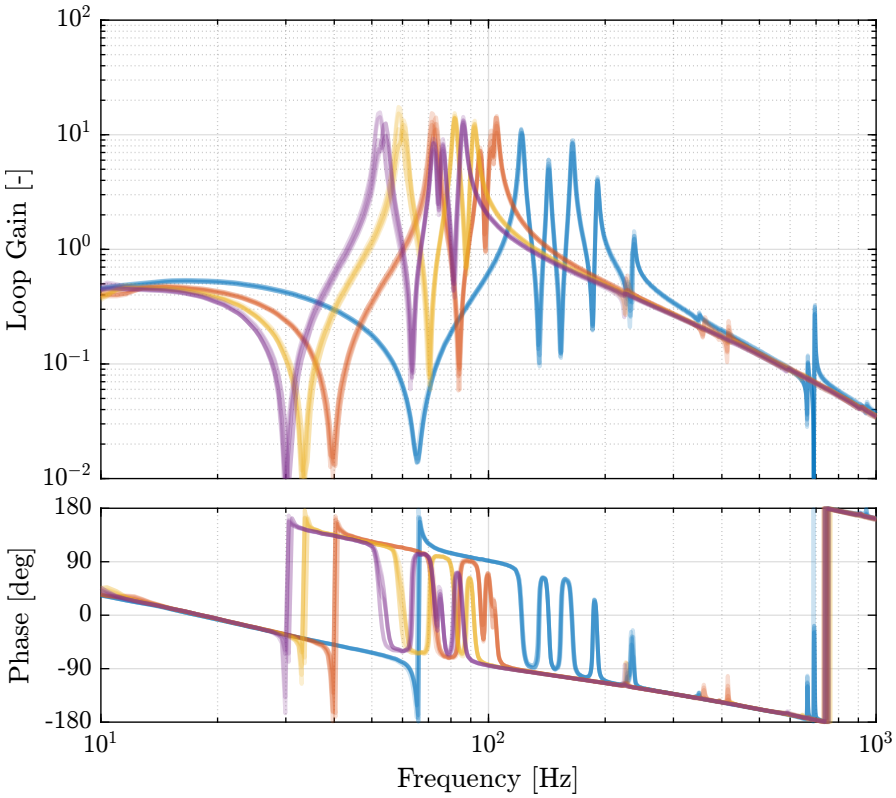

Figure 3.26: Loop gain for the Integral Force Feedback controller

3.6.2 Estimated Damped Plant from the Simscape model

Let's initialize the simscape model with the nano-hexapod fixed on top of the vibration table. And Load the IFF controller. Finally, let's identify the damped plant from $\boldsymbol{u}'$ to $d\boldsymbol{\mathcal{L}}_m$ for all payloads. The identified dynamics are then saved for further use.

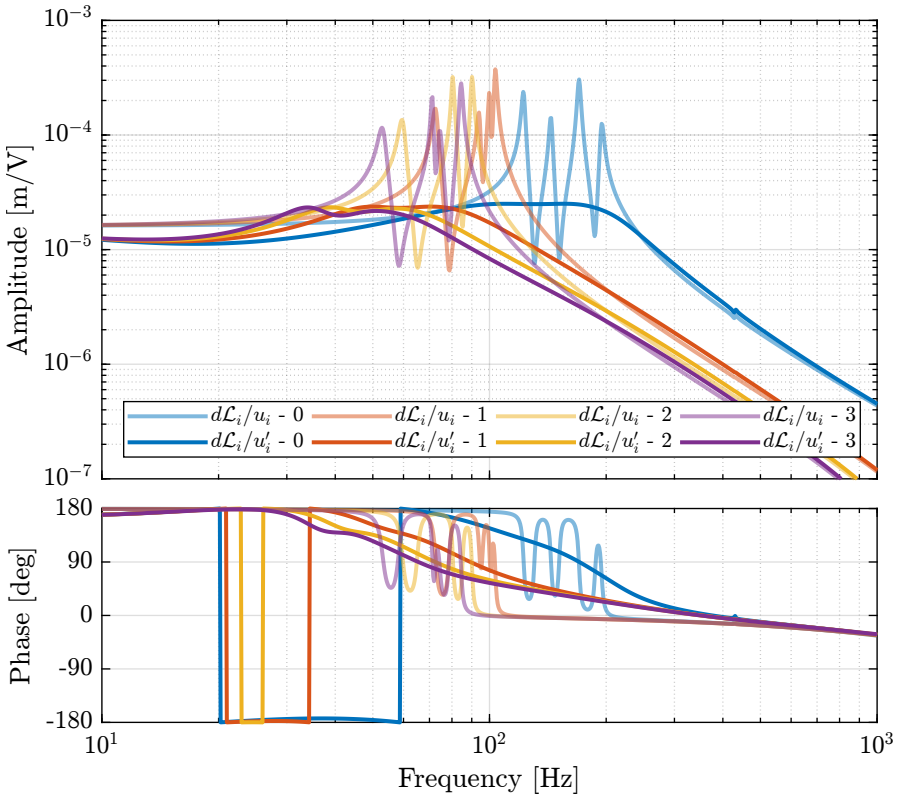

Figure 3.27: Transfer function from u_i to $d\mathcal{L}_{m,i}$ (without active damping) and from u'_i to $d\mathcal{L}_{m,i}$ (with IFF)

3.6.3 Compute the identified FRF with IFF

Several experimental identifications are done in order to identify the dynamics from $\boldsymbol{u}'$ to $d\boldsymbol{\mathcal{L}}_m$ with the robust IFF controller implemented and with various payloads.

The following data are loaded:

- `Va`: the excitation voltage for the damped plant (corresponding to u'_i)
- `de`: the measured motion by the 6 encoders (corresponding to $d\boldsymbol{\mathcal{L}}_m$)

The window `win` and the frequency vector `f` are defined. Finally the 6×6 transfer function matrix from $\boldsymbol{u}'$ to $d\boldsymbol{\mathcal{L}}_m$ is estimated: The identified dynamics are then saved for further use.

3.6.4 Comparison of the measured FRF and the Simscape model

The following figures are computed:

- Figure 3.28: the measured damped FRF are displayed
- Figure 3.29: the open-loop and damped FRF are compared (diagonal elements)
- Figure 3.30: the obtained damped FRF is compared with the identified damped from using the Simscape model

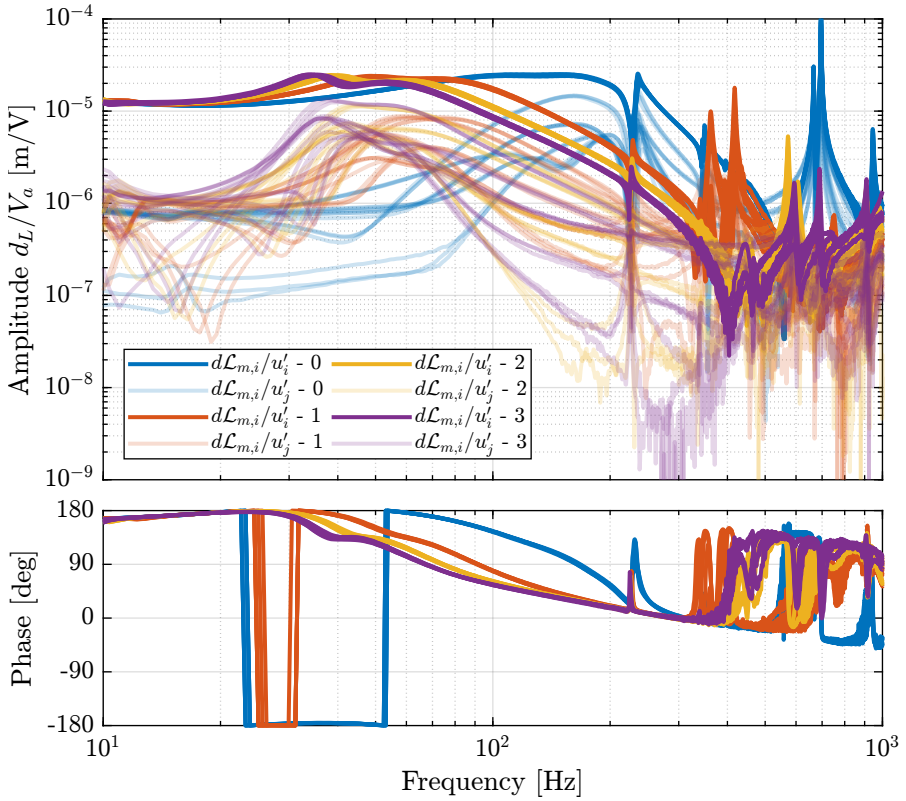

Figure 3.28: Diagonal and off-diagonal of the measured FRF matrix for the damped plant

Important

The IFF control strategy effectively damps all the suspensions modes of the nano-hexapod whatever the payload is. The obtained plant is easier to control (provided the flexible modes of the top platform are well damped).

3.6.5 Change of coupling with IFF

Let's see how the Integral Force Feedback is changing the interaction in the system.

To study that, the RGA-number are computed both for the undamped plant and for the damped plant

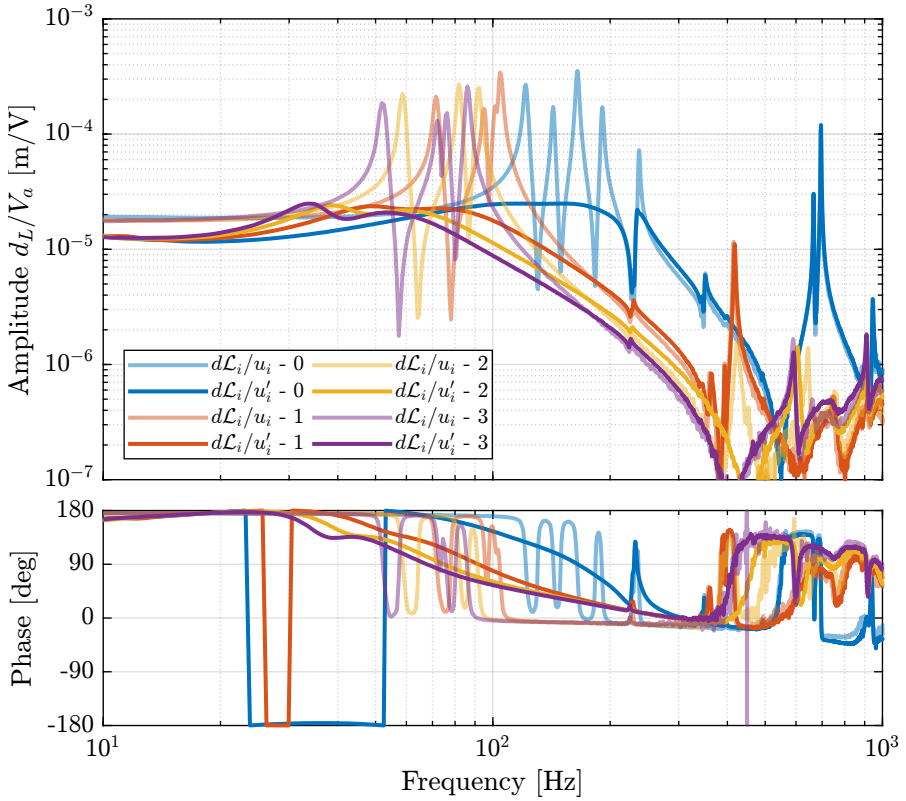

Figure 3.29: Damped and Undamped measured FRF (diagonal elements)

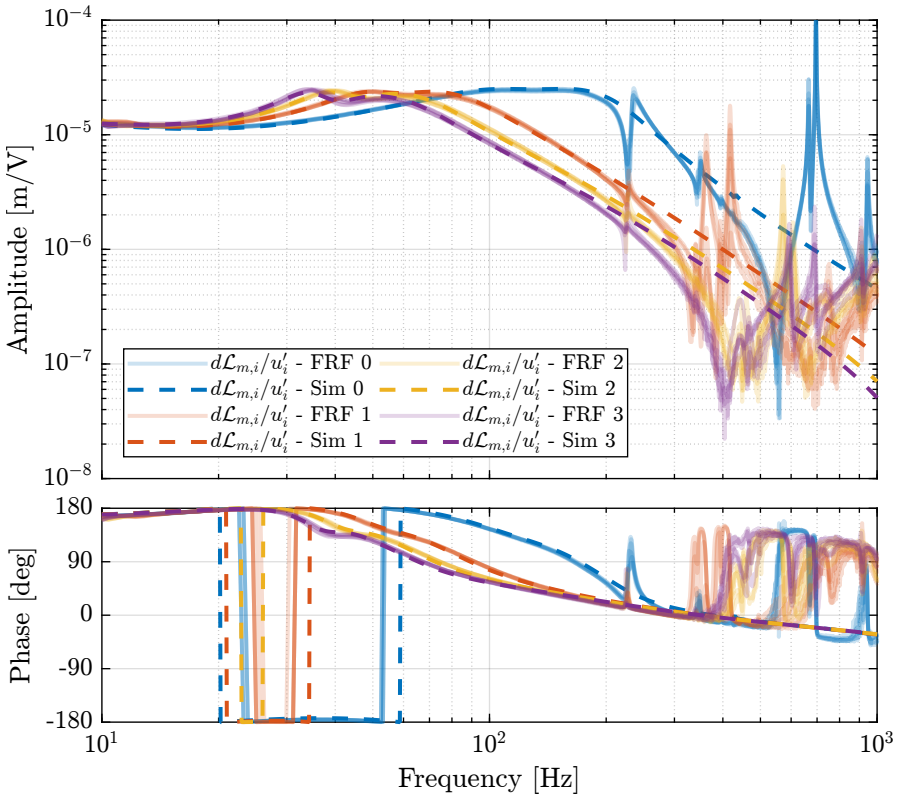

Figure 3.30: Comparison of the measured FRF and the identified dynamics from the Simscape model

using IFF.

Both are compared in Figure 3.31.

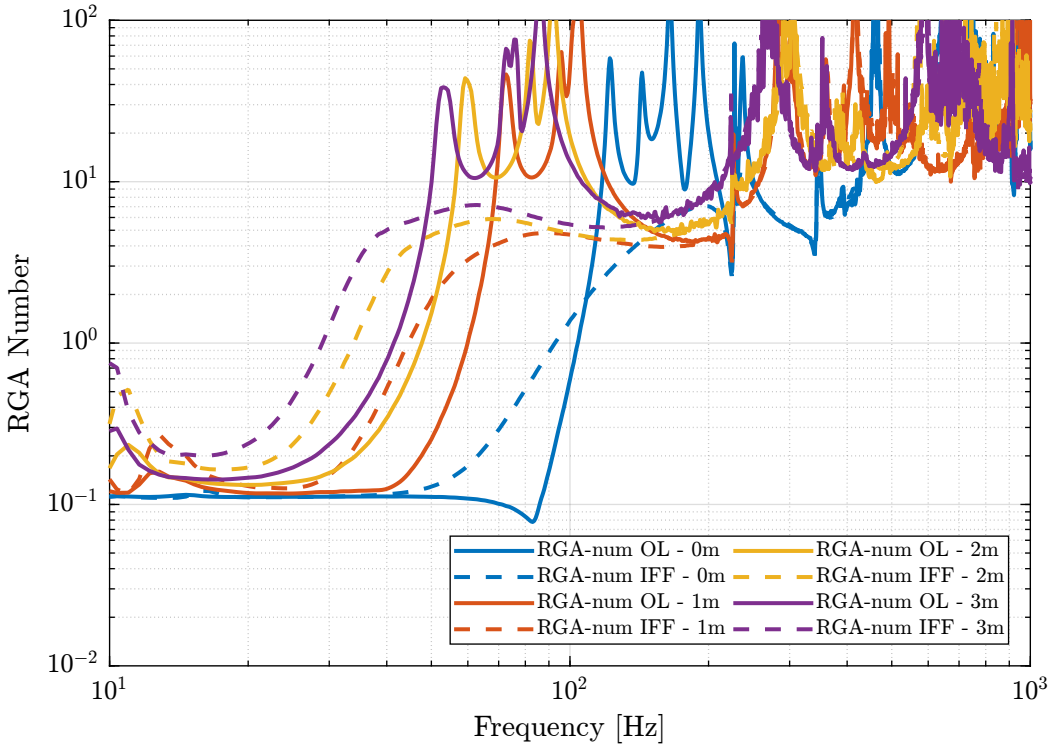

Figure 3.31: Comparison of the RGA-Number (interaction estimate) without and without IFF

Important

From Figure 3.32, it is clear that the interaction in the system is largest near the resonances. The Integral Force Feedback controller, by reducing the amplitude at the resonances, also reduces the coupling near these resonances. It however increases the coupling bellow the frequency of the suspension modes.

3.7 Un-Balanced mass

3.7.1 Introduction

In this section, we wish to see if a payload with a center of mass not aligned with the symmetry axis of the nano-hexapod could cause any issue.

To study that, the payload shown in Figure 3.32 is used.

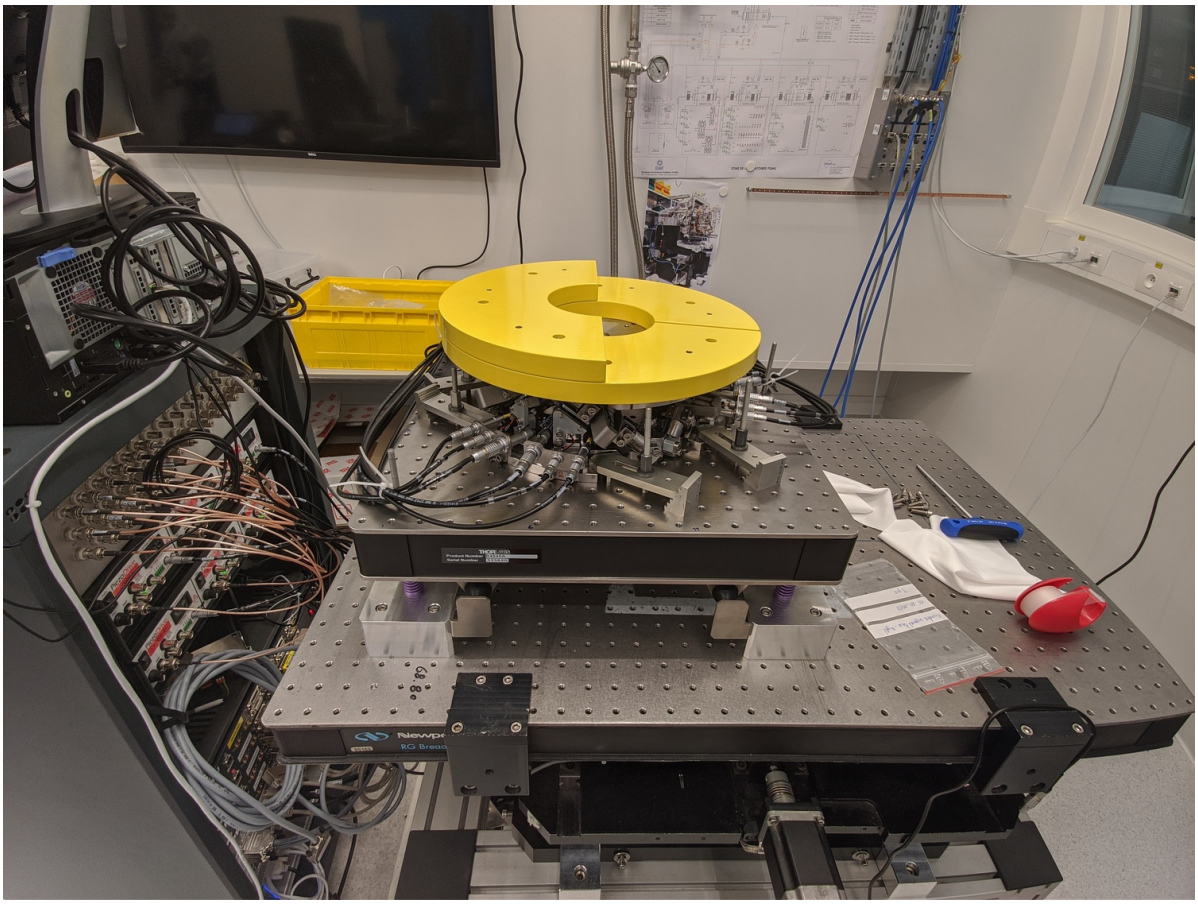

Figure 3.32: Nano-Hexapod with unbalanced payload

3.7.2 Compute the identified FRF with IFF

The following data are loaded:

- `Va`: the excitation voltage for the damped plant (corresponding to u_i')
- `de`: the measured motion by the 6 encoders (corresponding to $d\boldsymbol{\mathcal{L}}_m$)

The window `win` and the frequency vector `f` are defined. Finally the 6×6 transfer function matrix from $\boldsymbol{u}'$ to $d\boldsymbol{\mathcal{L}}_m$ is estimated: The identified dynamics are then saved for further use.

3.7.3 Effect of an unbalanced payload

The transfer functions from u_i to $d\mathcal{L}_i$ are shown in Figure 3.33. Due to the unbalanced payload, the system is not symmetrical anymore, and therefore each of the diagonal elements are not equal. This is due to the fact that each strut is not affected by the same inertia.

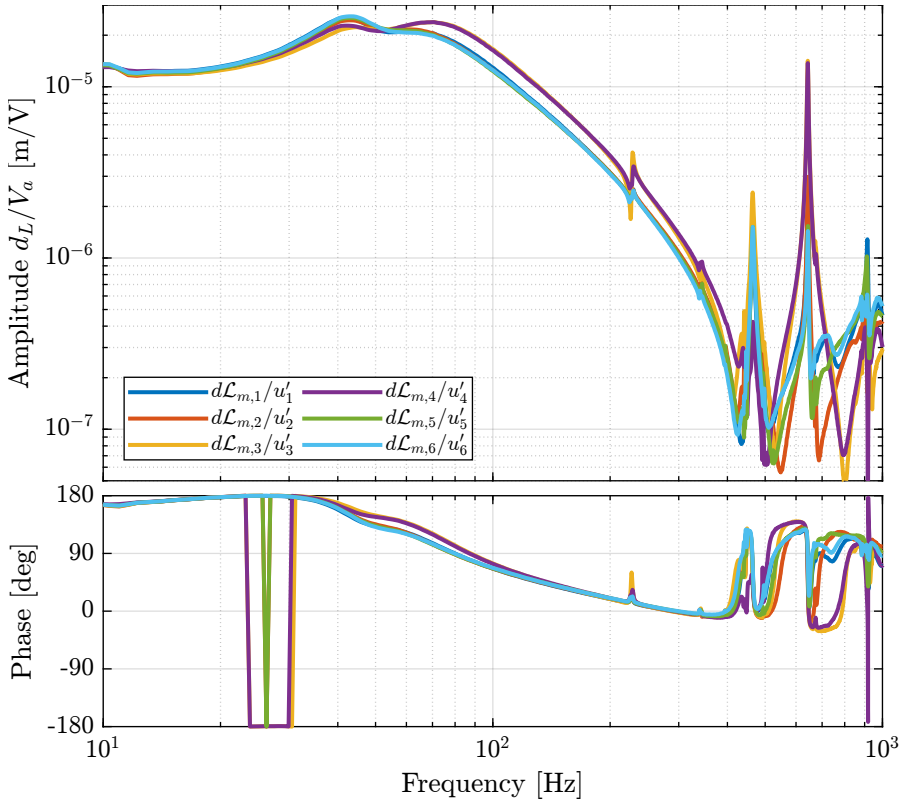

Figure 3.33: Transfer function from u_i to $d\mathcal{L}_i$ for the nano-hexapod with an unbalanced payload

3.8 Conclusion

Important

In this section, the dynamics of the nano-hexapod with the encoders fixed to the plates is studied. It has been found that:

- The measured dynamics is in agreement with the dynamics of the simscape model, up to the flexible modes of the top plate. See figures 3.5 and 3.6 for the transfer function to the force sensors and Figures 3.8 and 3.9 for the transfer functions to the encoders
- The Integral Force Feedback strategy is very effective in damping the suspension modes of the nano-hexapod (Figure 3.12).
- The transfer function from $\boldsymbol{u}'$ to $d\boldsymbol{\mathcal{L}}_m$ show nice dynamical properties and is a much better candidate for the high-authority-control than when the encoders were fixed to the struts. At least up to the flexible modes of the top plate, the diagonal elements of the transfer function matrix have alternating poles and zeros, and the phase is moving smoothly. Only the flexible modes of the top plates seems to be problematic for control.

4 Decentralized High Authority Control with Integral Force Feedback

In this section is studied the HAC-IFF architecture for the Nano-Hexapod. More precisely:

- The LAC control is a decentralized integral force feedback as studied in Section 3.3
- The HAC control is a decentralized controller working in the frame of the struts

The corresponding control architecture is shown in Figure 4.1 with:

- $\boldsymbol{r}_{\mathcal{X}_n}$: the 6×1 reference signal in the cartesian frame
- $\boldsymbol{r}_{d\mathcal{L}}$: the 6×1 reference signal transformed in the frame of the struts thanks to the inverse kinematic
- $\boldsymbol{\epsilon}_{d\mathcal{L}}$: the 6×1 length error of the 6 struts
- $\boldsymbol{u}'$: input of the damped plant
- $\boldsymbol{u}$: generated DAC voltages
- $\boldsymbol{\tau}_m$: measured force sensors
- $d\boldsymbol{\mathcal{L}}_m$: measured displacement of the struts by the encoders

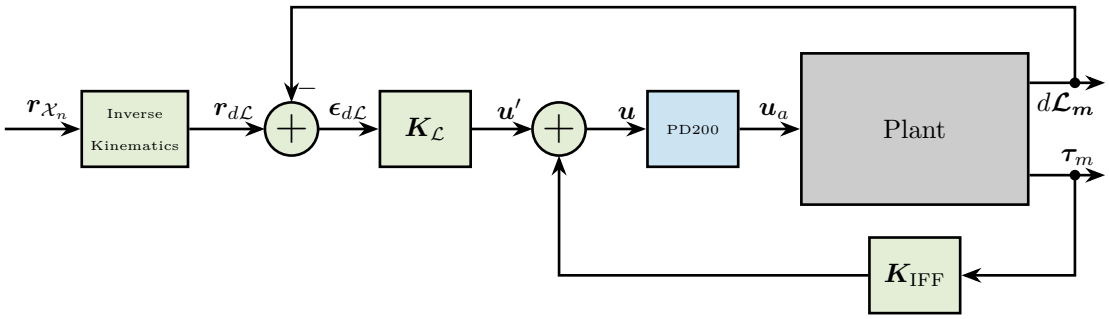

Figure 4.1: HAC-LAC: IFF + Control in the frame of the legs

This part is structured as follow:

- Section 4.1: some reference tracking tests are performed
- Section 4.2: the decentralized high authority controller is tuned using the Simscape model and is implemented and tested experimentally

- Section 4.3: an interaction analysis is performed, from which the best decoupling strategy can be determined
- Section 4.4: Robust High Authority Controller are designed

4.1 Reference Tracking - Trajectories

In this section, several trajectories representing the wanted pose (position and orientation) of the top platform with respect to the bottom platform are defined.

These trajectories will be used to test the HAC-LAC architecture.

In order to transform the wanted pose to the wanted displacement of the 6 struts, the inverse kinematic is required. As a first approximation, the Jacobian matrix $\boldsymbol{J}$ can be used instead of using the full inverse kinematic equations.

Therefore, the control architecture with the input trajectory $\boldsymbol{r}_{\mathcal{X}_n}$ is shown in Figure 4.2.

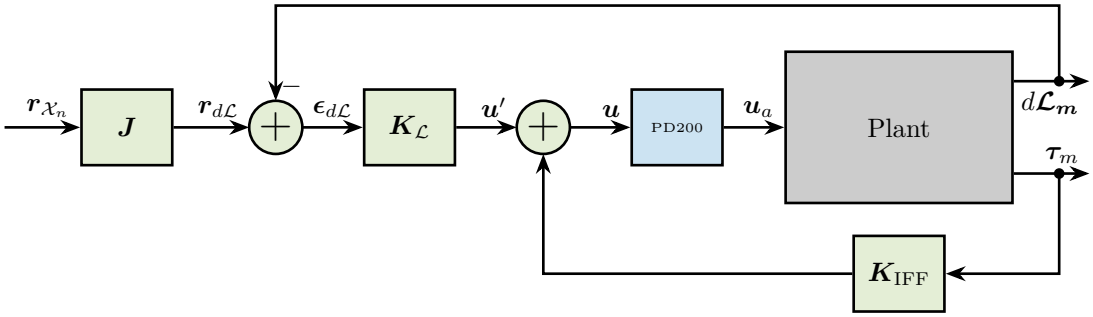

Figure 4.2: HAC-LAC: IFF + Control in the frame of the legs

In the following sections, several reference trajectories are defined:

- Section 4.1.1: simple scans in the Y-Z plane
- Section 4.1.2: scans in tilt are performed
- Section 4.1.3: scans with X-Y-Z translations in order to draw the word "NASS"

4.1.1 Y-Z Scans

A function `generateYZScanTrajectory` has been developed in order to easily generate scans in the Y-Z plane.

For instance, the following generated trajectory is represented in Figure 4.3.

The Y and Z positions as a function of time are shown in Figure 4.4.

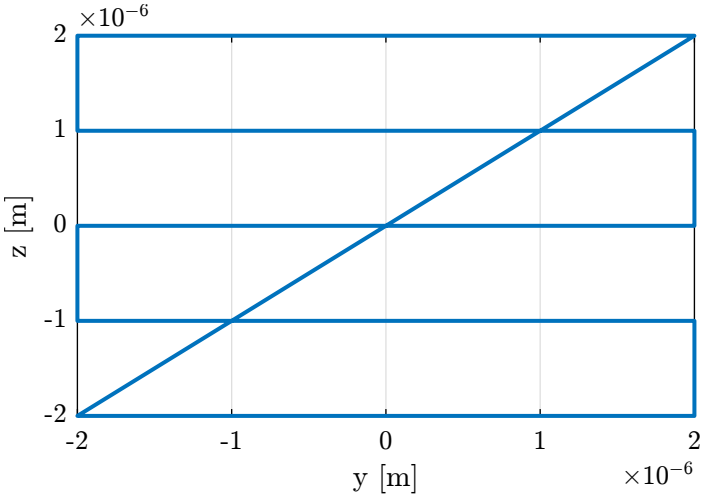

Figure 4.3: Generated scan in the Y-Z plane

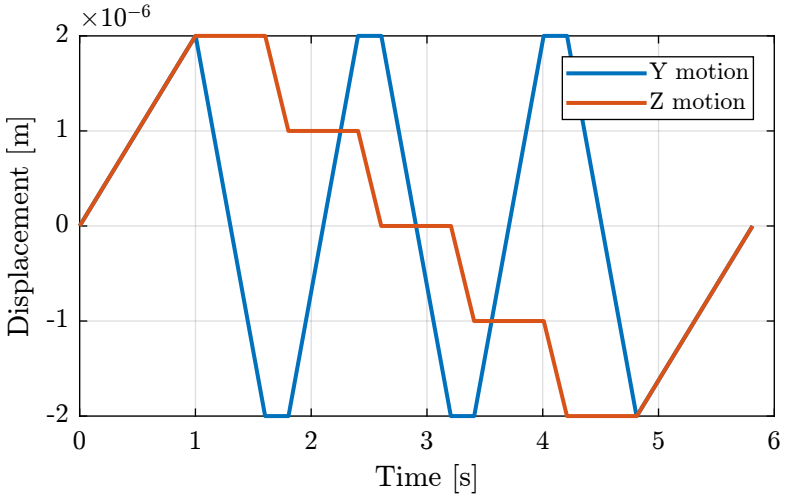

Figure 4.4: Y and Z trajectories as a function of time

Using the Jacobian matrix, it is possible to compute the wanted struts lengths as a function of time:

$$\boldsymbol{r}_{d\mathcal{L}} = \boldsymbol{J}\boldsymbol{r}_{\mathcal{X}_n} \tag{4.1}$$

The reference signal for the strut length is shown in Figure 4.5.

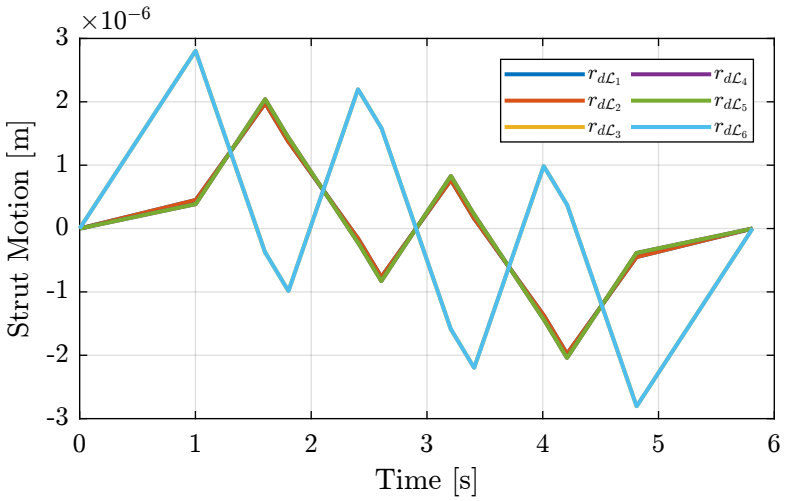

Figure 4.5: Trajectories for the 6 individual struts

4.1.2 Tilt Scans

A function `generalSpiralAngleTrajectory` has been developed in order to easily generate R_x, R_y tilt scans.

For instance, the following generated trajectory is represented in Figure 4.6.

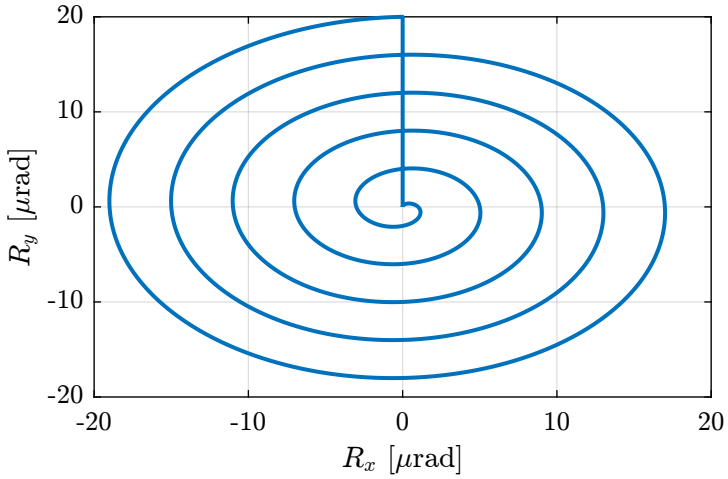

Figure 4.6: Generated "spiral" scan

The reference signal for the strut length is shown in Figure 4.7.

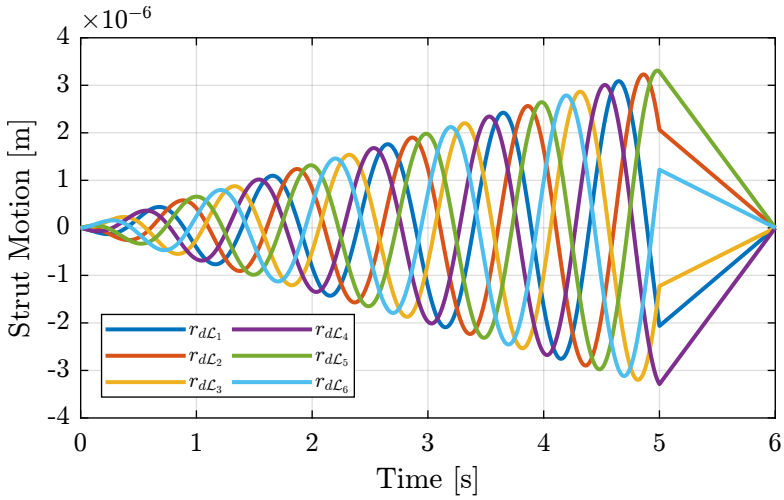

Figure 4.7: Trajectories for the 6 individual struts - Tilt scan

4.1.3 "NASS" reference path

In this section, a reference path that "draws" the work "NASS" is developed.

First, a series of points representing each letter are defined. Between each letter, a negative Z motion is performed. Then, using the `generateXYZTrajectory` function, the 6×1 trajectory signal is computed. The trajectory in the X-Y plane is shown in Figure 4.8 (the transitions between the letters are removed).

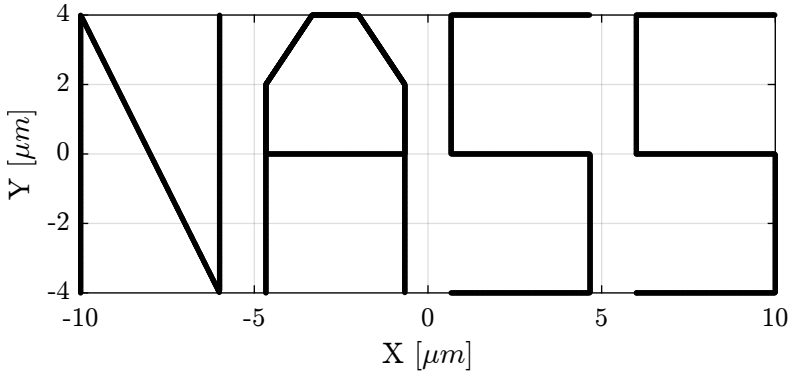

Figure 4.8: Reference path corresponding to the "NASS" acronym

It can also be better viewed in a 3D representation as in Figure 4.9.

4.2 First Basic High Authority Controller

In this section, a simple decentralized high authority controller $\boldsymbol{K}_{\mathcal{L}}$ is developed to work without any payload.

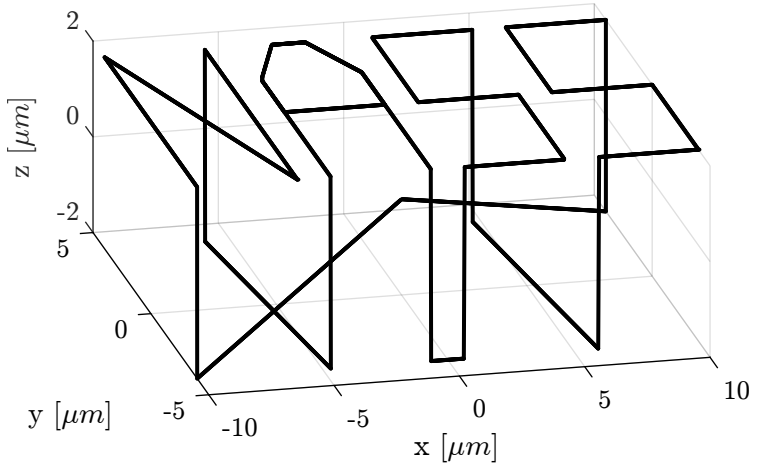

Figure 4.9: Reference path that draws "NASS" - 3D view

The diagonal controller is tuned using classical Loop Shaping in Section 4.2.1. The stability is verified in Section 4.2.2 using the Simscape model.

4.2.1 HAC Controller

Let's first try to design a first decentralized controller with:

- a bandwidth of 100Hz
- sufficient phase margin
- simple and understandable components

After some very basic and manual loop shaping, A diagonal controller is developed. Each diagonal terms are identical and are composed of:

- A lead around 100Hz
- A first order low pass filter starting at 200Hz to add some robustness to high frequency modes
- A notch at 700Hz to cancel the flexible modes of the top plate
- A pure integrator

This controller is saved for further use. The experimental loop gain is computed and shown in Figure 4.10.

4.2.2 Verification of the Stability using the Simscape model

The HAC-IFF control strategy is implemented using Simscape. We identify the closed-loop system. And verify that it is indeed stable.

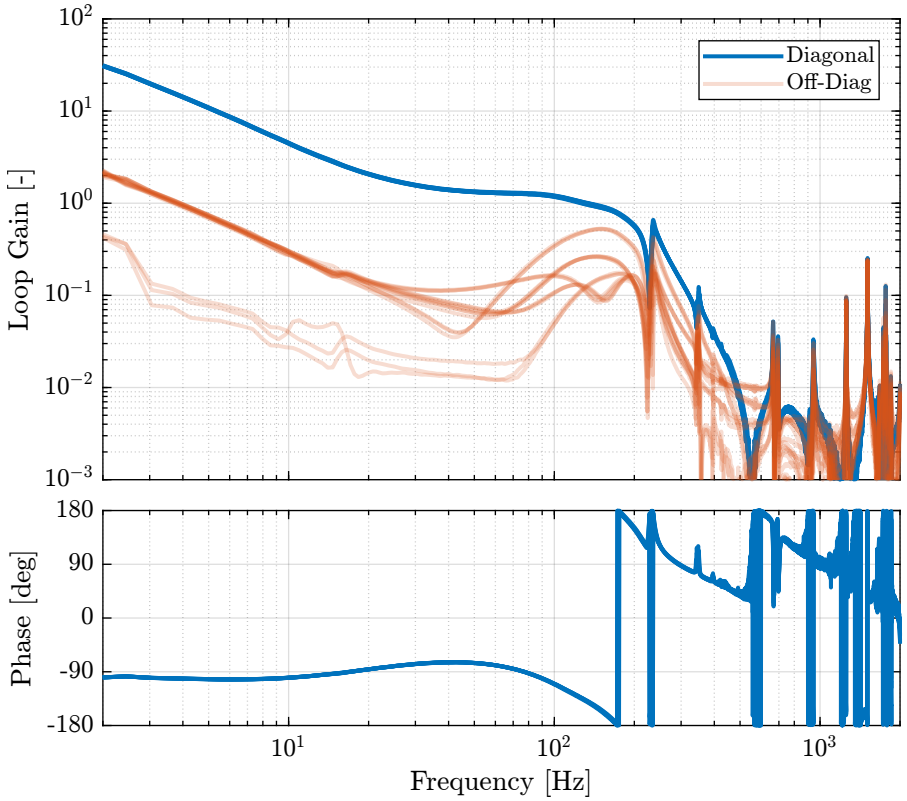

Figure 4.10: Diagonal and off-diagonal elements of the Loop gain for "HAC-IFF-Struts"

Matlab

```
%% Verify the stability
isstable(Gd_iff_hac_opt)
```

Results

```
1
```

4.2.3 Experimental Validation

Both the Integral Force Feedback controller (developed in Section 3.3) and the high authority controller working in the frame of the struts (developed in Section 4.2) are implemented experimentally.

Two reference tracking experiments are performed to evaluate the stability and performances of the implemented control.

The position of the top-platform is estimated using the Jacobian matrix: The reference path as well as the measured position are partially shown in the Y-Z plane in Figure 4.11.

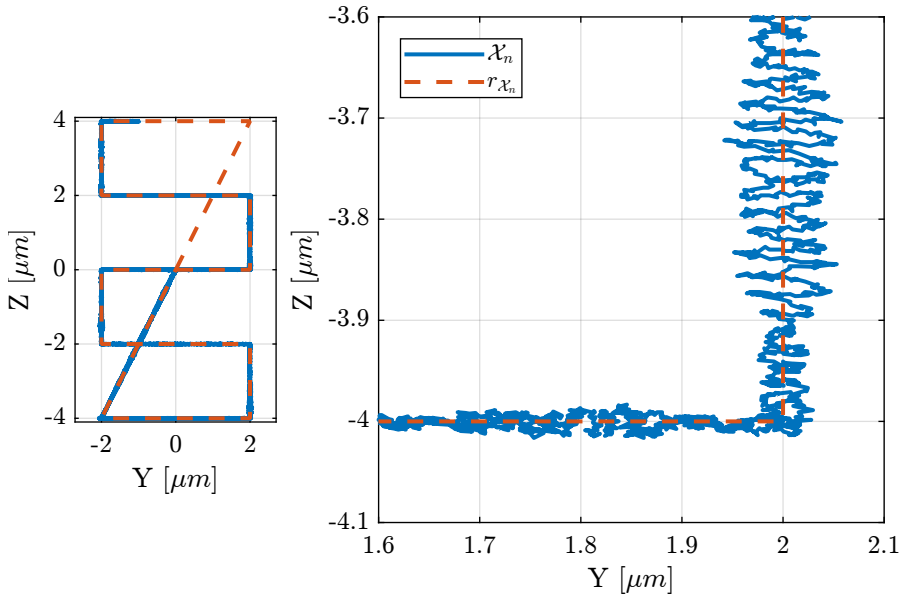

Figure 4.11: Measured position $\boldsymbol{\mathcal{X}}_n$ and reference signal $\boldsymbol{r}_{\mathcal{X}_n}$ in the Y-Z plane - Zoom on a change of direction

Important

It is clear from Figure 4.11 that the position of the nano-hexapod effectively tracks to reference signal. However, oscillations with amplitudes as large as 50nm can be observe.
It turns out that the frequency of these oscillations is 100Hz which is corresponding to the crossover frequency of the High Authority Control loop. This clearly indicates poor stability margins. In the next section, the controller is re-designed to improve the stability margins.

4.2.4 Controller with increased stability margins

The High Authority Controller is re-designed in order to improve the stability margins. The bode plot of the new loop gain is shown in Figure 4.12.

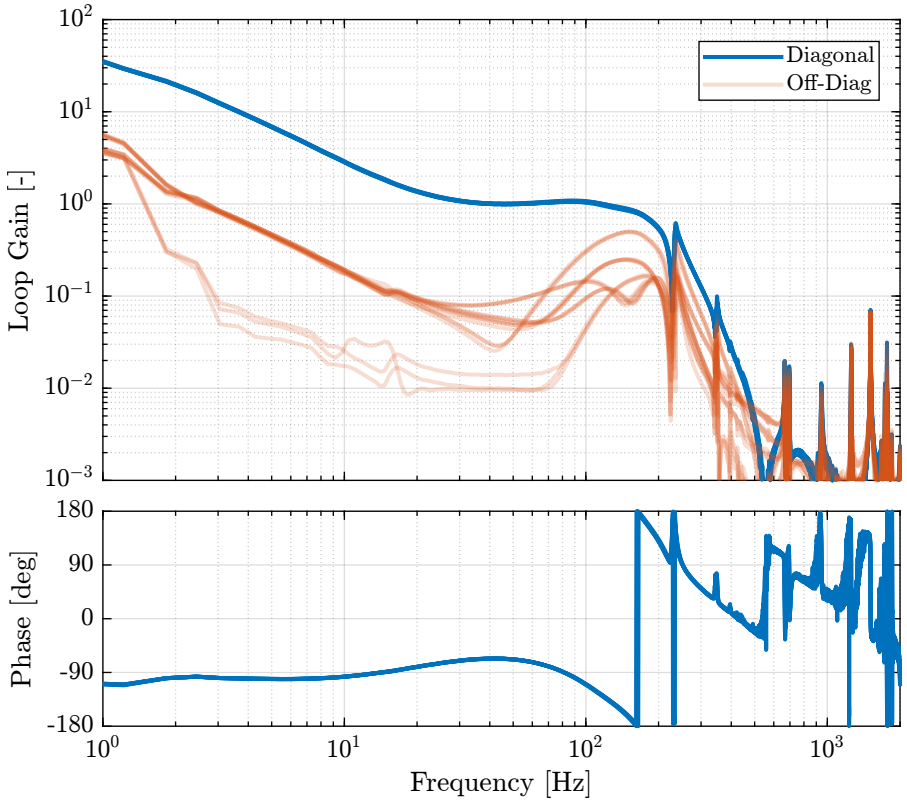

Figure 4.12: Loop Gain for the updated decentralized HAC controller

This new controller is implemented experimentally and several tracking tests are performed. The pose of the top platform is estimated from the encoder position using the Jacobian matrix. The measured motion as well as the trajectory are shown in Figure 4.13.

The trajectory and measured motion are also shown in the X-Y plane in Figure 4.14.

The orientation errors during all the scans are shown in Figure 4.15.

Important

Using the updated High Authority Controller, the nano-hexapod can follow trajectories with high accuracy (the position errors are in the order of 50nm peak to peak, and the orientation errors 300nrad peak to peak).

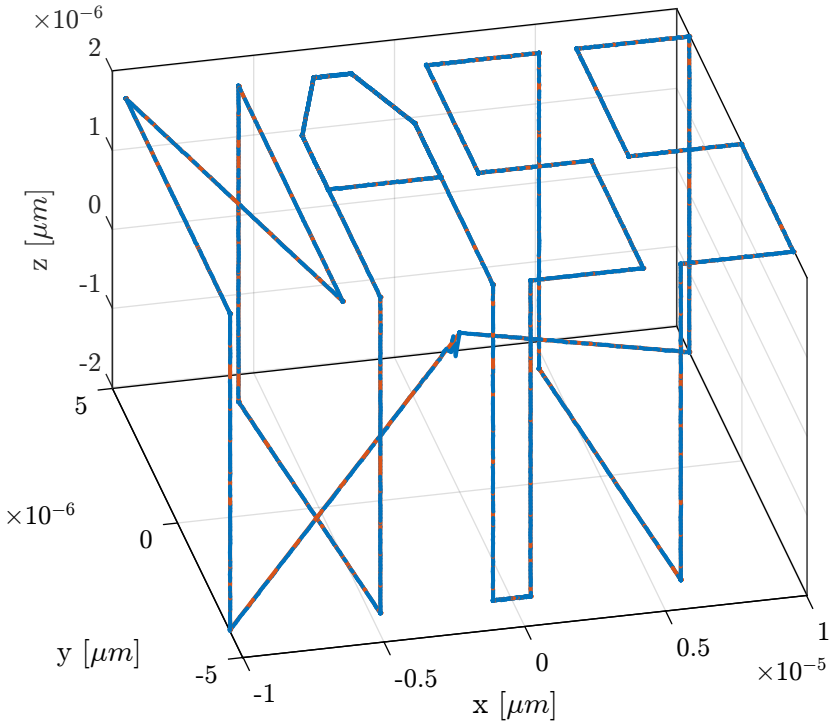

Figure 4.13: Measured position $\boldsymbol{\mathcal{X}}_n$ and reference signal $\boldsymbol{r}_{\mathcal{X}_n}$ for the "NASS" trajectory

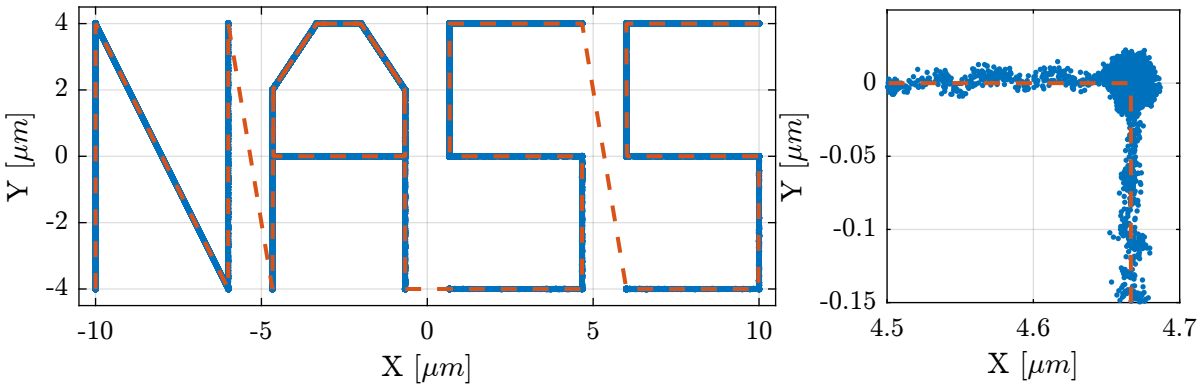

Figure 4.14: Reference path and measured motion in the X-Y plane

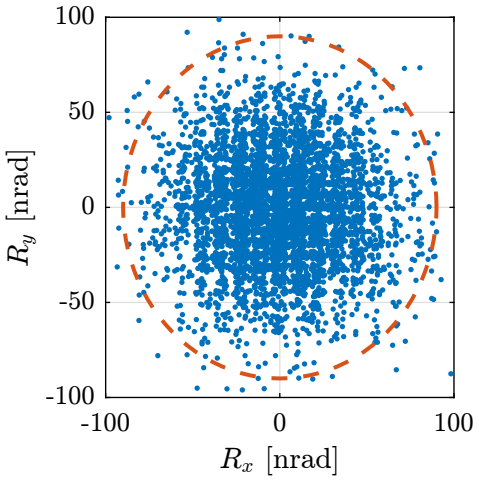

Figure 4.15: Orientation errors during the scan

4.3 Interaction Analysis and Decoupling

In this section, the interaction in the identified plant is estimated using the Relative Gain Array (RGA) [1, Chap. 3.4].

Then, several decoupling strategies are compared for the nano-hexapod.

The RGA Matrix is defined as follow:

$$\text{RGA}(G(f)) = G(f) \times (G(f)^{-1})^T \tag{4.2}$$

Then, the RGA number is defined:

$$\text{RGA-num}(f) = \|\text{I - RGA(G(f))}\|_{\text{sum}} \tag{4.3}$$

In this section, the plant with 2 added mass is studied.

4.3.1 Parameters

4.3.2 No Decoupling (Decentralized)

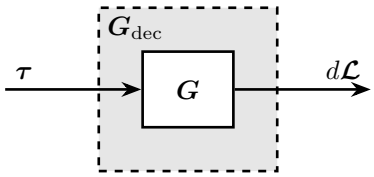

Figure 4.16: Block diagram representing the plant.

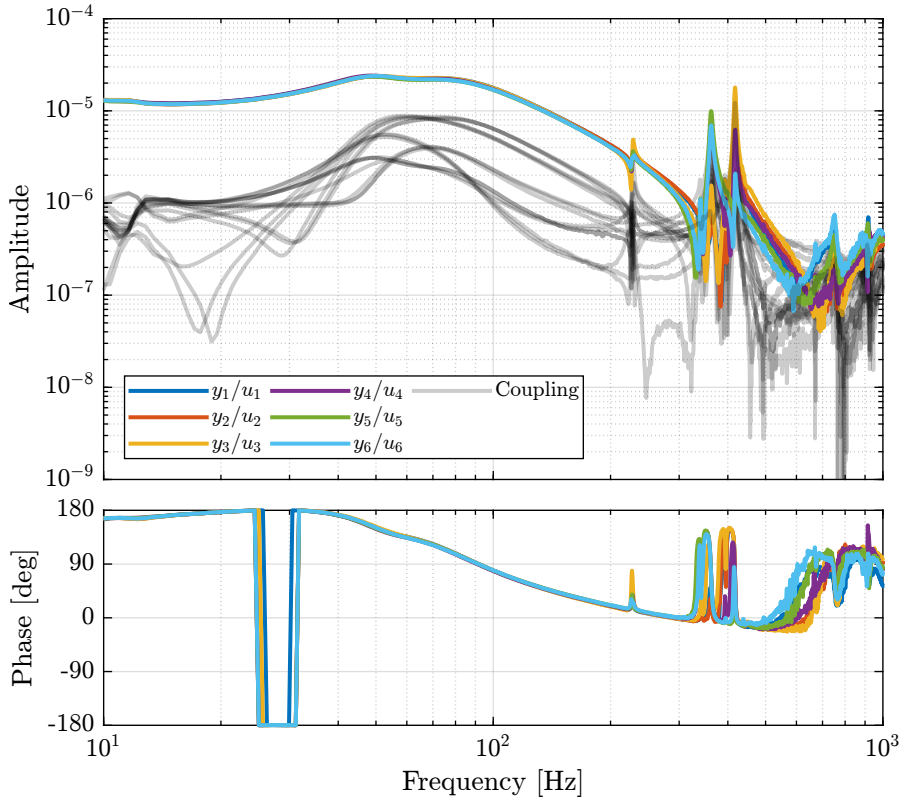

Figure 4.17: Bode Plot of the decentralized plant (diagonal and off-diagonal terms)

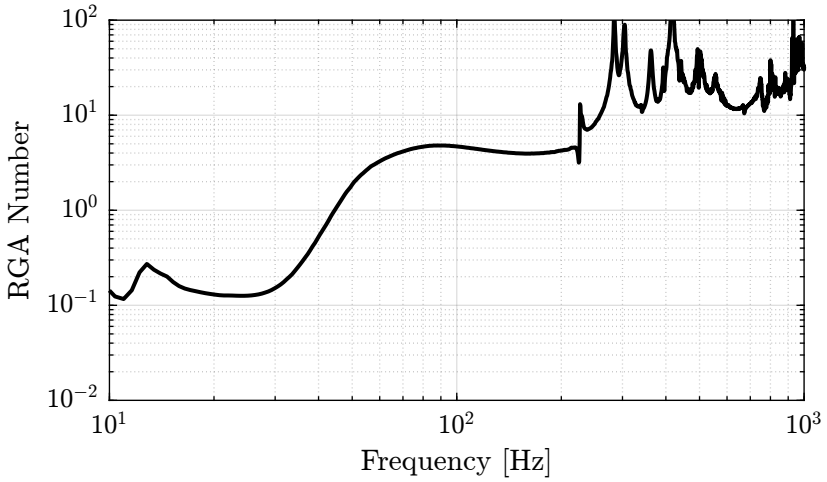

Figure 4.18: RGA number for the decentralized plant

4.3.3 Static Decoupling

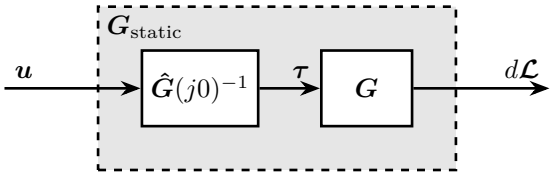

Figure 4.19: Decoupling using the inverse of the DC gain of the plant

The DC gain is evaluated from the model as be have bad low frequency identification.

-62011.5	3910.6	4299.3	660.7	-4016.5	-4373.6
3914.4	-61991.2	-4356.8	-4019.2	640.2	4281.6
-4020.0	-4370.5	-62004.5	3914.6	4295.8	653.8
660.9	4292.4	3903.3	-62012.2	-4366.5	-4008.9
4302.8	655.6	-4025.8	-4377.8	-62006.0	3919.7
-4377.9	-4013.2	668.6	4303.7	3906.8	-62019.3

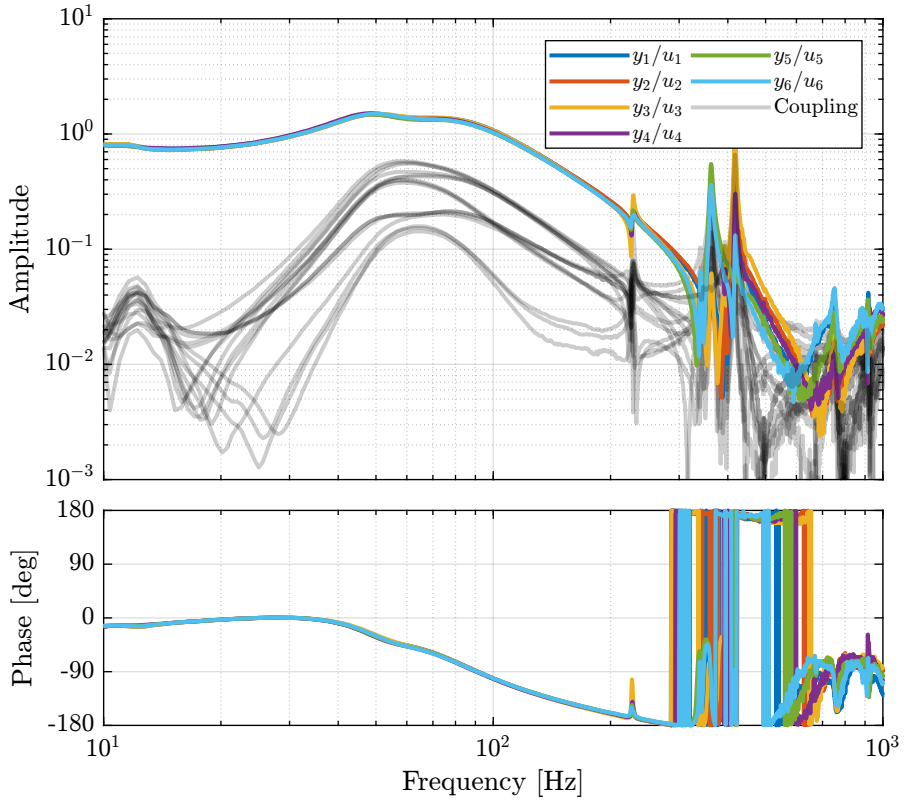

Figure 4.20: Bode Plot of the static decoupled plant

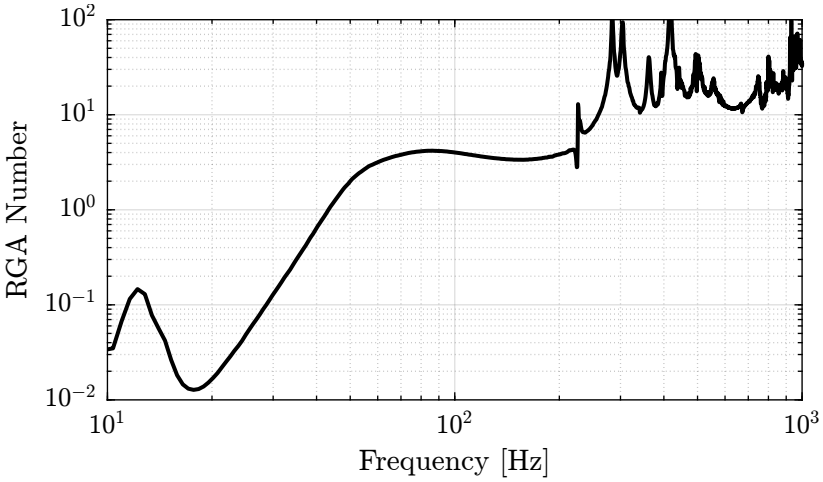

Figure 4.21: RGA number for the statically decoupled plant

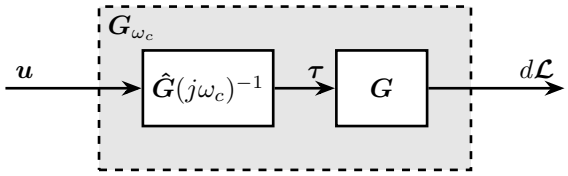

Figure 4.22: Decoupling using the inverse of a dynamical model $\hat{\boldsymbol{G}}$ of the plant dynamics $\boldsymbol{G}$

4.3.4 Decoupling at the Crossover

67229.8	3769.3	-13704.6	-23084.8	-6318.2	23378.7
3486.2	67708.9	23220.0	-6314.5	-22699.8	-14060.6
-5731.7	22471.7	66701.4	3070.2	-13205.6	-21944.6
-23305.5	-14542.6	2743.2	70097.6	24846.8	-5295.0
-14882.9	-22957.8	-5344.4	25786.2	70484.6	2979.9
24353.3	-5195.2	-22449.0	-14459.2	2203.6	69484.2

4.3.5 SVD Decoupling

4.3.6 Dynamic decoupling

4.3.7 Jacobian Decoupling - Center of Stiffness

The obtained plant is shown in Figure 4.32. We can see that the stiffness in the x, y and z directions are equal, which is due to the cubic architecture of the Stewart platform.

Because the plant in translation and rotation has very different gains, we choose to normalize the plant inputs such that the gain of the diagonal term is equal to 1 at 100Hz.

The results is shown in Figure 4.33.

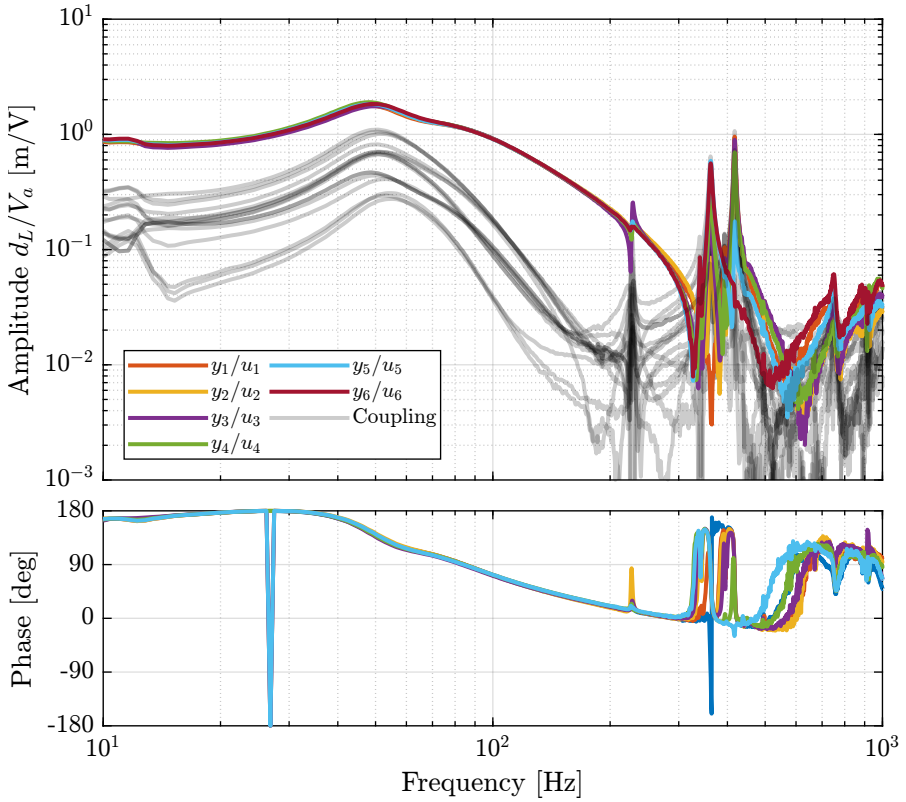

Figure 4.23: Bode Plot of the plant decoupled at the crossover

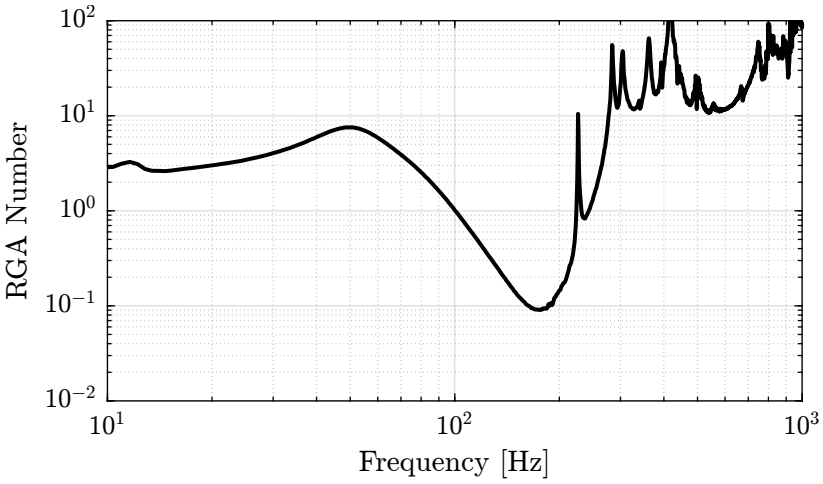

Figure 4.24: RGA number for the plant decoupled at the crossover

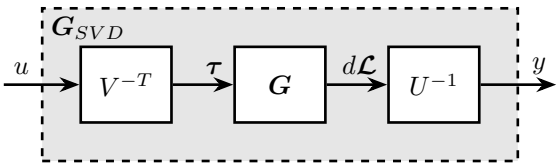

Figure 4.25: Decoupling using the Singular Value Decomposition

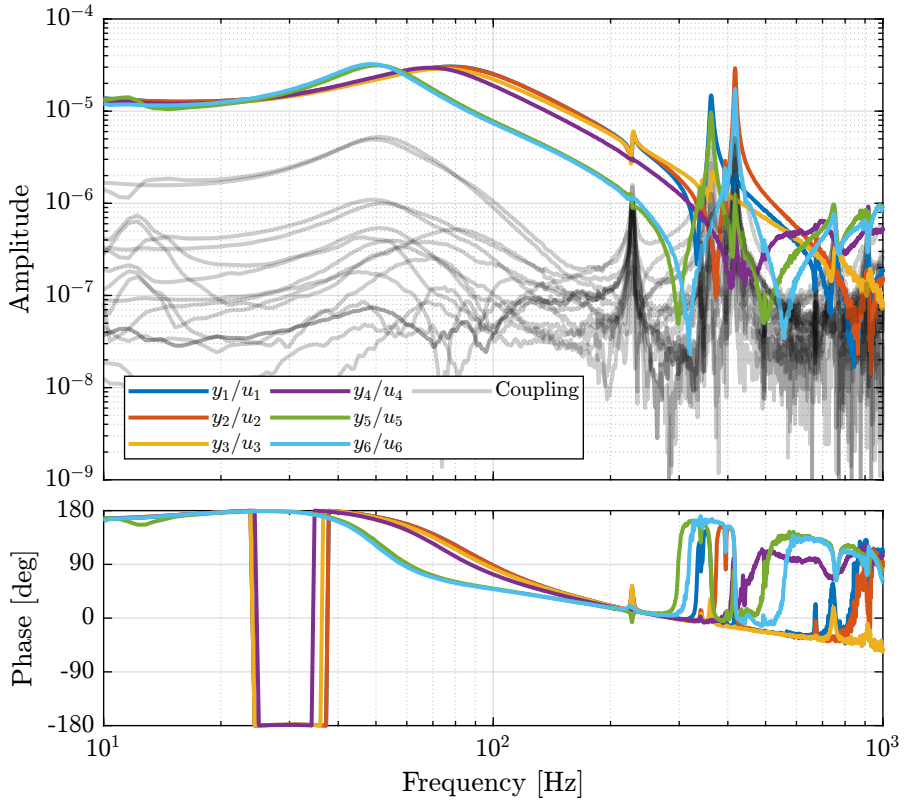

Figure 4.26: Bode Plot of the plant decoupled using the Singular Value Decomposition

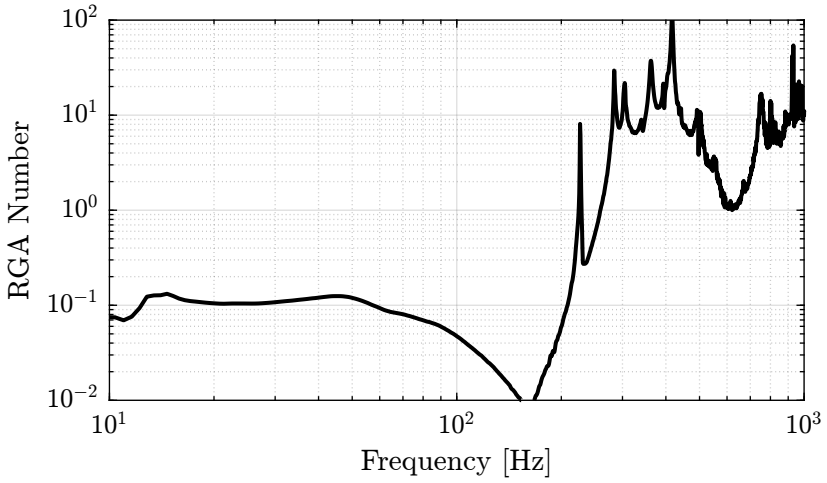

Figure 4.27: RGA number for the plant decoupled using the SVD

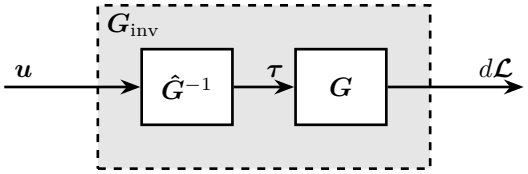

Figure 4.28: Decoupling using the inverse of a dynamical model $\hat{G}$ of the plant dynamics G

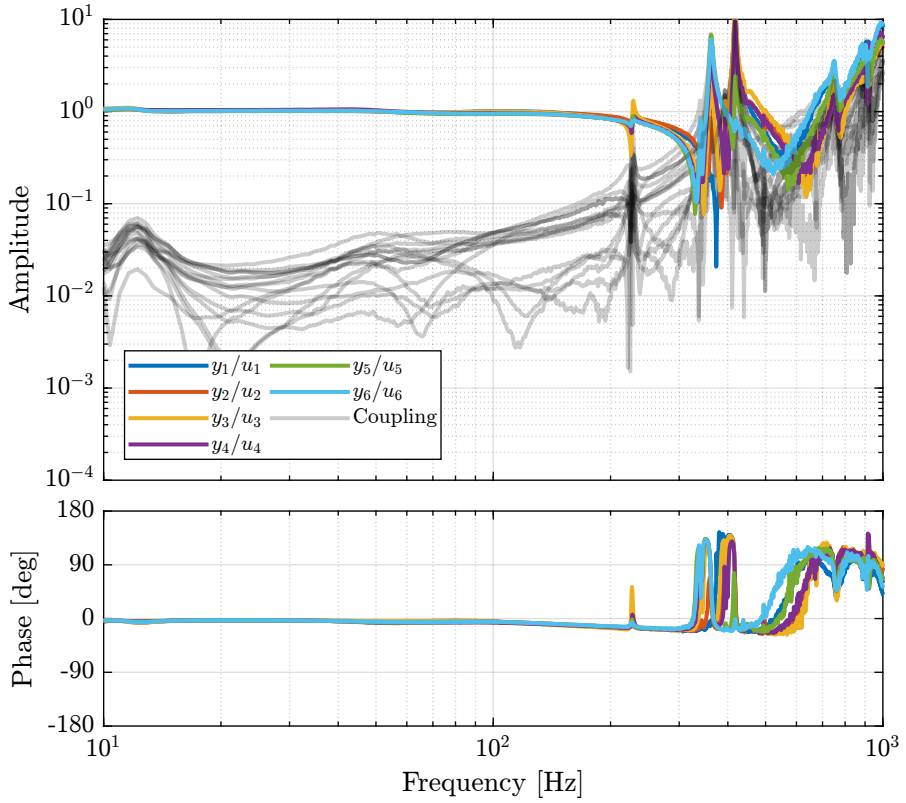

Figure 4.29: Bode Plot of the dynamically decoupled plant

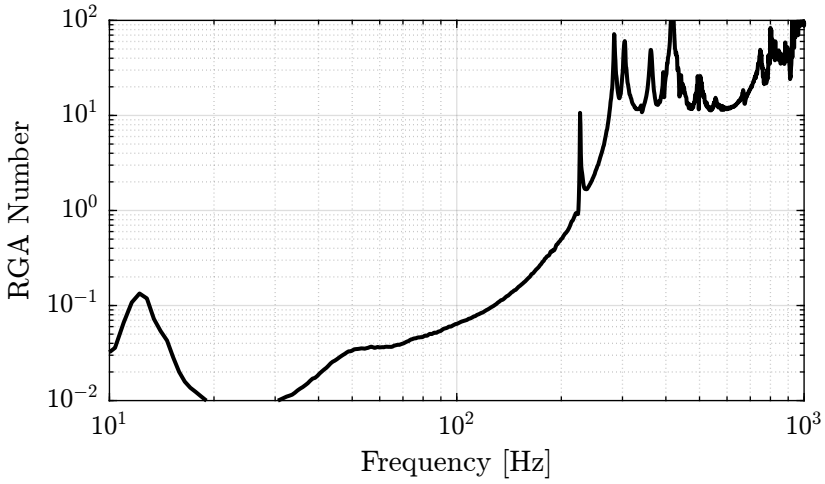

Figure 4.30: RGA number for the dynamically decoupled plant

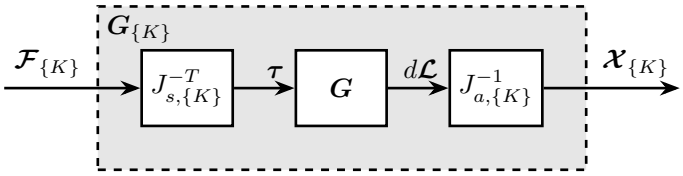

Figure 4.31: Decoupling using Jacobian matrices evaluated at the Center of Stiffness

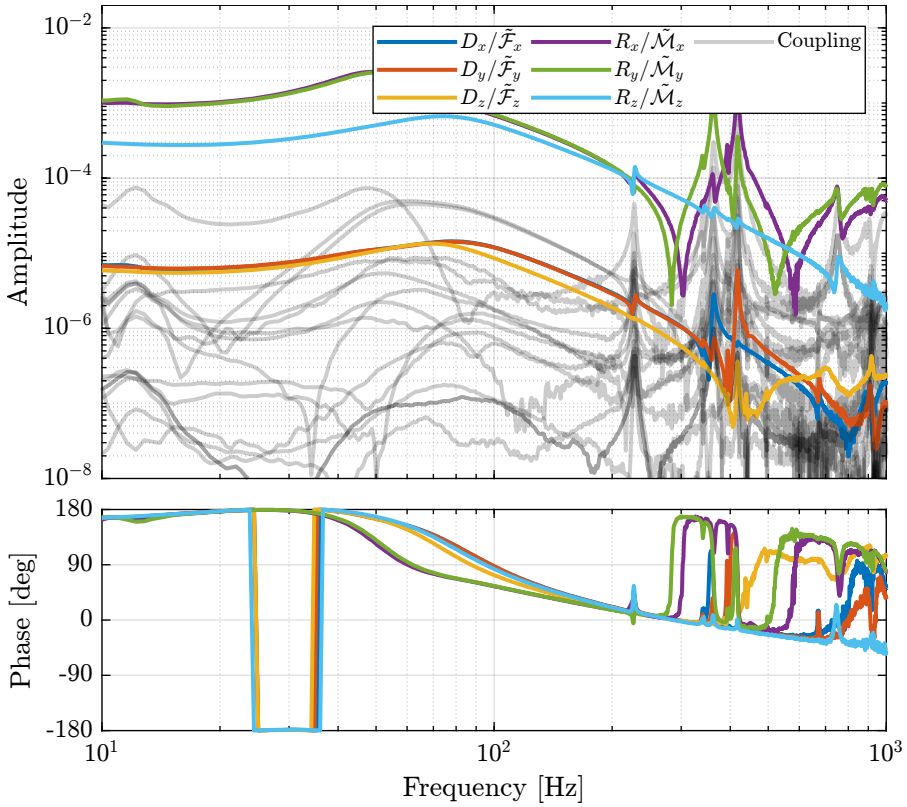

Figure 4.32: Bode Plot of the plant decoupled using the Jacobian evaluated at the "center of stiffness"

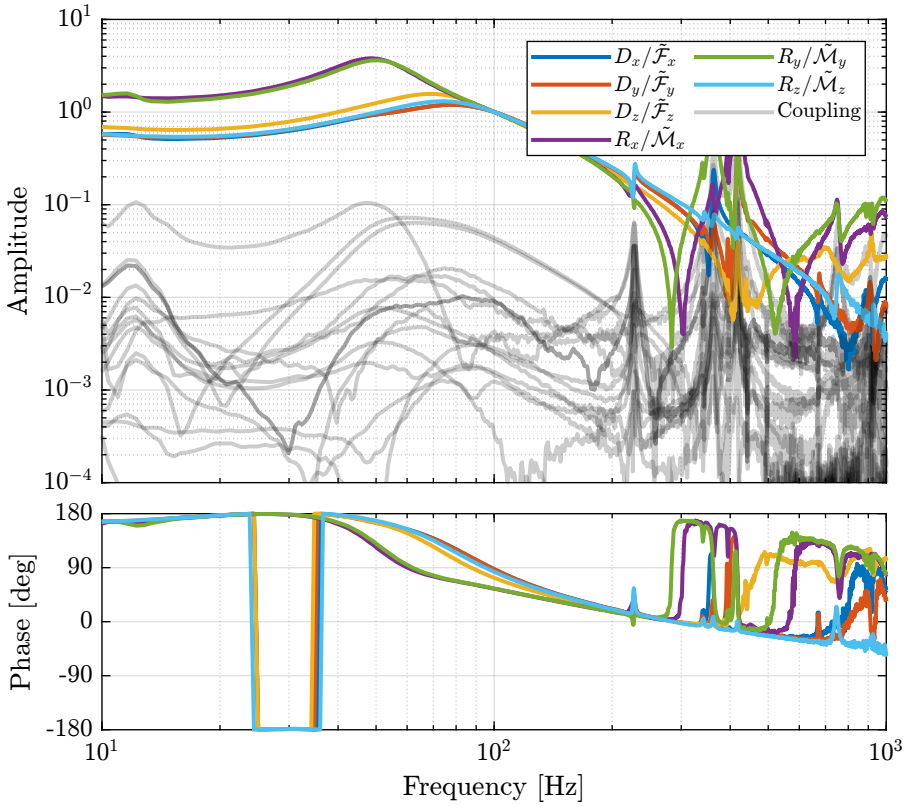

Figure 4.33: Bode Plot of the plant decoupled using the Jacobian evaluated at the "center of stiffness"

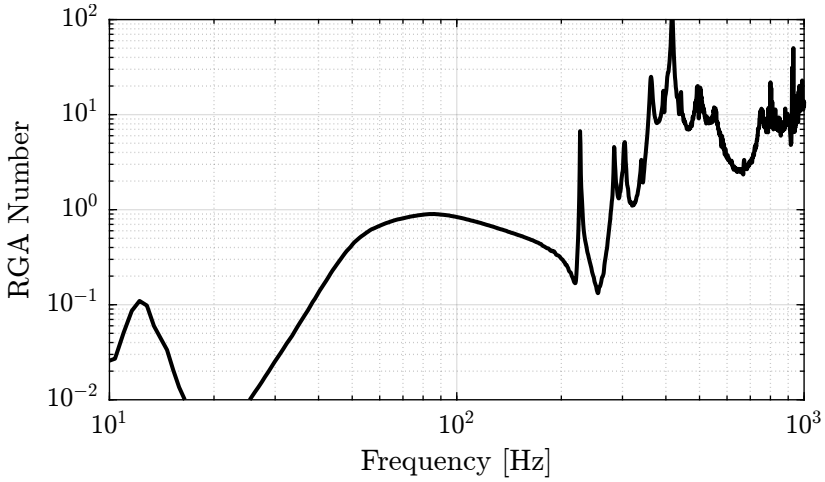

Figure 4.34: RGA number for the plant decoupled using the Jacobian evaluted at the Center of Stiffness

4.3.8 Jacobian Decoupling - Center of Mass

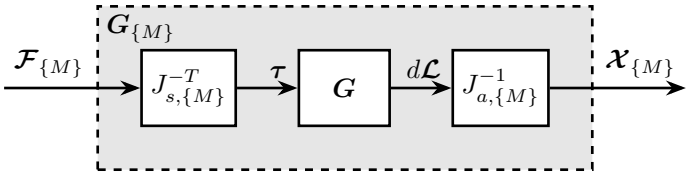

Figure 4.35: Decoupling using Jacobian matrices evaluated at the Center of Mass

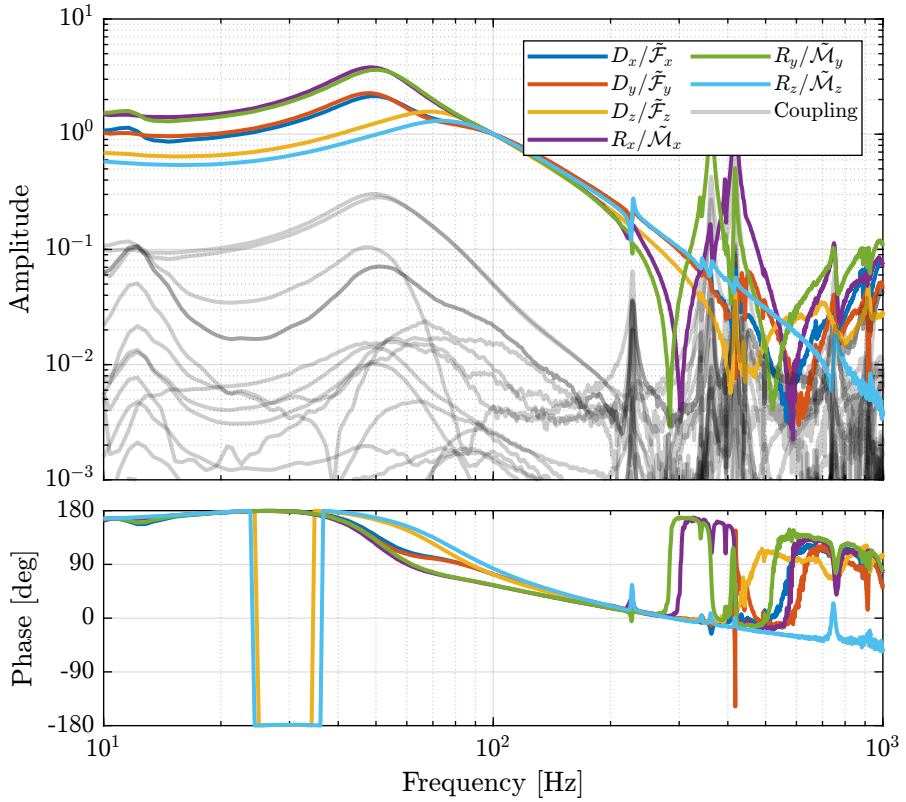

Figure 4.36: Bode Plot of the plant decoupled using the Jacobian evaluated at the Center of Mass

4.3.9 Decoupling Comparison

Let's now compare all of the decoupling methods (Figure 4.38).

Important

From Figure 4.38, the following remarks are made:

- **Decentralized plant**: well decoupled below suspension modes
- **Static inversion**: similar to the decentralized plant as the decentralized plant has already a good decoupling at low frequency
- **Crossover inversion**: the decoupling is improved around the crossover frequency as com-

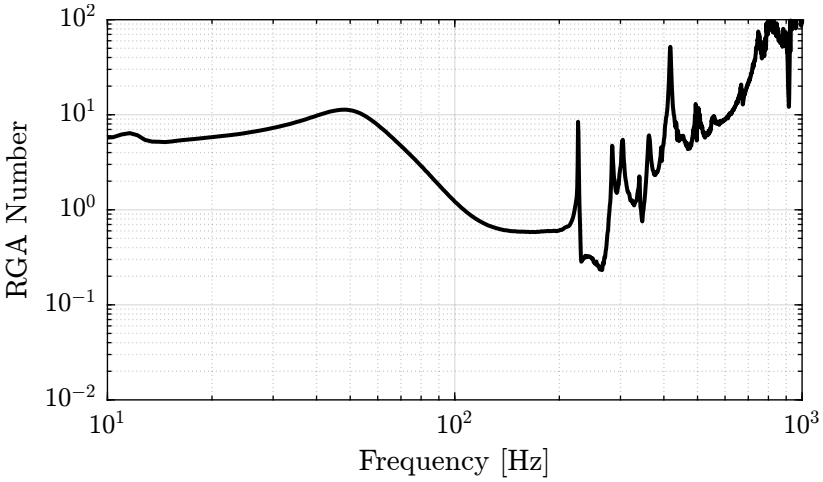

Figure 4.37: RGA number for the plant decoupled using the Jacobian evaluted at the Center of Mass

pared to the decentralized plant. However, the decoupling is increased at lower frequency.

- **SVD decoupling**: Very good decoupling up to 235Hz. Especially between 100Hz and 200Hz.
- **Dynamic Inversion**: the plant is very well decoupled at frequencies where the model is accurate (below 235Hz where flexible modes are not modelled).
- **Jacobian - Stiffness**: good decoupling at low frequency. The decoupling increases at the frequency of the suspension modes, but is acceptable up to the strut flexible modes (235Hz).
- **Jacobian - Mass**: bad decoupling at low frequency. Better decoupling above the frequency of the suspension modes, and acceptable decoupling up to the strut flexible modes (235Hz).

4.3.10 Decoupling Robustness

Let's now see how the decoupling is changing when changing the payload's mass. The obtained RGA-numbers are shown in Figure 4.39.

Important

From Figure 4.39:

- The decoupling using the Jacobian evaluated at the "center of stiffness" seems to give the most robust results.

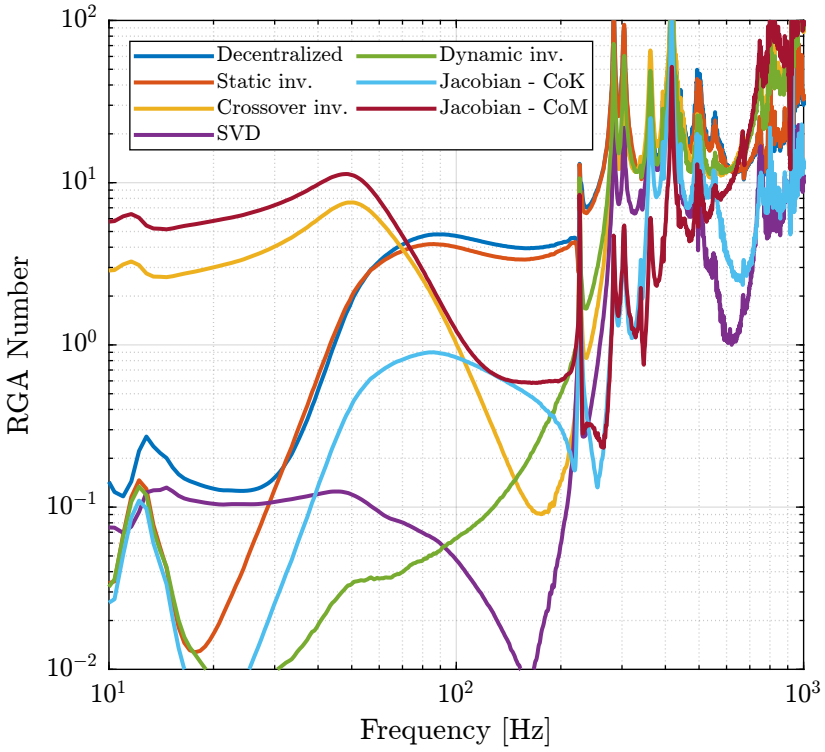

Figure 4.38: Comparison of the obtained RGA-numbers for all the decoupling methods

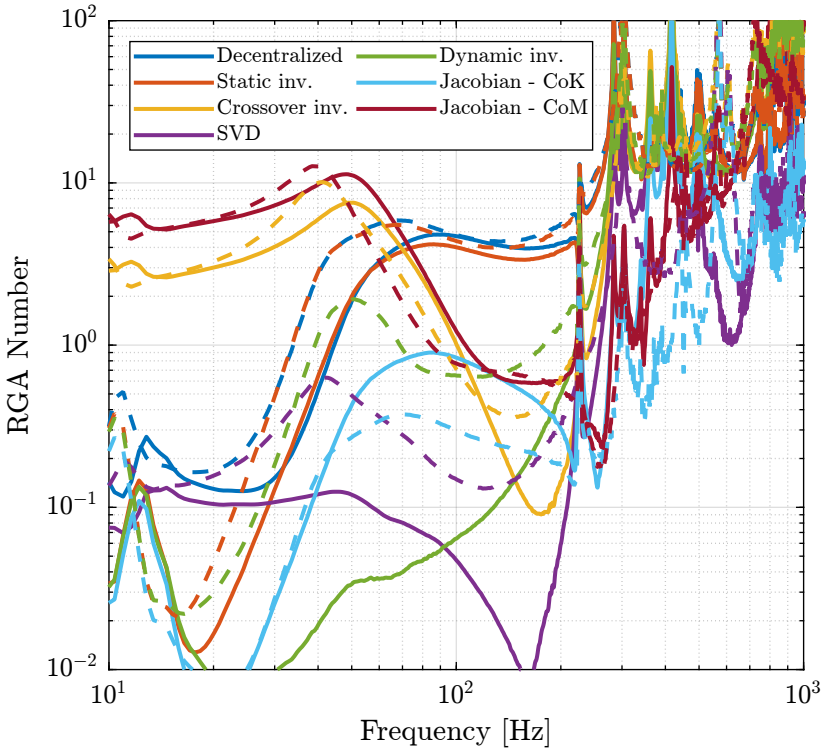

Figure 4.39: Change of the RGA-number with a change of the payload. Indication of the robustness of the inversion method.

4.3.11 Conclusion

Important

Several decoupling methods can be used:

- SVD
- Inverse
- Jacobian (CoK)

Table 4.1: Summary of the interaction analysis and different decoupling strategies

Method	RGA	Diag Plant	Robustness
Decentralized	–	Equal	++
Static dec.	–	Equal	++
Crossover dec.	-	Equal	0
SVD	++	Diff	+
Dynamic dec.	++	Unity, equal	-
Jacobian - CoK	+	Diff	++
Jacobian - CoM	0	Diff	+

4.4 Robust High Authority Controller

In this section we wish to develop a robust High Authority Controller (HAC) that is working for all payloads.

[2]

4.4.1 Using Jacobian evaluated at the center of stiffness

Decoupled Plant

SISO Controller Design As the diagonal elements of the plant are not equal, several SISO controllers are designed and then combined to form a diagonal controller. All the diagonal terms of the controller consists of:

- A double integrator to have high gain at low frequency
- A lead around the crossover frequency to increase stability margins
- Two second order low pass filters above the crossover frequency to increase the robustness to high frequency modes

Obtained Loop Gain

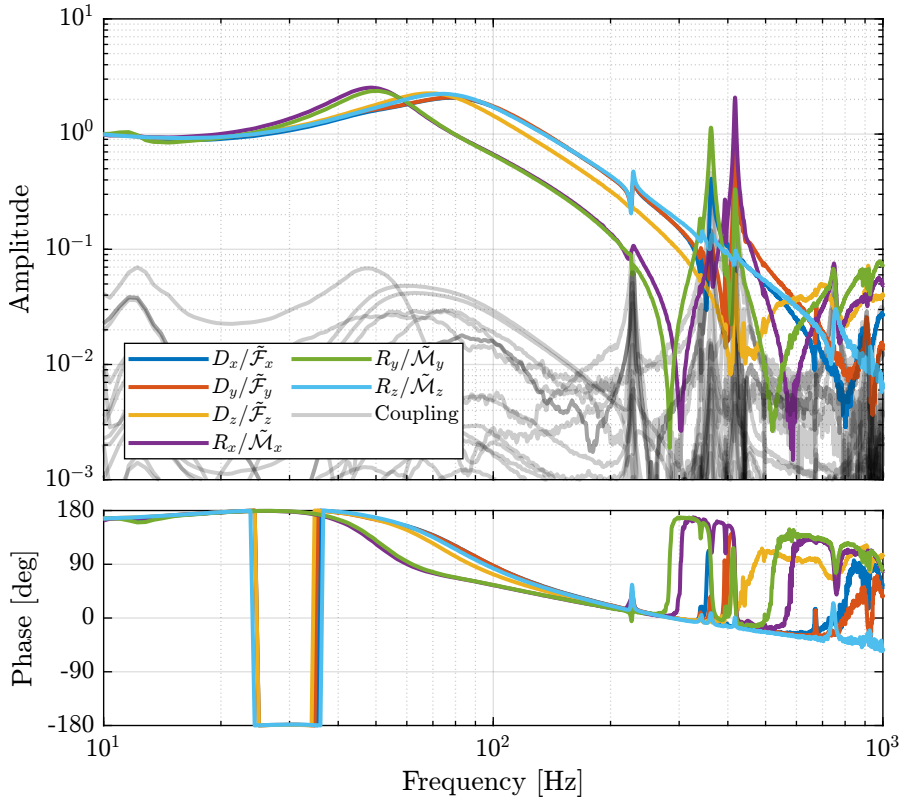

Figure 4.40: Bode plot of the decoupled plant using the Jacobian evaluated at the Center of Stiffness

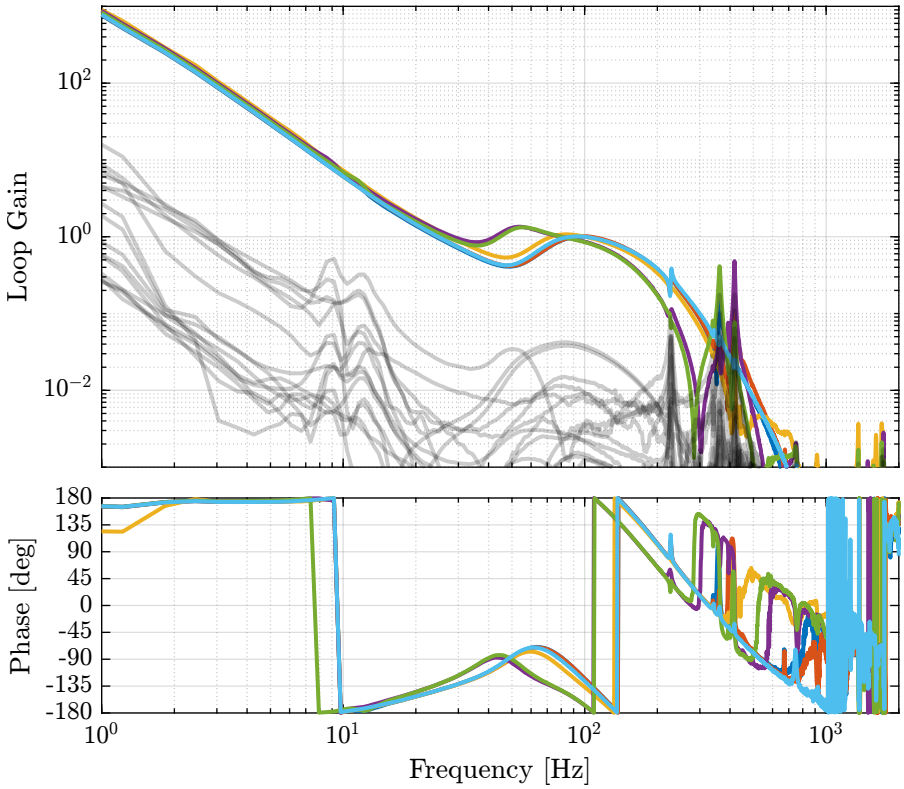

Figure 4.41: Bode plot of the Loop Gain when using the Jacobian evaluated at the Center of Stiffness to decouple the system

Verification of the Stability Now the stability of the feedback loop is verified using the generalized Nyquist criteria.

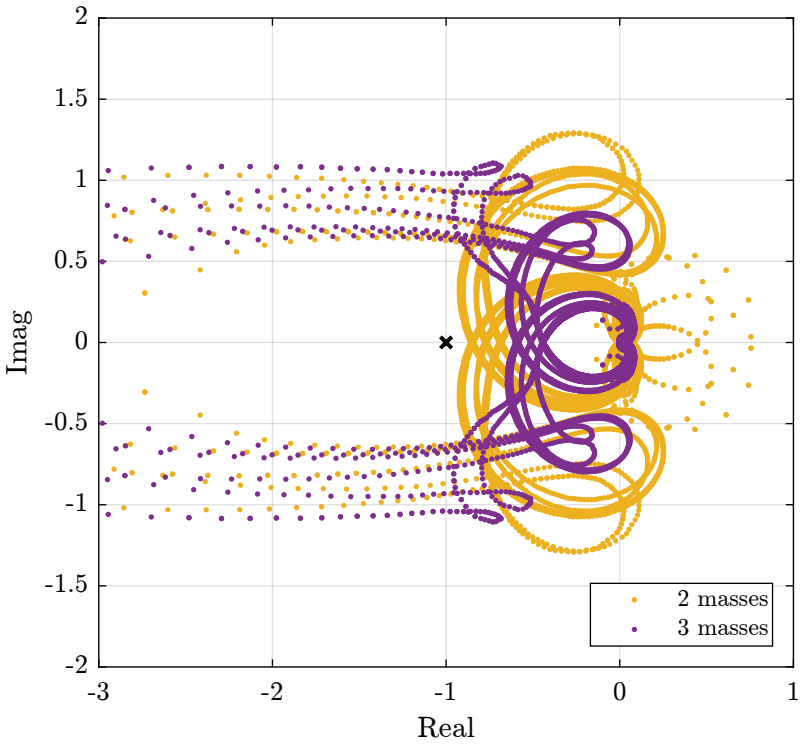

Figure 4.42: Loci of $L(j\omega)$ in the complex plane.

Save for further analysis

Sensitivity transfer function from the model The results are shown in Figure 4.43.

4.4.2 Using Singular Value Decomposition

Decoupled Plant

Controller Design

Loop Gain

Stability Verification

Save for further analysis

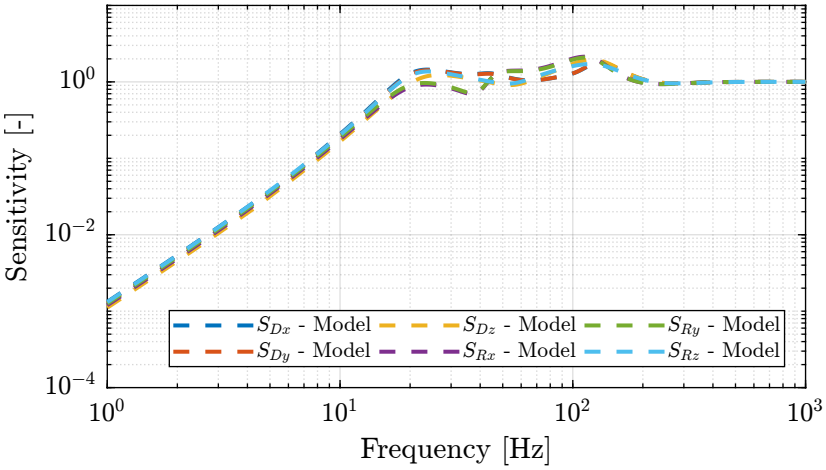

Figure 4.43: Estimated sensitivity transfer functions for the HAC controller using the Jacobian estimated at the Center of Stiffness

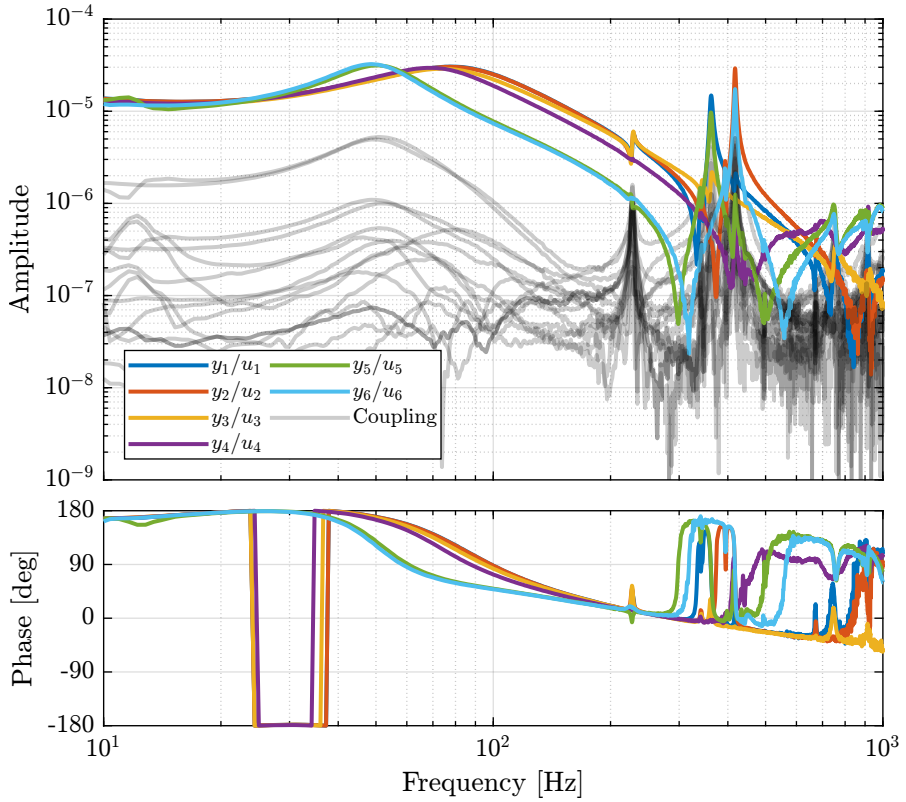

Figure 4.44: Bode plot of the decoupled plant using the SVD

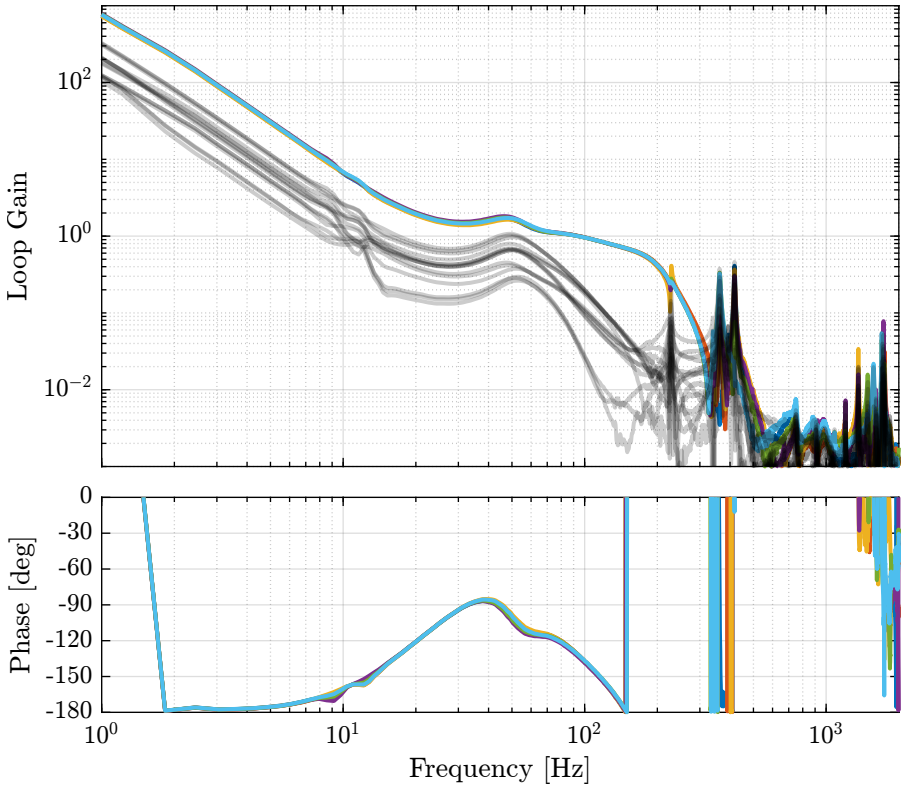

Figure 4.45: Bode plot of Loop Gain when using the SVD

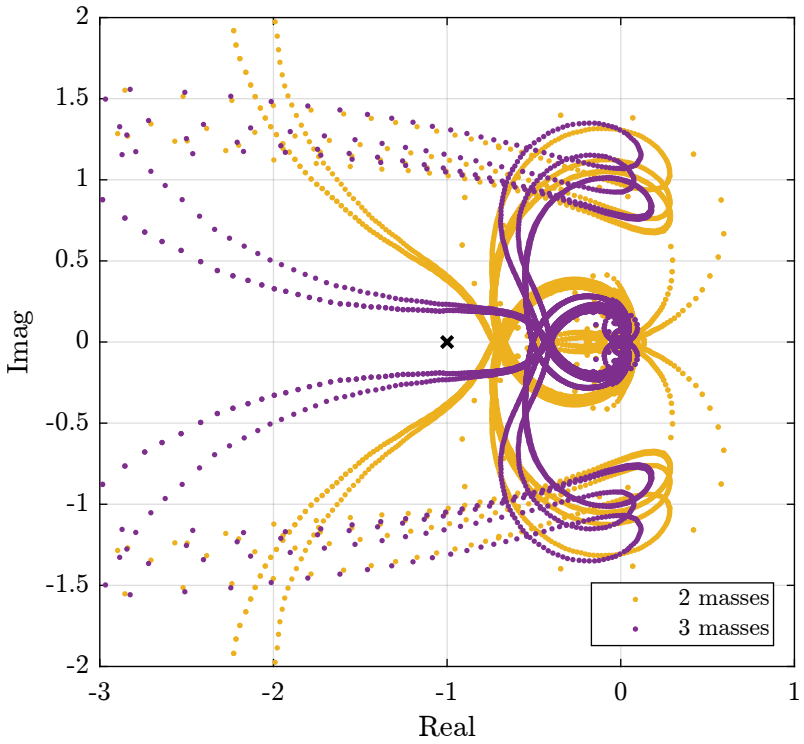

Figure 4.46: Locis of $L(j\omega)$ in the complex plane.

Measured Sensitivity Transfer Function The sensitivity transfer function is estimated by adding a reference signal R_x consisting of a low pass filtered white noise, and measuring the position error E_x at the same time.

The transfer function from R_x to E_x is the sensitivity transfer function.

In order to identify the sensitivity transfer function for all directions, six reference signals are used, one for each direction.

An example is shown in Figure 4.47 where both the reference signal and the measured position are shown for translations in the x direction.

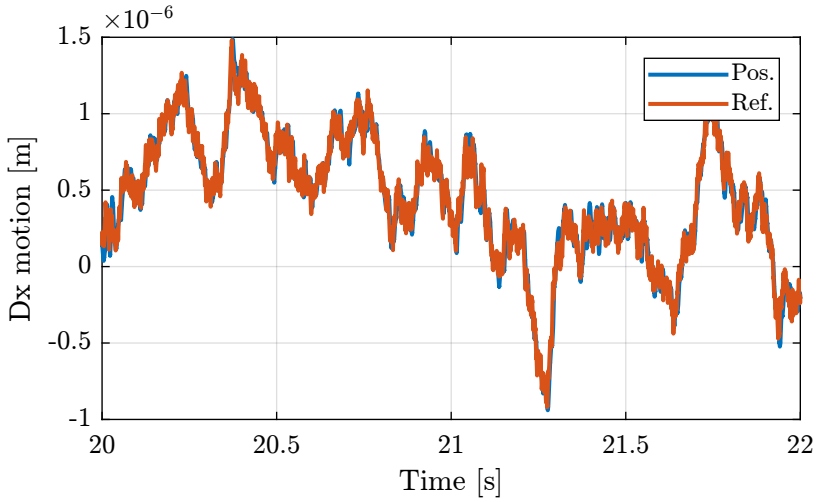

Figure 4.47: Reference position and measured position

The sensitivity transfer functions estimated for all directions are shown in Figure 4.48.

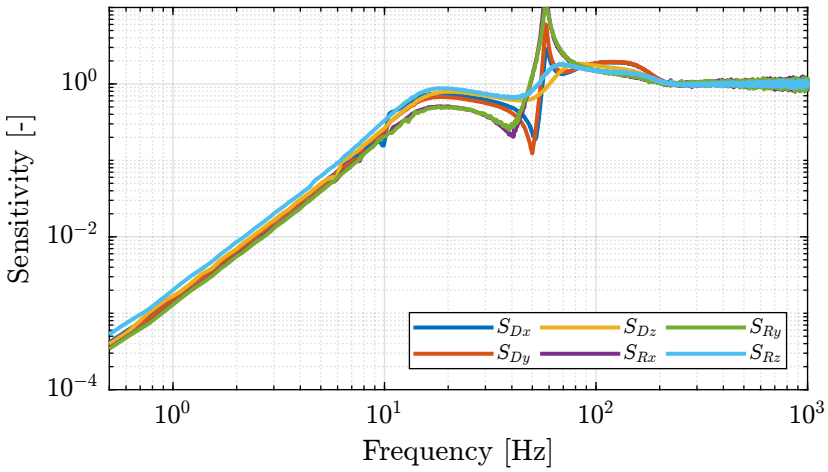

Figure 4.48: Measured diagonal elements of the sensitivity transfer function matrix.

Important

From Figure 4.48:

- The sensitivity transfer functions are similar for all directions
- The disturbance attenuation at 1Hz is almost a factor 1000 as wanted
- The sensitivity transfer functions for R_x and R_y have high peak values which indicate poor stability margins.

Sensitivity transfer function from the model The sensitivity transfer function is now estimated using the model and compared with the one measured.

The results are shown in Figure 4.49. The model is quite effective in estimating the sensitivity transfer functions except around 60Hz were there is a peak for the measurement.

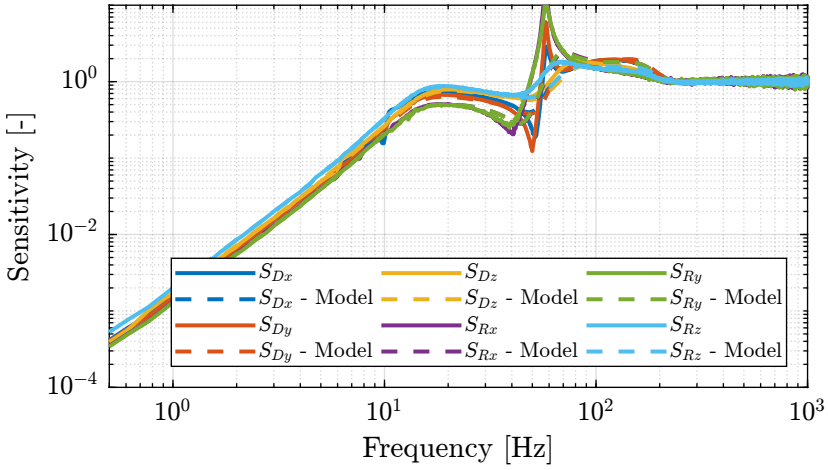

Figure 4.49: Comparison of the measured sensitivity transfer functions with the model

Bibliography

[1] S. Skogestad and I. Postlethwaite, *Multivariable Feedback Control: Analysis and Design - Second Edition*. John Wiley, 2007 (cit. on p. 83).

[2] M. Indri and R. Oboe, *Mechatronics and Robotics: New Trends and Challenges*. CRC Press, 2020 (cit. on p. 95).